ABSTRACT

Title of Dissertation: FABRICATION AND CHARACTERIZATION OF NANOSCALE SHAPE MEMORY ALLOY MEMS ACTUATORS

Cory Ray Knick, Doctor of Philosophy, 2020

Directed By: Professor Hugh A. Bruck,
Department of Mechanical Engineering

The miniaturization of engineering devices has created interest in new actuation methods capable of large displacements and high frequency responses. Shape memory alloy (SMA) thin films have exhibited one of the highest power densities of any material used in these actuation schemes with thermally recovery strains of up to 10%. With the use of a biasing force, such as from a passive layer in a “bimorph” structure, homogenous SMA films can experience reversible shape memory effect provided they are thick enough that the crystal structure is capable of transforming. However, thick films exhibit lower actuation displacements and speeds because of the larger inertial resistance. Therefore, there is a need to find a way to process thinner SMA films with grain structures that are capable of transformation in order to realize larger actuation displacements at higher speeds. In this work, a near-equiatomic NiTi magnetron co-sputtering

process was developed to create nanoscale thick SMA films as thin as 120 nm. By using a metallic seed layer, it was possible to induce the crystallization of epitaxial, columnar grains exhibiting the shape memory effects in nanoscale films ranging from 120 – 400 nm. It was also possible to crystalize these SMA films at lower processing temperatures (as low as 325 °C) compared to directly sputtering thicker films onto Si wafers. The transformation behavior associated with the SME in these films were characterized using x-ray diffraction (XRD), differential scanning calorimetry (DSC), and stress-temperature measurements at wafer level. After quantifying the shape memory effects at wafer-level, the SMA films were used to fabricate various microscale MEMS actuators. The SMA films were mated in several "bimorph" configurations to induce out of plane curvature in the low-temperature Martensite phase. The curvature radius vs. temperature was characterized on MEMS cantilever structures to elucidate a relationship between residual stress, recovery stress, radius of curvature, and degree of unfolding. SMA MEMS actuators were fabricated and tested using joule heating to demonstrate rapid electrical actuation of NiTi MEMS devices at some of the lowest powers (5-15 mW) and operating frequencies (1-3 kHz) ever reported for SMA or thermal actuators. By developing a process to create nanoscale thickness NiTi SMA film, we enabled the fabrication of MEMS devices with full, reversible, actuation as low as 0.5 V. This indicated the potential of these devices to be used for high frequency, low power, and large displacement applications in power constrained environments (i.e. on chip).

FABRICATION AND CHARACTERIZATION OF NANOSCALE SHAPE MEMORY ALLOY MEMS ACTUATORS

By

Cory Ray Knick

Dissertation submitted to the Faculty of the Graduate School of the

University of Maryland, College Park, in partial fulfillment

of the requirements for the degree of

Doctor of Philosophy

2020

Advisory Committee:

Dr. Hugh Bruck, Associate Dean for Faculty Affairs, Chair

Dr. Christopher Morris, Branch Chief, US Army Research Laboratory

Dr. Patrick McCluskey, Professor, Dept. of Mechanical Engineering

Dr. Don DeVoe, Professor and Associate Chair, Dept. of Mechanical Engineering

Dr. Miao Yu, Professor, Dept. of Mechanical Engineering

Dr. Ichiro Takeuchi, Deans Representative, Professor of Materials Science and Engineering

Acknowledgements

To Liz: for inspiring me to pursue my passions and for the many wonderful adventures and your companionship. For some of the most enjoyable and content moments in my life. You are my rock, my soulmate, and my forever, most trusted advisor. I dedicate this to you and our little one on the way. To Chris, Gabe, and Wayne: for helping me to develop personally and professionally. I am in large part where I am today, because of all you've done for me. Thank you for your invaluable mentorship and for the wonderful home away from home for several years. To Dr. Bruck: my advisor and academic role model. Thank you for your support in this PhD endeavor. Without your support and guidance, this body of work would not have been made possible. To my parents and grandparents who from day one have always inspired and encouraged me to pursue my dreams. Your love and support are immeasurable and so humbly and gratefully acknowledged. This project is dedicated to you all. To Zack: my brother and life's longest friend. To little Henry: for always reminding me that "outside" is the best place to be. I wish for you to grow up to engineer, create, tinker, build, and change the world for the better. To my friends: who have encouraged me to try rock-climbing, yoga, running, and helping me keep a healthy balance and perspective over the years. Cheers to many more enjoyable adventures. To my lab mates and colleagues: for the fruitful discussions. To Brendan: for your help with XRD. To Brian: for your tireless and dedicated support to bringing these devices to realization in the cleanroom. To Zeke: for your informal mentorship and relationship building. To Dan: I'm glad that SMASIS caused our paths to cross. I've greatly enjoyed my time in nature with you. Your assistance with the nanoindentation experiments is gratefully acknowledged, and I remain hopeful for continued collaborations together. To the CMU SHRIMP Team (including Sarah and Camilo): Thank you for your fantastic efforts in continuing the legacy of this work. For giving NiTi a chance to blossom

into awesome micro-bots. I am continuously inspired by your team. To all who helped me to invent and maybe one day transition technology to our warfighter. To Andrew: for your longtime friendship, and now dedicated and tireless service to our nation, and to all your fellow soldiers who defend our freedoms and help maintain our global dominance. It is the greatest honor to work and create for you. To Darin and Adam: you are exemplars of smarts, innovation, and dedication, and it has been my great pleasure to work alongside you. To Asher: for your help with TEM and insightful discussions about metallurgy, and phase diagrams. To Ron: for setting the gold standard and showing us how it's done. May we all continue to emulate you. To Whitney: for believing in us and giving us the freedom and confidence to get it done. To George: I'm tickled that our paths crossed at such a fortuitous time. Thank you for showing me how to truly push the limits. To Miguel and Jason: for taking a chance on me, and giving me the avenues to push the maturity and application of this technology even more. To the youth of this world (our future): a career in science, technology, engineering, and math (STEM) is most rewarding and impactful. Stay curious. Keep asking questions.

Table of Contents

List of Figures

List of Tables

Chapter 1: Introduction and Literature Review

"There's plenty of room at the bottom: An Invitation to Enter a New Field of Physics," the famous lecture by physicist Richard Feynman in 1959 at the American Physical Society meeting at Caltech, inspired researchers to explore the nanoscale. He opened up the possibility of direct manipulation of individual atoms as a more powerful form of synthetic chemistry than those used at the time. Since then, there has been a rapid explosion of research into micro and nanotechnology. This work seeks to miniaturize a fascinating, multi-functional class of materials known as shape memory alloys (SMAs) based on the physical control of atomistic and crystal structures at the micro and nano scales.

1.1. Shape Memory Alloy Thin Films

SMAs are a class of functional smart materials. They have the ability to remember their original form after thermal-mechanical deformation at a high stress level (over 500 MPa) and large recoverable strains (up to 10%). Additionally, the work output (per unit volume) for SMAs is highest among all smart material actuators, making them competitive in both high force and high displacement applications. SMA applications are found in aerospace, automobiles, robotics, micro-electromechanical systems (MEMS), and biomedical tools. MEMS/Nano-electromechanical systems (NEMS) is a multi-billion dollar, worldwide market that can benefit from technological development of miniaturized functional or smart materials like SMAs. Due to their high work output (~10^7 J/m^3), Nickel-Titanium (NiTi) alloy is one of the most well researched and most promising alloy classes. With miniaturization comes the promise of overcoming

inherently slow thermal response times due to small thermal mass and a large surface area to volume ratio (SVR). The aim of this work is to show that in combining some of the thinnest NiTi actuators with MEMS/NEMS scale actuators (such as small volume joule heaters), the device can be cycled faster, and through greater ranges of motion than any SMA-based devices to date.

Of the many SMAs available, NiTi has become one of the most widely used due to its exceptional physical and mechanical properties including shape memory effect (SME) and super/pseudo-elasticity (SE), including large recoverable strains [1]. To understand the reason behind the SME/SE in NiTi, it is necessary to first understand the crystallography. The basis for SME/SE is the switching between two different crystallographic phases, namely the high temperature phase known as austenite (or) the parent phase, and the low temperature phase known as martensite. The crystal structure of the austenite phase is a CsCl type B2 cubic structure and the low temperature martensite phase is a complex monoclinic crystal structure (B19'). The martensitic transformation is a diffusionless solid-state phase transformation. During the martensitic transformation, the metal atoms move cooperatively in the matrix under shear stresses. As a result a new phase is formed from the parent phase. To accommodate the internal stresses caused by the transformation to the B19' phase, the formation of a combination of up to 24 multiple martensitic variants is possible, resulting in a twinned martensite crystal form, also known as self-accommodated martensite.

The first ever reported thin film version of sputtered shape memory alloy was done by Walker (of Bell Laboratories) in 1990 [2]. The first several accounts of SMA film characterization on Si wafers showed measureable shape memory effects, but all phase-transformations happened below ambient conditions, which is of no utility for thermal actuators operating at ambient conditions. This was in part due to the fact that the films tended to be Ni-rich in composition if

starting from equiatomic NiTi sputter target, due to the different sputter yields of Ni and Ti. Ni has a higher sputter rate than Ti, and Ti has a tendency to react with any residual oxygen in the deposition chamber. In order to make high performance thermal actuators, it is necessary to undergo the specific processing to ensure transformations are measured above ambient conditions. This is no easy task, but can be done by carefully controlling Ni/Ti ratio and thermal processing (i.e. annealing). Krulevitch presented one of the earlier accounts of thin film NiTi as SMA for micro actuation [3]. One of the first SMA-based MEMS actuators was reported out of Case Western University in 2001, based on a sputtered NiTi film capable of recovering about 250 MPa according to their stress-temperature loop on a 4 inch Si wafer [4].

Regarding the in-situ crystallization of NiTi, Gisser also observed that the films deposited on (100) silicon (Si) substrates at 733K (equivalent to 500 °C) showed a (110)-oriented crystalline structure [5] of the austenite phase. Hou also observed that the films deposited onto quartz and polyimide substrates above 623K (equivalent to 350 °C) showed a strong (110)-oriented crystalline structure [6]. There is significant room for improvement of shape memory effects concerning texture, as it has been reported that the (111) orientation of austenite would exhibit even greater shape memory effects due to larger recoverable strain [7], but this orientation has been hard to realize. Dominant martensite peaks at room temperature tend to be (200) and (022). This range of crystallization temperatures of the NiTi films suggests that the crystallization process is affected by the surface condition of the substrates. However, it is not clear why the heated substrates lowers the crystallization temperature and enhances a particular orientation for the NiTi thin films. This is due to lack of understanding the process of film growth during deposition. The composition and structure of sputtered NiTi SMA films are significantly affected by the sputtering conditions: target

power, gas pressure, target to substrate distance, deposition temperature, substrate bias voltage, etc. [5, 8-16].

NiTi films with transformation temperatures above room temperature are difficult to manufacture due to compositional shifts in the film deposited onto substrates like glass or Si wafers. Sputtering processes typically produce films with reduced transformation temperatures (i.e. below room temperature), prohibiting their use as practical actuator material. The reason for this is that a shift of as little as 1 atomic % can reduce transformation temperatures by 100 °C. Ho and Carman showed that NiTi films deposited deviate by up to 2 atomic % in lower Ti composition when compared to target compositions [9, 17, 18]. Thus, certain methods must be employed to ensure that the film composition is near equiatomic or Ti rich, in order to help ensure reliable shape memory properties above room temperature. Additionally, important issues like formation of film texture and its control are not yet understood, but it is important to identify and control their preferential orientation, as it is a crucial factor in determining the extent of the strain recovery [7].

Barber [19, 20] looked into sputter deposited NiTi onto Si from separate Ni and Ti targets using a 1 μm per hour deposition process, and 2 μm thick films. It was shown that phase transformation from martensite to austenite happens above room temperature for equiatomic and Ti-rich films, and below room temperature for Ni-rich films. Through a nanoindentation technique, it was determined that Ni-rich films exhibit SE effect, and Ti-rich samples exhibit SME. The mechanism for deformation is different in SE and SMA NiTi films. For austenite films, deformation can cause transformation into martensite and detwinning; while in martensite phase, only detwinning takes place. De-twinning is metastable in the austenite phase and thus reverses upon unloading, where as it is permanent in martensite phase until a temperature is applied to convert the sample into austenite.

In 2017, Reddy (of the Indian National Institute of Technology) looked at the influence of annealing temperature on structural, morphological, mechanical, and surface properties of NiTi thin films [21]. They sputtered NiTi (unheated) onto Si (100) substrates using DC magnetron sputtering with separate Ni and Ti targets and performed post-deposition crystallization annealing study. Crystallinity increases up to 550 °C, but decreases at 650 °C due to recrystallization.

For MEMS integration, there is a need for an electrically and thermally insulating or sacrificial layer. Therefore, the study of NiTi film deposition on different types of substrates is an important topic of research [14]. In MEMS, mechanical property of materials has an important role on the performance of devices. Characterization of the mechanical properties of MEMS materials has been an active research area during the recent years. Ishida et al. first evaluated the mechanical properties, including yield stress, elongation, and ductility of sputter-deposited NiTi thin films [22-24]. Besides Fu et al. presented their researches on residual stress of sputter-deposited NiTi thin films [10, 12, 14, 15, 25-27]. SMA films have been deposited by sputtering and evaporation. SMA films with high performance have been realized for MEMS such as 600 MPa recovery forces and recovery strains of 6%, which are sufficiently useful properties for MEMS actuation [27]. A few researchers have reported on micro hardness and Young's modulus of sputter-deposited NiTi thin films [28]. Young's modulus is phase dependent, and for austenite is around 80 MPa, and for martensite 20 - 40 MPa. Clearly, the lower temperature martensite phase is more compliant than the high temperature austenite phase.

The preferential orientation of NiTi thin films is a crucial factor in determining the shape memory behavior. The texture has a strong influence on the extent of the strain recovery. Shu et al., using "recoverable strain" as a measure of SME, have shown that texture is a crucial factor in determining the SME in polycrystals and strong textures may lead to anisotropic shape memory

behavior [7, 29]. Concerning the texture of NiTi thin films deposited on Si (100) substrates, different behavior has been observed between amorphous films post-sputtering annealed and those sputtered at elevated temperatures (> 400° C) where the films are crystalline as deposited in the latter case with substrate heating. A post-deposition annealing of amorphous NiTi films leads in many cases to a weak texture or almost none [30], probably due to a homogeneous nucleation mechanism by which the crystalline phase forms [31]. For films crystallized during deposition, a strong (110) fiber texture is commonly observed for the B2 BCC cubic structure [5] suggesting that the crystalline phase nucleates on the surface of the heated substrate assuming an orientation that minimizes surface energies [32, 33]. The effect of annealing temperature on amorphous sputtered NiTi was investigated in these works [23, 28, 34, 35].

In the case of films deposited on thermally Si oxidized substrates, Su et al. observed a strongly (110)-textured B2 on films presenting a good adhesion to the SiO_2/Si substrate (200 nm SiO2 layer) [36]. These films were deposited at room temperature and subject to an annealing at 560 °C. Wuttig showed that there exists an interface that is able to crystallize into the austenite (B2) phase on the order of 50 - 100 nm thick that is not able to thermally transform between martensite (B19) and austenite phase [37], as shown in Figure 1. To overcome this problem in SMA films, it is very common to ensure a NiTi thickness of 1 - 2 μm or greater in order to ensure measureable, reversible SMA properties. In other words, there exists a thin layer of NiTi at the interface of substrate that does not contribute the shape memory effect. This is a key reason why generating reliable, and reversible phase change above room temperature in sub-micron thickness films is often very challenging.

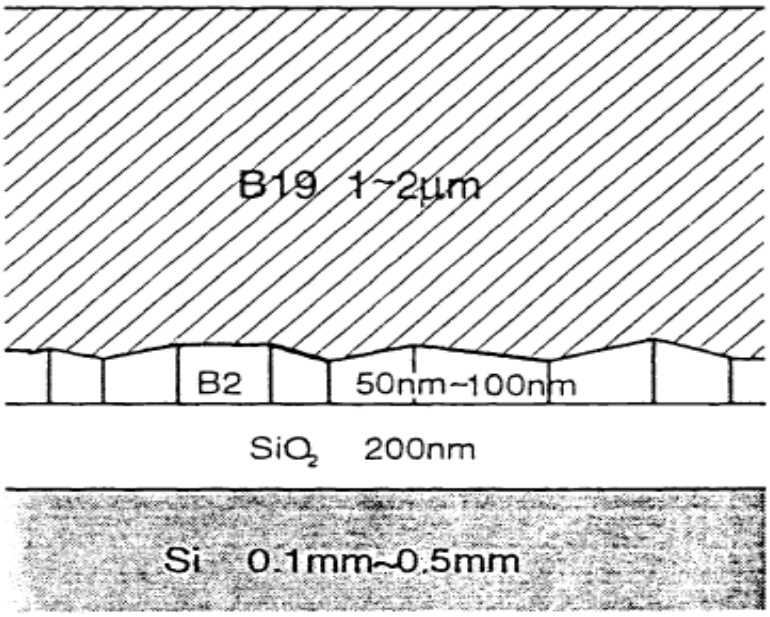

Figure 1. NiTi SMA Film on typical MEMS substrate (200 nm SiO_2 on Si wafer) from [38].

On the other hand, Kim et al. have mentioned the formation of an (200)-oriented NiTi film (100 nm thick) deposited at 550 °C on a Si oxide/Si substrate (300 nm Si oxide layer) [39]. This work also has shown that (110)-oriented NiTi films (also 100 nm thick) are obtained when a Pt random-oriented layer is deposited on top of the Si oxide substrate (at room temperature) before the deposition of the NiTi film at high temperature.

For relatively simple and straight forward characterization of shape memory effect in sputtered films of NiTi (especially those onto Si wafer), there exists the wafer bow versus temperature measurement. This experiment uses Stoney's equation, and measures the Si wafer curvature over a temperature range (e.g. room temperature – 100 °C), and can routinely be used to determine the Nitinol residual stress, recovery stress, and phase transformation temperatures as shown in Figure 2. The assumption under this method is that the film is much less thick than the substrate, so therefore ~1 μm thick NiTi on ~525 μm thick Si certainly meets this criteria.

Secondly, it is assumed that the compositional uniformity across the wafer is highly uniform, and there exists no compositional gradient in the radial direction that would lead to changes in phase transformation temperature. This second assumption is generally less valid, since composition gradients can naturally exist, but we cut back on these effects as much as possible by rotating substrate during deposition to maintain highest possible levels of uniformity.

The Case Western Group, led by Materials Science Prof. A. Heuer showed some of the first comprehensive quantitative phase transformation behavior in NiTi SMA thin films on 4" Si wafer [40]. Combining XRD and stress versus temperature measurements (i.e. wafer bow), they demonstrated that NiTi films are suitable for microactuator application due to low residual stress and relatively large amounts of recovery stress, at least for NiTi films between 1 - 2 μm in thickness.

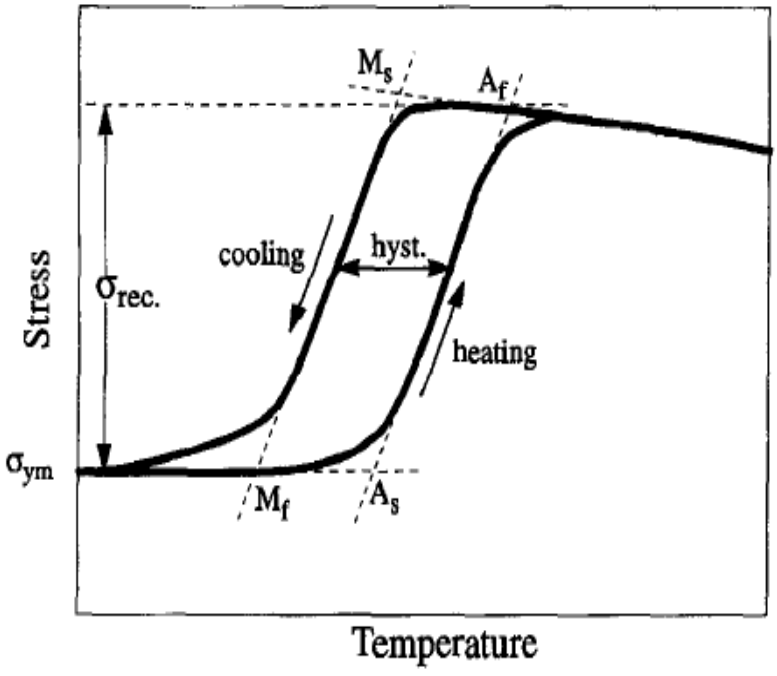

Figure 2. Schematic wafer stress vs. temperature hysteresis loop and definitions of phase change temperatures and thermal hysteresis. From [41].

Stoney's equation (shown below) can be used to measure and track the residual stress in Nitinol film on Si wafer substrate. E is the Si wafer young's modulus. V is Poisson ratio of Si wafer. Hs denotes thickness of substrate (which is much larger than that of film), h denotes the Nitinol film thickness, R_o is the initial radius of Si wafer, and R is the radius after deposition of Nitinol. The higher nonlinear stress versus temperature loop show in Figure 2 is typical of the Nitinol phase being thermally transformed between martensite (at lower temperatures) and austenite (at higher temperatures). Recovery stress is a good indicator of the amount of stress than can be harnessed to actuate a MEMS cantilever actuator based on Nitinol. The residual stress is a good indicator as to how much residual stress deformation would be expected in a released MEMS structure.

$$\sigma = \frac{E}{6(1-\nu)} \frac{{h_s}^2}{h} \left(\frac{1}{R} - \frac{1}{R_o} \right)$$

Ishida looked into the thickness effect on shape memory behavior of TiNi thin films and found that there are two kinds of constraints due to surrounding grains and surface oxides, where surface oxide constraints are especially important in submicron films [24]. Hou and Hamilton have done some very nice work on submicron SMA films [42] using the biased target ion beam sputter deposition of Nitinol. NiTi thin films showed a uniform crystallite orientation distribution or a typical [110] fiber texture depending on sputtering condition, and the transformation strain was almost the same, irrespective of direction in the sputtered films. In keeping with the theme of thickness effects, Fu showed a lower limit of SMA transformation (for film confined to substrate) of 105 nm, using the well-known wafer curvature approach [11]. Figure 3 shows the SMA stress-temperature loops for films of decreasing thickness. The 48 nm thick film did not exhibit any

measureable SME, for reasons indicated above. Namely, there exists an interfacial region between NiTi film and substrate it is deposited onto that does not undergo reversible transformations. This interfacial layer has been shown in some instances to be 50 - 100 nm in thickness. Therefore, when coupled with the oxide surface layer that also imposes restraints on transformation, there exists a critical thickness for which a film must be in order to exhibit any reversible phase change to drive a microactuator.

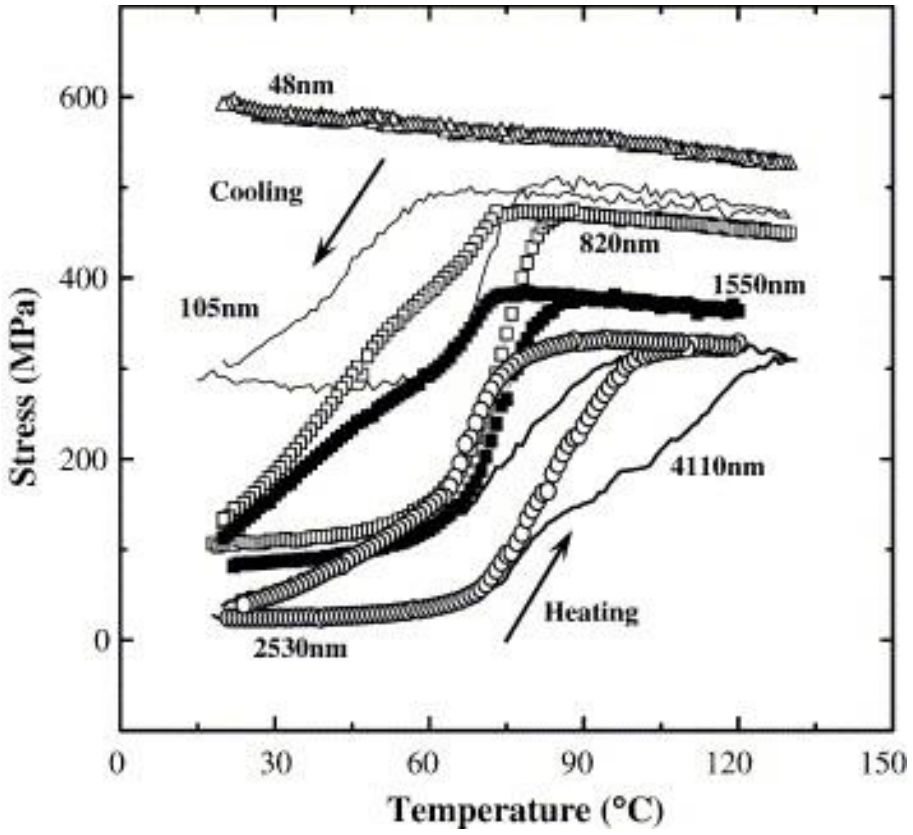

Figure 3. NiTi stress-temperature loops for various thickness NiTi films on Si, showing diminishing SMA properties below 100 nm from [11], "On the lower thickness boundary of sputtered TiNi films for shape memory application".

Gisser et. al. [5] have shown a preferential development of <110> oriented grains of the B2 phase since the beginning of the deposition has been observed (without and with the application of a substrate bias voltage of −45 and −90 V). The *in-situ* study of the structural evolution of the

growing Ni–Ti film as a consequence of changing the Ti: Ni ratio during deposition (on a TiN <111> layer) has also been performed. The preferential growth of <110> oriented grains of the NiTi B2 phase has been as well observed despite the precipitation of Ti_2Ni during the deposition of a Ti-rich NiTi film fraction. Functionally graded NiTi films should lead to an intrinsic "two-way" shape memory effect which is a plus for the miniaturization of NiTi films based devices in the field of micro-electro-mechanical systems [43]. Special thermo-mechanical treatments can generate precipitates with preferred orientations that promote the growth of specific martensite variants on cooling.

Ternary films of NiTiCu have also been investigated, and can generally lead to above ambient transformation properties coupled with narrow-thermal hysteresis [15, 26, 27, 44-47]. Interfacial microstructures of TiNi thin films RF sputtered on to Si (100) and post-annealed at 400 – 700 °C for 30 minutes have been investigated using analytical and high-resolution transmission electron microscopy. For annealing temperatures below 600 °C, a very thin amorphous (Si, O)-rich layer is observed at the interface. Ni atoms are the primary diffusing species and $NiSi_2$ forms triangularly and epitaxially towards the Si substrate. TiNi films initially crystallize after 30 minutes at 500 °C. Si and Ti atoms begin to migrate in specimens annealed at 600 °C for 30 minutes. At this temperature, a near-$Ti_4Ni_4Si_7$ phase in triangular $NiSi_2$ and a near-TiNiSi phase in the TiNi film are simultaneously nucleated and grown at the interface. For the specimens annealed at 700 °C for 30 minutes, two layers of $Ti_4Ni_4Si_7$ and TiNiSi form at the interface with the sequence TiNi/TiNiSi/$Ti_4Ni_4Si_7$/Si. Triangular $NiSi_2$ islands are now embedded in the $Ti_4Ni_4Si_7$ layer. A mechanism of interfacial microstructure evolution is proposed to explain the temperature effect on the interfacial reaction layers between the TiNi film and the Si (100). Lower processing temperatures or metallic seed layers should be expected to minimize some of these effects.

Islague [48] found that NiTi films containing an excess of Ti (52 at %) were crystallized when deposited on Si (100) substrates heated up to only 473 K (equivalent to 200 °C). NiTi/Si(n) Schottky diodes I–V characteristics showed a temperature dependence indicating structural transition in the NiTi electrode.

Kotnur completed a PhD dissertation on SMA films on flexible substrates leading to crystallized films on polyimide (PI) [13, 49]. These results helped lay the groundwork for extending NiTi sputter deposition towards monolithic integration with flexible substrates, such as those required for soft bodied micro robotics.

1.2. Shape Memory Thin Films in MEMS Applications

NiTi thin films are in demand for applications in actuators for MEMS because these films exhibit large displacement, accompanied by the shape memory effect (SME) through the B2 austenite to B19' monoclinic martensite transformation. Take for example a 10 μm thick NiTi film, 2 mm wide, that could easily generate over 500 MPa of recovery stress. Such an element, resistively warmed, or thermally actuated to modest temperatures, could exert over 10 N of force or lift a 1 kg mass. Highly optimized NiTi films have potential to double this capacity [16]. The majority of NiTi films are fabricated by RF or DC magnetron sputtering methods, and these films are amorphous, unless the substrates are heated during deposition [10, 12, 14, 15, 50]. Post deposition annealing at a temperature above 700K (equivalent to 427 °C) for crystallization is necessary for the films initially deposited in amorphous condition to show the shape memory effect [8]. In fact, one specific study [51] showed that NiTi films (with Ti-rich compositions) sputtered onto Si (100) at 300 °C and 400 °C were amorphous, by XRD. Even additional four hour anneals at 300 °C and 400°C was not sufficient to induce crystallization. Only by annealing at 500 °C and 600 °C for four hours, was crystallization of the NiTi confirmed. It is noted that NiTi thin films

sputter-deposited at ambient temperature are amorphous, thus require post-sputtering crystallizing at elevated temperature to obtain the desired shape memory property [30, 52]. It is also possible to crystallize NiTi films during deposition by utilizing a heated substrate above an ambient temperature. The NiTi films deposited in this manner exhibit interesting behaviors such as lowered crystallization temperature and oriented crystallographic structure [5]. For example, Ikuda observed that the NiTi film deposited onto a glass substrate at 673 K (or 400 °C) produced crystallinity in the NiTi film. Other, more recent studies also looked into the SMA properties of in-situ annealed NiTi films [53, 54].

Figure 4 highlights that SMAs have the highest actuation stress (MPa) compared against piezo ceramics, magnetostrictive ceramics, shape memory polymers (SMPs), and electrostrictive ceramics. Figure 4 also highlights that metallic SMAs like NiTi also can undergo large amounts of actuation strain, between 2-8 % reversibly for many cycles. Only SMPs can undergo higher strains owing to their extreme flexibility (low Young's modulus), but this happens at very low speeds, often requiring many seconds to fully unravel or actuate, in part due to the poor thermal conductivity and slow heat transfer of polymers. Most recently, Sharar et. al showed that bulk NiTi shape memory alloys are highly promising candidates for solid-state thermal energy storage, based on the high latent heat of transformations associated with the reversible martensitic transformations [55]. The high thermal conductivities of the NiTi alloy (15-28 W/mK) are suitable for transporting heat. These authors expanded upon this work to show that physical properties of the NiTi could be tailored through manipulation of grain size (~40 nm to ~60 μm) through different solution annealing procedures [56].

Figure 5 also highlights the impressive actuation energy density of SMAs (>10^3 J/kg). From this figure, we see that SMAs simply cannot actuate as fast as MSMAs, electrostrictive and

magnetostrictive ceramics, and especially piezo ceramics like lead zirconate titanate (PZT). Therefore, one of the most obvious rooms for improving SMA would be to increase the actuation bandwidth, or rate that SMA can be actuated. By shrinking the SMA volume (ultra-thin NiTi films) we can therefore enable improved surface to volume ratios (S/V) which would improve the rate of heat transfer. The main focus of this PhD therefore is on the miniaturization of NiTi SMA MEMS devices, to enable rapid heat transfer and rapid, reversible actuation, and move the actuation frequency (Hz) to the right for SMA, making in more appealing for higher frequency actuation applications.

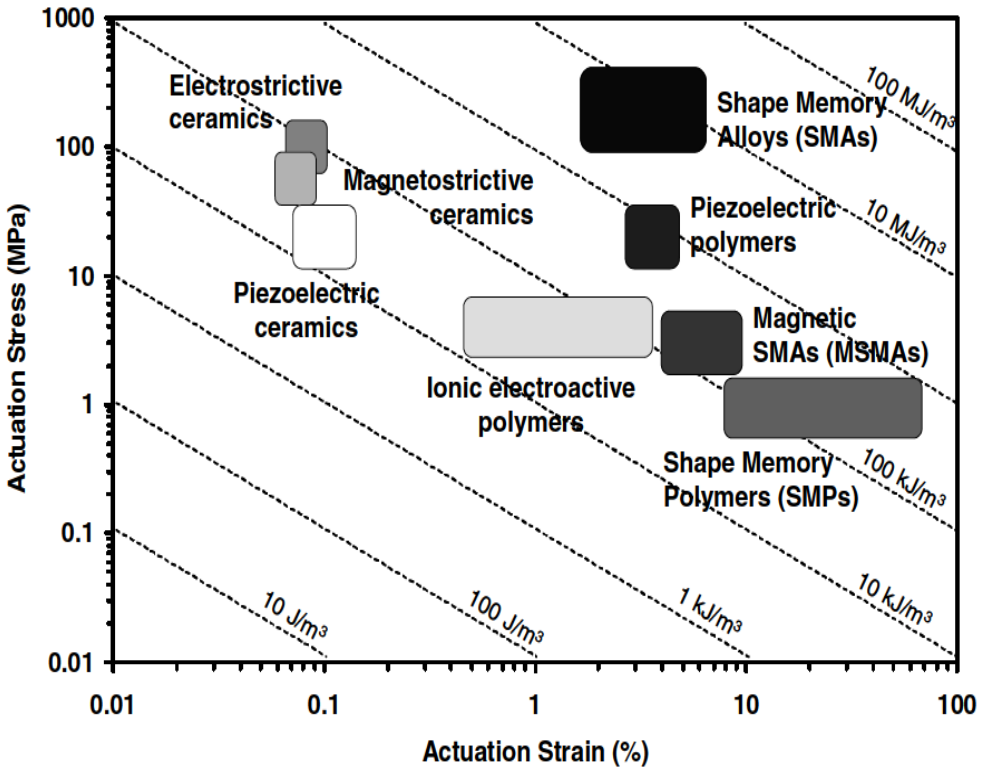

Figure 4. Actuation stress (MPa) vs. actuation strain (%) for common smart material actuators, highlighting that NiTi SMA can achieve simultaneous high stress and high strain, leading to the highest actuation energy density. Adapted from Lagudas textbook.

One major smart-material actuator in addition to SMAs is the piezoelectric ceramic actuators, one common example being lead-zirconate-titanate (PZT). As you can see, PZT can only undergo reversible strains up to 0.1%. This makes sense intuitively because PZT is a brittle ceramic, a class of materials with strong atomic bonding, characterized by brittle stress-strain response. By comparison, the NiTi SMAs, being from the metallic class of alloys can undergo reversible strains up to 8-10%, making it much more desirable than PZT or other ceramics for large displacement actuations. PZT is of course much more competitive for lower forces, but rapid cycling (into the MHz) such as would be required for RF MEMS components like variable-capacitors (varactors), MEMS RF contact switches, oscillators, and resonators for applications such as filtering and tuning in RF communications front ends [57, 58]. NiTi could certainly be made more attractive in high-bandwidth applications if its bandwidth could be improved upon. One natural room for improvement is in device down-scaling both in terms of device size and film thickness. If one can achieve an overall significant reduction in volume of SMA actuator needing to be heated, then the thermal cycling problem can be significantly improved upon and NiTi could compete in this space.

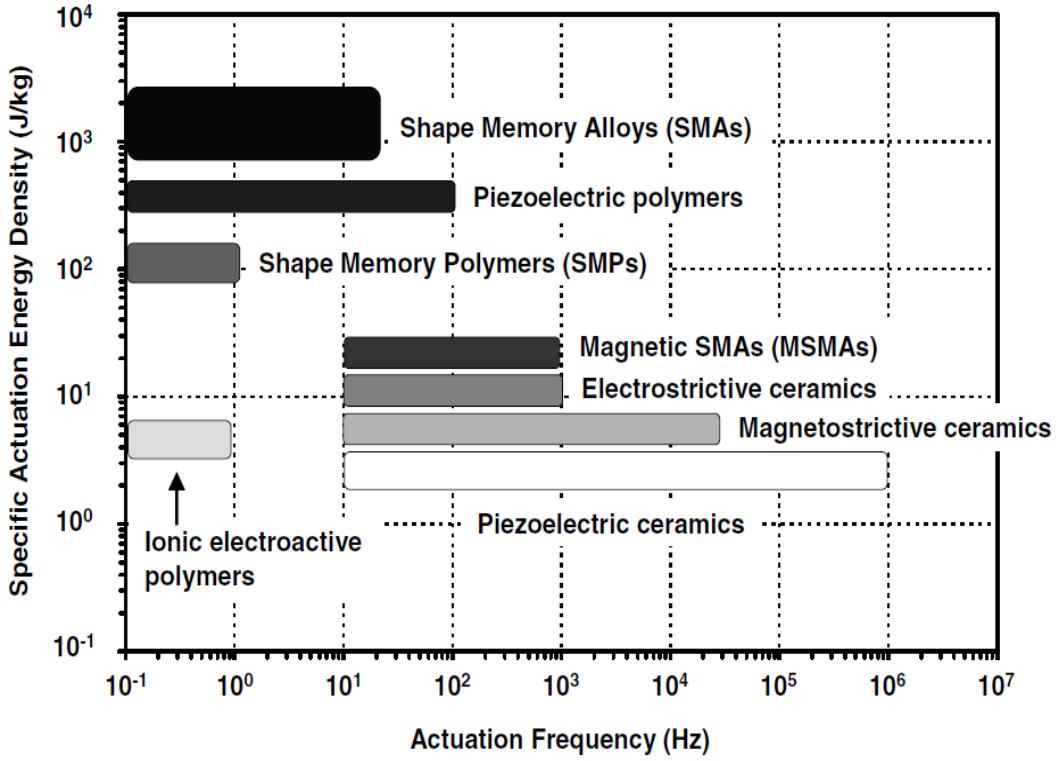

Figure 5. Specific actuation energy Density (J/kg) vs. actuation frequency (Hz), highlighting SMA as the highest energy density, but overall slow in frequency response (<100 Hz)

NiTi (Nickel Titanium) is a shape memory alloy (SMA) known for shape memory effect and superelasticity. The shape memory effect and superelasticity allows NiTi to be strained reversibly unto 6-8%. NiTi thin films are of technological interest as actuator materials in MEMS because they possess a large deformation and recovery force compared to other performance materials proposed for fabricating microactuators . Several early attempts were made to fabricate NiTi thin films and build NiTi thin film based microactuator prototypes, such as micropumps and microvalves, microgrippers and microsensors.

Functionally graded shape memory alloys (FGSMAs) have also been of great interest [59]. One obvious advantage of functionally graded shape memory alloys is their widened

transformation stress and temperature windows that provide improved controllability in actuating applications. AbuZaiter, et al. [60]. Lambrecht has a few very recent studies on martensitic transformation and nanoscale actuation in nanoscale thickness SMA bimorphs of NiMnGa on Si [61]. In 200 nm thick NiMnGa films, they show a 3% change in maximum beam deflection per beam length in agreement with finite element simulations. The thermal bimorph effect competed with the SMA phase change cause deflection to go in opposite directions. Observance of shape memory effect strongly depends on SMA/Si thickness ratio. For nanoactuators there exists a large temperature gradient along the beam length. Optimal SME were exhibited for SMA / Si ratio of 90 / 250.

Although there have been numerous studies of SMA film properties in the early years, a very recent paper added to this comprehensive understanding. Reddy [21] looked at NiTi on Si (100) deposited by DC magnetron sputtering (without intentional substrate heating), and from separate targets of Ni and Ti. Films were annealed post-deposition for 60 minutes at 350 °C, 450 °C, 550 °C, 650 °C. XRD revealed that crystallinity increased up to 550 °C, but decreased at 650 °C. They showed NiTi films have a strong tendency to show TiO_2 on the surface. The hardness and Young's modulus increased up to 550 °C but decreased at 650 °C. Their films were ~300 nm thick.

Phase transformation behaviors of shape memory alloys (SMAs) are strongly affected by size reduction [62] as shown in shape memory alloy wires. In 2003, Carmen demonstrated a miniature shape memory alloy actuator capable of cycling at 100 Hz due to an active cooling design [17]. Lehnert studied the influence of annealing parameters on the martensitic phase transformation in sputter-deposited Ti rich NiTi films is systematically studied by differential scanning calorimetry and by transmission electron microscopy [63]. He found that NiTi sputtered

at 500 °C has fine grain size and is homogeneous. Transformation properties could be significantly altered by changing film composition or annealing procedure.

Liu [32] studied the effect of crystallizing procedure on microstructure and characteristics of sputter-deposited TiNi shape memory thin films [32]. Ti-rich TiNi shape memory thin films, sputter deposited by different crystallizing procedures, may display quite different microstructures. For the room temperature films deposited on Si substrate at room temperature and post crystallized at 600 °C, the structure at room temperature is martensite. When martensite is present at room temperature in the NiTi film, then physical actuation resulting from significant changes in film stress lead to actuation above room temperature in the MEMS device. The grain size is a few μm and almost no texture exists. For the high temperature films deposited at ~500 °C and crystallized *in-situ*, the structure at room temperature is austenite. The grain size is only several tenths of a μm and a strong texture is able to develop. Thus, with small grains, and no martensite phase present at room temperature, this shows that 500 °C, in-situ annealed NiTi would not exhibit actuation due to M <> A-phase change above RT in MEMS applications.

In an impressive paper titled “Shape Memory Alloy (SMA)-Based Microscale Actuators with 60% Deformation Rate and 1.6 kHz Actuation Speed [64]” these researchers showed pulsed laser actuation of a FIB milled SMA wire. They integrated a force sensor that was capable of monitoring force as a function of time for pulsed laser optical-induced heating actuation of an in-place stretching SMA actuator. As the laser irradiation power increased from 5 to 50 mW, the reaction force increased and the force saturation time, which is the time required when the average force measured during 10 ms reaches first to the maximum force, decreased. The rates and forces of the reactions did not increase linearly and eventually became saturated as the laser power

increased. The optimum laser conditions for actuation are those that induce the maximum force and highest speed

They selected a 355 nm UV laser source due to its high absorption coefficient when applied to metals. As with all metals, NiTi absorbs more light in the UV region than in the visible or infrared region. In addition, lasers with wavelengths of 355 nm have small spot sizes and high peak powers, meaning they can be used as alternative heating sources for microscale SMA actuation. The actuation speed of their device was slower than piezoelectrically driven actuators (less than tens of kHz), but almost 30 times faster than the highest previously reported SMA actuation speed (50 Hz).

Kwok looked into Fabrication and characterization of sputtered NiTi shape memory thin films using in-situ crystallization in some samples, and solution treatment of 700 °C and aging treatment of 400 °C on amorphous samples [65]. He looking into RF and DC sputtering. The substrate heated sample showed only B2 phase at room temperature in the XRD scans (i.e. only austenite, no martensite), so the film would not actuate above room temperature. The 1 hour – 700 °C sample + 1 hour at 400 °C also only showed B2 phase at room temperature, so would not make a thermal actuator. Only the 6 hour aged film (400 °C) showed appreciable amounts of B19' phase at room temperature, which would make for a thermal actuator. The nucleation and growth of NiTi thin films has been systematically studied using TEM [52].

Actuation based on shape memory films has been shown in bimorph and trimorph configurations [66, 67]. The bimorph configuration is desirable in nanoscale thickness SMA films because other implementations could prove challenging with such small amounts of SMA to work it. Other methods known to create two-way shape memory effect (TWSME) or reversible shape change are localize annealing, functionalized gradients (composition gradient), and dead weight

bias. Dead weight bias could be tricky in MEMS because structures are so small, that "weight" of additional elements would be negligible to cause any significant biasing mechanism. Oriented defects or oriented precipitates are alternative methods, but there is no well-known way to control or predict this effect, making an actuator like this would only come from luck rather than "engineered actuation". Figure 6 shows the methods to engineer reversible shape change using extrinsic and intrinsic biasing mechanisms.

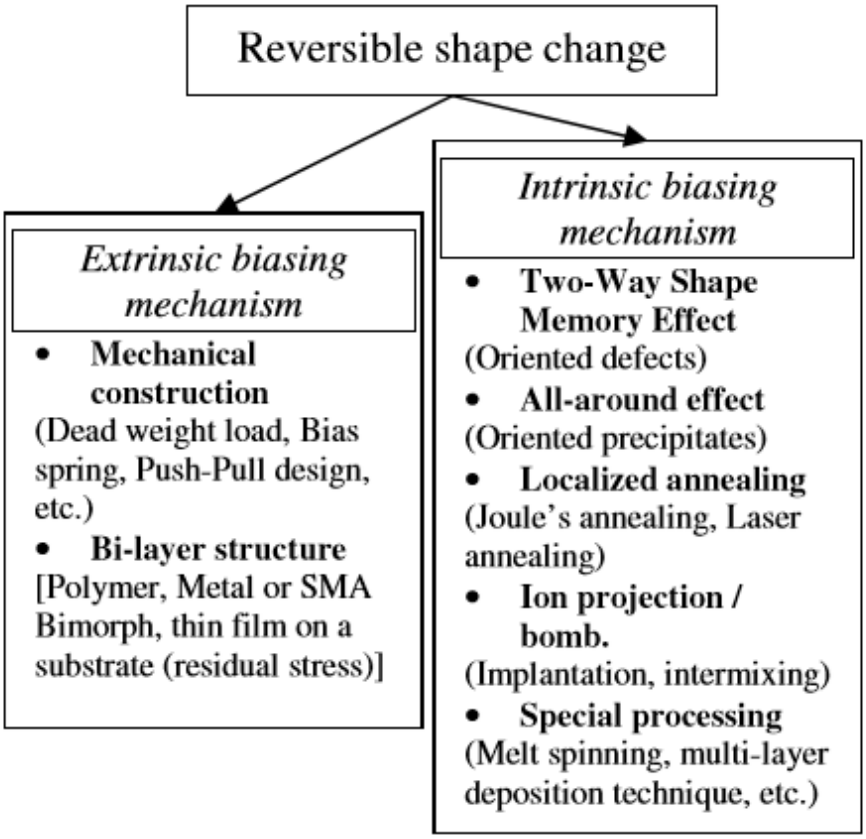

Figure 6. Methods (extrinsic and intrinsic) for inducing reversible shape change in SMA materials.

NiTi films of 100 μm thickness were used in conjunction with stress layers to fabricate SMA-bimorphs, albeit a bit larger than true MEMS scale [60]. Stress layer thickness were on the order or 2 - 6 μm and structures sizes were 10 mm in length. Nonetheless, this was a very nice

study of SMA Bimorph actuation and it would be interesting to the MEMS community to see if similar actuation applies at much smaller scales. That is in part, the pursuit of this PhD thesis: measure shape memory MEMS-scale actuation in sub-micron thick NiTi films.

A MEMS device based on NiTi on SiN was fabricated and tested. The MEMS SMA-bimorph actuator was caused to curl upward due to the residual stresses that develop in NiTi, and the SMA beam uncurled when heated do to shape memory effects. The uncurling was only partial and this group did not quantity the radius of curvature or uncurling, rather they presented microscope pictures on hotplate. Various MEMS bimorph actuators based on shape memory alloy have been demonstrated already [60, 68-71]. MEMS thermal bimorph actuators have also been demonstrated [72]. In plane buckle-beam actuator design is well-known [73]. NiTi SMA has even recently been integrated with Si photonics to form a physically actuated optical coupler/de-coupler type device with excellent nano-positioning accuracy to within 4 nm and on/off ratio of 9 dB [74, 75].

Residual stress in MEMS thin films has caused curling of microstructures in many documented cases. Of course, thinner cantilevers have potential for tighter curling radius because stiffness scales with the cube of thickness. Dr. Chris Morris used highly tensile stressed Cr on relatively neutral stress Au to create tightly folding microgrippers [76], that were limited to single use scenarios. A similar approach was demonstrated for single cell gripping, with much smaller curling radius by mating residual stress bilayers with tensile and compressive layers [77]. Nickel-Vanadium (NiV) alloy is also well known to be a highly tensile stressed metal as reported in [78], at 1.8 GPa tensile stress. Mismatch in stress across a common boundary leads to folding of released structures as reported in several other cases [79, 80]. As another example, 50 - 100 nm of

evaporated Cr on Si, generally has a residual tensile stress of around 1 GPa, which could alternatively be used to bend released NiTi bilayers to impart a TWSME.

It was suggested that SMA materials and effects could also be used for Nano actuation [81], which would enable new applications. However, in order to achieve such further miniaturization, the actuator thin films need to become thinner, and particularly, the lateral-structure sizes need to become smaller, from millimeters, over micrometers, to nanometers. Therefore, it is necessary to investigate if there is a limit concerning the functionality of SMA materials with decreasing size and if the shrinking of lateral device dimensions is accompanied with scaling effects. For the characterization of micro- to nanoscale SMA materials and devices, the following parameters and their scaling dependence on lateral structuring need to be monitored: 1) occurrence and reversibility of the phase transition; 2) phase transition temperatures; and 3) width and shape of the thermal hysteresis. It can be expected that these effects will be strongly dependent on the materials used and the way they are processed. In the literature, scaling effects in nanostructured SMA materials were identified with the general tendency that the shape-memory effects are shifted to lower temperatures or are even suppressed for the smallest structures. For different material systems, it was found that a decreasing grain size leads to decreasing transformation temperatures [82, 83]. Fu et al. attributed the change in the transformation characteristics to the influences of the top TiO_2 layer and the interfacial layer between substrate and thin film [8]. Recently, *in situ* transmission electron microscope (TEM) nanocompression tests on NiTi nanopillars have been performed, showing that a stress induced transformation from the austenite (B2) to the monoclinic martensite (B19') occurs even for nanoscale volumes with a sample size below 200 nm [9].

The role of film geometry on the phase-transformation properties of 1.1 μm $Ni_{48}Ti_{52}$ (Ti-rich) thin films was compared for continuous films with 5-μm-wide stripes in [84]: An increase of the transformation interval was found and implications are that MEMS devices (such as simple cantilever actuators) may not necessarily behave as continuous films (i.e. NiTi on Si wafer bow measurements).

A study of 1 micron thick amorphous NiTi films was performed [34]. The conclusion was that if you anneal too hot, or too long, you lose a significant amount of martensite-phase detected with XRD at room temperature. In fact, the paper seems to show that more ideal shape memory effects could be achieved for a 460 °C anneal for 5 or 10 minutes, compared to 660 °C anneal for 1 hour. Another study looked at incomplete martensitic transformations in NiTi thin film by running wafer bow thermal stress scans, but interrupting them (i.e. cooling the sample) before complete transformation from M-phase to austenite. [85]

Ishida [24] studied the thickness effects on shape memory behavior of Ti-50.0at.%Ni thin films. They did TEM and XRD on NiTi films of 0.5, 1, 2, 5, and 7 μm. All films were annealed for 300 seconds (equivalent to 5 minutes in vacuum at 500 °C). They draw the following conclusions: The films show an equiaxed structure with an average grain size of about 5 μm. Thickness effect on the shape memory behavior becomes prominent below 5 μm, whereas it is negligible above 5 μm thickness. As the thickness decreases from 5 μm, the transformation strain and residual strain increase gradually and then decrease rapidly after showing a maximum around 1 – 2 μm NiTi film thickness. The variation of the transformation and plastic strains with thickness can be explained in terms of two kinds of constraints from surface oxide layers and neighboring grains. Surface oxidation affects also the transformation temperature when the thickness is less than 1 μm. In this PhD dissertation, some of these claims are verified to be true; namely that 600

°C anneal for 1 hour after a room temperature NiT sputter in the 0.5 - 1.5 μm film thickness range leads to very small amounts of recovery stress. Alternatively for 0.5 - 1.5 μm thick NiTi films sputtered in unheated condition and annealed for 5 - 10 minutes at 460 °C, exhibit exceptional amounts of recovery stress (via wafer bow), and significant amounts of reversible deformation in MEMS-scale bimorph actuators.

Another relevant study looked into the relationships between sputter deposition conditions, grain size, and phase transformation temperatures in NiTi thin films [82]. An *in-situ* NiTi annealing study on 3 μm thick NiTi films showed that crystallization and SMA properties can be controlled by substrate deposition temperatures [54]. Another study summarized some recent developments in shape memory thin film technology [86].

Thickness and films stress effects on martensitic transformation in equiatomic NiTi thin films has been investigated [87]. It was shown here that if thermal stress in austenite exceeds ~300 MPa, the martensitic transformation occurs in a one step process between B2 <> B19'. Films with lower residual stress follow a two-step transformation of B2 <> R-phase <> B19'. For films less than 400 nm thickness, the transformation temperature decreases rapidly with diminishing film thickness, thus making it incredibly difficult to obtain shape memory actuators based on films 400 nm or thinner. Models for phase transformation behavior of an SMA film constrained to substrate have been discussed in the literature [37].

The crystallization process is a direct consequence of the grain nucleation and growth at elevated temperatures. As a result, the annealing temperature and time will influence the structure as well as property of NiTi thin films and their shape memory behavior. A connection between the annealing temperature and phase transformation temperatures of NiTi thin films has previously been reported by Surbled et al [35].

Photo lithographically defined NiTi actuators exist [88] and can generally do before med using chemical wet etch, ion mill, or Reactive ion etching (RIE). The isotropic nature of the wet-etch prevents small MEMS features (below a few microns) to be reliably patterned, and anisotropic methods like ion mill or RIE should be used instead. Another novel aspect of this PhD is the development of low-power ion mill etch recipes that are compatible with typical MEMS photolithography and allow us to pattern small (2-3 μm) wide NiTi actuator beams, useful in the scale down of SMA MEMS actuator devices, such as joule heater actuator, MEMS switch, and MEMS optical mirror arrays (OMAs).

In order to obtain useful force-displacement product from NiTi SMA film, it is necessary to plastically deform the martensite through a biasing mechanism such as elastic bias spring. Such a "bias" can be obtained due to differential thermal expansion of NiTi on Si [89-91]. Local images taken from NiTi samples showed that grains larger than 150 nm undergo a martensitic phase transformation at a temperature of approximately 50 °C, while neighboring grains smaller than 50 nm do not transform into martensite, even in a liquid nitrogen environment [92], providing further evidence for a minimum grain size in order for shape memory effects to be observed. The effects of substrate conditions on Nanocrystalline NiTi films fabricated by magnetron co-sputtering [93] was studied, where they found that phase transformations are impeded in small grains.

Waitz showed using TEM measurements, that with decreasing grain size, the Martensite transformation is completely suppressed below GS = 60 nm due to increasing energy barrier for the transformation [94]. The R-phase transformation, which is only responsible for relatively small amounts of transformation strains is observed for GS between 15 and 60 nm. In grains below 15 nm, only B2 austenite phase is present, indicating no phase transformation happens for GS below 15 nm. This is a really nice paper on thickness and grain size dependence of B2 <> R martensitic

transformation behaviors in nanoscale TiNi films [95]. Size effects relating to the SMA or SE properties of NiTi have been investigated in nanoscale dimensions [62, 96-99]. Several PhD dissertations have looked into NiTi SMA films, characterizing nanoscale thickness SMA or MEMS devices based on SMA films in nanoscale thickness range. Huilong Hou from PSU developed biased-target ion beam deposition (BTIBD) of NiTi [42]. Konig looked at nanoscale objects based on SMA [100].

Although not the topic of this dissertation, a class of high temperature shape memory alloys exist to enable shape memory or superelastic properties in more extreme environments. In fact, it may be relevant for MILSPEC, due to the fact that NiTi generally transforms somewhere between well-below ambient and up to about 70-80 °C max, which does not meet the MILSPEC requirement to operate in environments up to 70 or 80 °C. To prevent, unintended actuation, the military design engineer may be well-suited to choose one of these other NiTiX alloys for higher temperature "actuation" designs. High temperature SMAs (HT-SMAs) are generally defined to have operating temperature above 100 °C. More well know classes of alloy consist of NiTiPt, and NiTiPd. A model was developed to predict the crystallization of laser annealed amorphous NiTi [101].

Shape memory alloys (SMAs) have early on been considered as a potential solution for efficient microactuators as these materials offer attractive properties like a high-power to weight ratio, large deformation and the capability to be processed at the micro-scale [102].

Figure 7 shows the extrinsic two-way shape memory effect (TWSME). One way to achieve the two-way shape memory effect in MEMS-scale actuator is through the "bimorph" effect [60, 68-71]. Residual stresses, formed in part due to CTE mismatch and elevated temperature depositions or crystallizations will cause the NiTi film to bend once released from substrate. The

bulk, macro scale analogy is that of the mass hanging from SMA spring. The SMA is shape-set into its tightly coiled configuration, the hanging mass causes the NiTi to go from twinned martensite (in unstressed configuration) to detwinned martensite (stressed configuration). Once heated, the NiTi will phase transform into austenite and rapidly morph into its shape-set position. The hanging mass makes this a reversible process. There is also a documented tendency for these transformation temperature to shift towards higher temperatures under high stresses. So in the case of NiTi bimorph actuators, the large degree of bending could actually prove desirable for ensuring that the phase-change happens above room temperature.

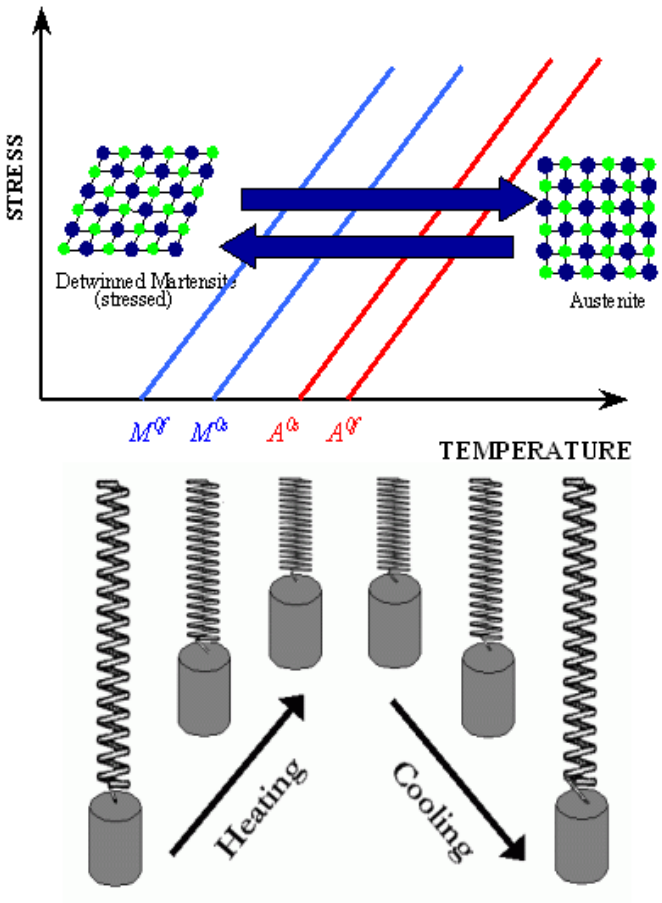

Figure 7. Constant stress SMA actuator exhibiting the two-way shape memory effect (TWSME) [Lagudas book on SMA].

Low temperature processing of NiTi is also of interest to enable integration with CMOS and soft materials (polymers, polyimide, SU-8, etc.). Islague showed the NiTi could at least be partially crystallized when deposited as low as 200 °C onto Polyimide films [48] by using a Ti-rich composition (~52 at%). Whether or not these films would exhibit any appreciable shape memory effects is unclear as they were not investigated in this work. A recent paper reviewed NiTi SMA thin films for MEMS applications [103]. In this paper they compared NiTi SMA vs. other actuator technologies. They quoted SMA actuation time as 30 milliseconds. Using miniaturized joule heaters, this dissertation showed drastic reductions in response time of SMA actuators down to 400 µsec.

Even by using the narrow thermal hysteresis R-phase transformation, researchers could only achieve a maximum of 125 Hz actuation frequencies in NiTi SMA diaphragm actuator [104]. In fact, it was predicted that maximum frequency for SMA actuators would plateau around a few hundred Hz. One particularly novel aspect of this PhD dissertation was miniaturization of NiTi MEMS device, to enable electrically actuated SMA up to 3 kHz, pushing the state of the art in actuation frequency up from hundreds of Hz to several kHz.

Kohl presented an SMA microgripper with integrated antagonism with the following specs: max displacement of 180 µm, max gripping force of 17 mN, electrical power of 22 mW, and response time of 32 milliseconds [105]. This device was made from 100 µm thick NiTi which was laser cut to size. A comprehensive review of SMA MEMS applications is presented in [106] and [103]. MEMS switches made from thin film SMA and carbon nanotube (CNT) is demonstrated in [107]. Radio controlled SMA coil inductor for "wireless" actuation was shown in [108]. Additional review papers on SMA MEMS are given in [25, 109]. Planar extrinsic biasing of SMA MEMS actuators is documented in [89]. Micromachining processes for NiTi SMA are described in [110].

Intrinsic Two-way SME (TWSME) in SMA actuators was achieved in [111]. Mechanical Properties of SMA films were characterized in [112]. Characterization of low-temperature deposited NiTi on "soft" substrates like polymers [113]. Heterogeneous structures combining NiTi and PZT cantilevers were described in [58]. Development of NiTi-polyimide actuator [114]. Bi-stable, laser actuated NiTi device [115]. SMA pump for microfluidic transport [116]. Control of internal stress in SMA bimorph actuators [70]. Mechanical properties and optimal design of SMA actuators [112].

High temperature SMA actuators for applications where operation temperature is >100 °C [117]. Micro thermostat array of NiTi devices [118] has been demonstrated. Tailoring microstructure in SMA films [53] is an important area of study, as crystal orientation is known to influence shape memory effects, recovery stress, and recovery strain. The influence of processing and texture in SMA transformation properties is discussed in [21]. Nitinol can be laser cut with CW and femtosecond laser [119]. In additional to sputtered thin films SMA, there also exists additive manufacturing approaches to fabricate SE and SME structures based specifically on NiTi-based alloys. SLM additive manufacturing of NiTi SMA [120] is discussed. SLM and DEM (directed energy melting) of NiTi heterostructures [121] is also an area of study. A review of additive NiTi is presented here [122]. Additional additive NiTi references include [120-124].

NiTi SMA micropumps papers (fab and device characterization) including W. Benard's work. [47, 116, 125, 126]. Review of additively manufactured NiTi [122]. Nanocrystalline NiTi SMA fabricated from co-sputtering technique [93]. Grain size effects on shape memory properties in nanocrystalline NiTi SMA has been reported [98]. Thickness and film stress effects on NiTi phase transformation is discussed in [87]. NiTi thin films micro cantilevers array have been fabricated in [127]. Grain size effects in sputtered NiTi [83]. Effects of film dimension on

transformation properties [84]. A NiTi SMA-based microgripper was fabricated and characterized [128]. Characterization of NiTi SMA using temperature controlled AFM [129] has been demonstrated. Effects of film composition on NiTi properties [20] is known to play a crucial role. Fabrication of NiTi/Cu SMA bimorphs was shown in [71]. Texture and anisotropy play a critical role in shape memory and superelastic properties in additive manufactured NiTi [130]. Double layer SMA bimorphs [131] have been shown to have interesting properties. Effects of annealing can influence on SMA properties [34].

Prediction of thermally-controlled actuation for shape memory alloy film-based bimorph cantilevers was modeled and experimentally verified in [68]. Their model takes into account temperature dependent changes in material property of NiTi as it is driven through its phase transformation from martensite to austenite. Deflection is calculated based on Timoshenko's formula for bimetallic strip [132]. These authors developed a useful model to predict the actuation (i.e. temperature induced deflection) of NiTi SMA bimorph cantilevers (shown in Figure 8) which is extensible to other substrates. Clearly the influence of substrate (i.e. cantilever in which NiTi is deposited) rigidity or Young's modulus is apparent. More compliant, ductile, (i.e. bendable) materials like Quartz and Brass with lower modulus (72, and 100 GPa), should exhibit more significant actuation changes in deflection during the SMA phase change as compared to cantilever substrates that are more rigid like Mo and Mica (329, and 172 GPa) as shown in Figure 9. Si for reference is 130 GPa, which is in the middle of these extremes considered.

The deposition temperature also plays a critical role in the amount of deflection incurred. The caveat, is the system of consideration here is NiTi sputter coated at high temperature onto a free standing Si beam. As is the case for more realistic NiTi MEMS actuator fabrications, NiTi gets deposited onto Si wafer and then patterned, prior to device release. The NiTi sputtered directly

onto Si is allowed to bend after deposition completes during the entire cool down period. These two cases are expected to be considerably different in terms of stress generation and relaxation. Typical depositions are done at 500 °C to 600 °C to ensure good crystallization of the NiTi film. The increase in bending likely comes from the additional curvature imparted into the bimorph at higher deposition temperature (i.e. driven by the larger changes in temperature for fixed CTE mismatch, as in the case of NiTi on Si beam). In these scenarios, their NiTi film is 2 μm thick, and the free standing Si cantilever is 100 μm thick, therefore active NiTi to Si cantilever ratio is 2%.

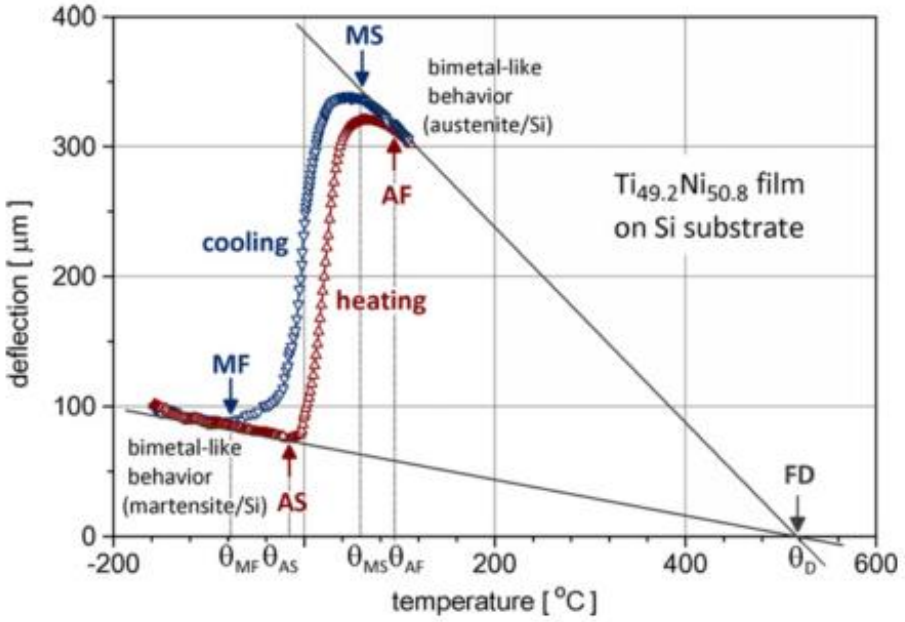

Figure 8. Typical actuation of a bimorph $Ti_{49.2}Ni_{50.8}$ / Si cantilever; the tangents (solid lines) to the single phase segments of the plot converge to deposition point FD (zero deflection point) [133].

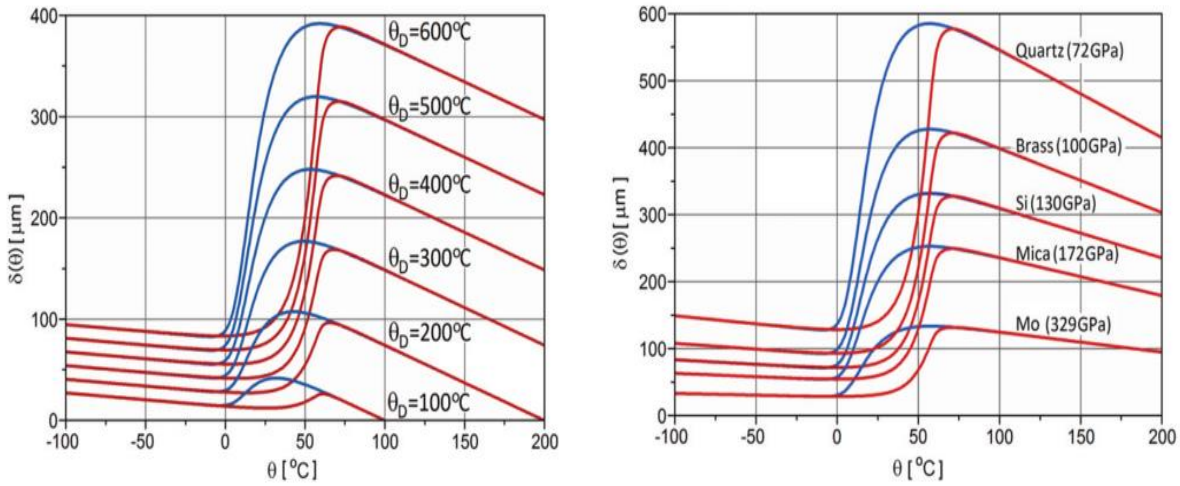

Figure 9. Predicted influence of reference temperature on the deflection of the Si-substrate cantilever (d_f = μm, d_s = 100 μm, L = 20 mm) during the martensitic transformation cycle in the TiNi. (left). Predicted influence of substrate Young's modulus on deflection of $Ti_{50.1}Ni_{49.9}$ SMA film-based cantilever (d_f = μm, d_s = 100 μm, L = 20 mm) during the martensitic transformation cycle. (right). From[133].

R-phase formation:

There is currently no effective approach to control the R-phase transformation [134]. It is not easy to largely separate the temperature domain of R-phase and B19' martensite phase transformation, especially in the presence of an external force. Grain size and aging microstructures each have an influence on the transformation behavior. After full solution annealing, near-equiatomic NiTi alloys show (upon cooling) a one-stage themo elastic martensitic transformation between B2 austenite (A) and B19' martensite (M). The presense of crystallographic defects (e.g. dislocations, coherent Ni_4Ti_3 precipitates), a thermoelastic transformation between austenite and rhombohedral (R-phase) has frequently been observed as an intermediate step between austenite and martesnite [12, 104, 134, 135]. Microactuators have been built and thermally actuated utilizing the R-phase <> austenite phase transformation [104, 134]. In general, this transformation results in much lower recovery strains (0.2 - 1.0 %), but has the

advantage of narrow thermal hystersis (0-5 °C) to allow for faster thermal cycling or thermal actuation [42]. It is will established that grain size of NiTi can be grown using for e.g. a 700 °C anneal for prolonged amount of time ranging between just several minutes to 1,000+ minutes (15+ hours) [136] as shown in Figure 10.

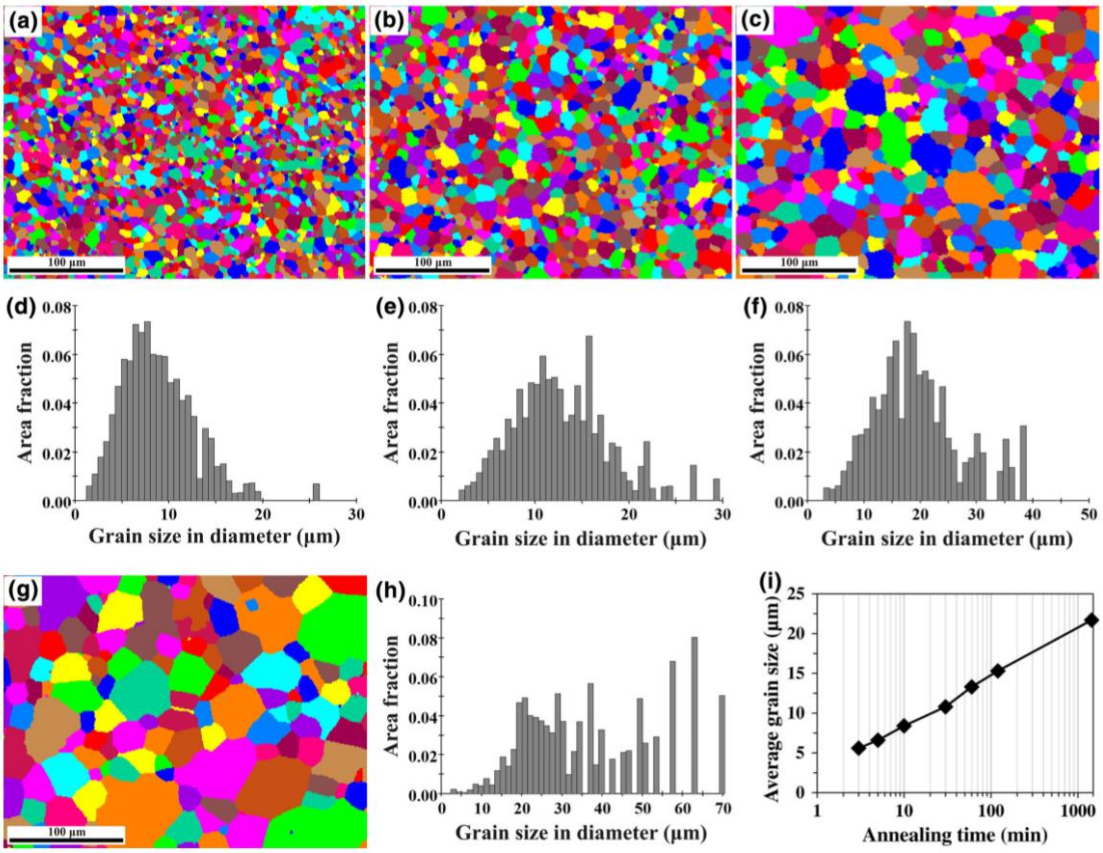

Figure 10. Effect of grain size on aging microstructure as reflected in the transformation behavior of a low-temperature aged Ti–50.8 at.% Ni alloy. Adapted from [136].

Certain papers deal with looking at influence of substrate conditions on nanocrystalline NiTi sputtered from elemental Ni and Ti targets. Substrate conditions can include temperature setpoint, “seed layer”, or RF bias for example. In one study, they bombarded with Ar ions using a -100 V substrate bias during NiTi film growth, and 300 °C substrate setpoint. They used XRD to measure crystallization. They reported martensite peaks at room temperature, indicating the

potential for phase transformaiton upon heating. Average grain saize of ther nanocrystalline samples, as the name suggests was quite small at just 30 - 50 nm. Generally speaking, ion bombardment during film growth leads to measurably larger grain sizes [93].

Effects of film dimension have also been studies and show some interesting behaviors [84], i.e. lithographically patterned lines posses a strain profile that significantly alters the phase transformation behavior. Amorphous NiTi 1.1 μm thick, and Ti rich (52 at% Ti) was sputter coated onto 200 nm SiNx coated Si wafer. Using photolithography and wet etch, 5 μm lines x 10 mm, and 13 μm spacing were patterned on the wafer. Vacuum crystallization was used (440 °C for 20 minutes). AFM and SEM were used as characterization, along with standard XRD. Wafer curvature was used to monitor stress on a full wafer between 25 – 100 °C. TEM revealed Grain size (GS) on the order of 2.5 +/- 0.5 μm for the films, and 1.7 +/- 0.4 μm for the patterned lines. Diffuseness of the XRD patterns indicated no significant texture in the films. An important limitation of their work, is that no microcantilevers were actually patterned and tested; all of their testing was done at wafer level.

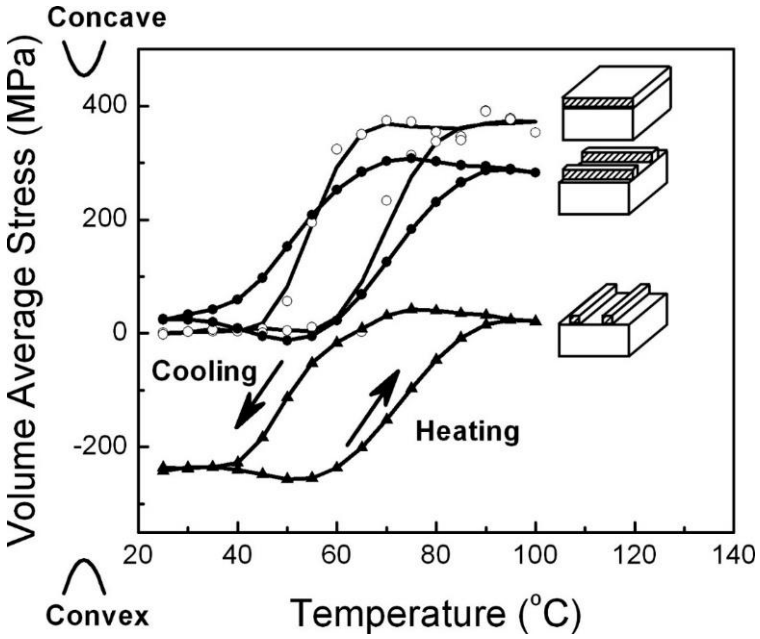

Figure 11. The volume average stress as a function of temperature for a continuous film and micron-lines measured parallel and perpendicular to their length adapted from [84].

Effects of Fatigue on NiTi:

Although fatigue is not the main focus of this body of work, it is nonetheless important to highlight the practical engineering aspects of using NiTi in high cycle applications. Of particular relevance to this PhD study is thermal fatigue; defined as the operation of NiTi actuator over many heating and cooling cycles. DSC has shown that NiTi transformation temperatures decrease over the course of just 100 thermal cycles, for the case of unstressed NiTi. The mechanisms are a bit more complicated in thin films under constant bias stress/strain during thermal cycling. Thermal fatigue, mechanical fatigue [137]. Dislocation density increased from ~10^{10} to 5x10^{14} after 100 thermal cycles. The observations of dislocation bands suggest that the moving martensite interfaces act as crystallographic ‘‘snowplows’’ that force the <100> (011) shear loops to slip (and cross slip) and then become locked in the sessile bands at the interface plane. During subsequent

transformation cycles, additional dislocation debris becomes more tangled, shorter, and more curved after multiple cycles. These dislocations further impede the motion of the martensite interface, thereby requiring a larger driving force, and consequently lower temperatures, to initiate transformation. Hamilton et. Al looked into functional fatigue of NiTi films on Si substrate up to 100 thermal cycles [138].

Ultralow fatigue SMA [139] is important for high cycle applications such as elastocalorics cooling [140] and stents. Ternary [139], and quaternary alloys based on NiTi have been developed for these purposes [141]. Transformation-induced plasticity during pseudo elastic deformation in NiTi microcrystals was shown, where they utilized a single crystal NiTi pillar ~20 μm diameter that was FIB milled from a polycrystalline sample with grain sizes > 200 μm, which was facilitated by a 20 hour anneal at 1,000 °C and rapid quenching to avoid the formation of precipitates (since extended time in the precipitate-stable region of phase diagram would lead to formation of precipitates). It is generally agreed in the community that as long as strain is kept below 1 – 1.5%, then cycle times can go well into the millions.

1.3. Photothermal Actuation of MEMS cantilevers

Photo thermal (i.e. laser induced heating) actuation allows for a wireless means to harness directed energy over large distances. Optical actuation (i.e. folding or bending) has been shown in shape memory alloy (SMA), other polymers (albeit slow actuation), thin metal films, and carbon nanotubes. One major drawback in some of these applications was the need for mirrors or lenses to focus laser beam to 100 - 1000's of W/cm^2 [142]. It would be advantageous if laser actuation thresholds could be lowered to 10's of W/cm^2 or less. In this dissertation, microsecond actuation time scales with irradiation levels below $5W/cm^2$ is demonstrated. The SMA actuation response was shown to be faster than 100 ms, with irradiance levels as low as 2 W/cm^2.

Lasers can be used to heat MEMS cantilever like devices [143-145]. Lasers were used to soften polymers and allow bending of microgrippers that were actuated due to residual stress in thin films [76, 77, 79, 80, 146]. Stressed Cr was used to bend a "hinge" in MEMS structure. Wireless bimorph actuated MEMS bimorph cantilevers (BMC) were actuated with a pulsed laser [147]. They used Au on Poly-Si cantilevers based on Poly-MUMPS process. Nd:YAG laser of 355 nm wavelength and 12 ns pulse was used to heat the bimorph device. Cantilevers varied in length (1 mm, 850 um, and 500 um). Poly-Si was 1.5 μm thick, Au was 500 nm thick. Devices released with upward curl due to residual stresses developed in the process. ~85 μJ per pulse (1 mm diameter laser) generated max displacements of 100 μm in the 1,000 μm length BMC. The authors claimed this opens up wireless microactuation (i.e. micropumps or micropropellers).

Optical actuation of micromirrors fabricated by micro-origami technique was shown in [148]. The most deflection they were able to achieve in a rigid micromirror was 0.5 deg. This was at an optical power density of ~400 mW/mm^2. The Air Force Research Lab MEMS group published a paper on thermally-actuated micro-shutter for MOEMS applications [149]. These used joule heating and traditional thermal actuators based on hot and cold beams.

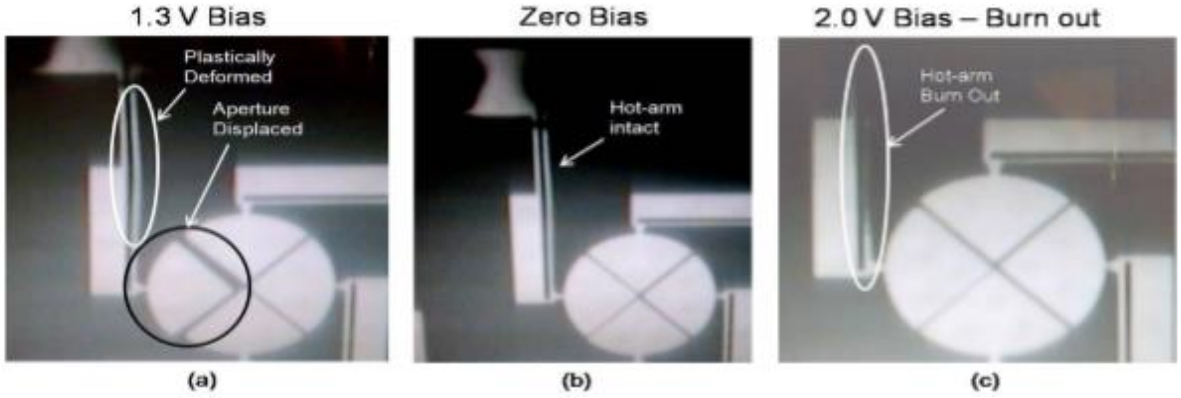

Figure 12. MOEMS shutter actuated with 1.3 V DC bias. This group had fabrication issues where the device would collapse into the substrate due to stiction and lack of rigidity in the 1.0-1.5 µm thick Al film. From [149].

An additional concept for MEMS shutter was the electrostatic, artificial eyelid. Using stressed sheets of rolled up thin films, these devices were limited in success because they required 100 - 300 V in order to actuate [150] and would more often than not stick to the substrate and not return after the voltage load was removed.

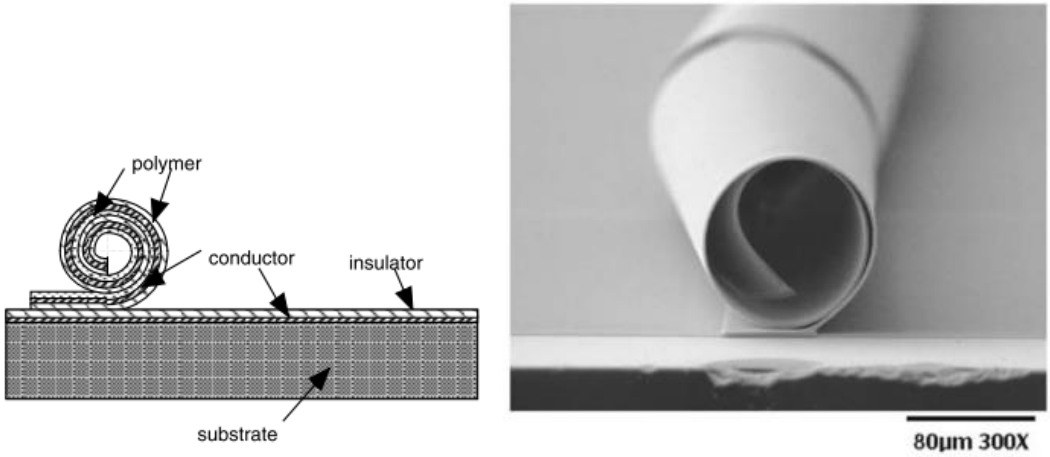

Figure 13. Electrostatically actuated MEMS shutter eyelid for sensor protection from [150].

Another type of microshutter array was developed by NASA for James Webb Space Telescope [151]. In this design, the microshutters can be selectively addressed using a combination of electrostatic and magnetic forces.

Baglio et al. showed Modeling and design of novel photo-thermo-mechanical microactuators [152]. One huge disadvantage to their approach was the need to micro machine lenses to focus the light source onto the suspended MEMS cantilever. Also, not all radiation is absorbed: consider for example in the visible spectrum that Al reflects about 90% of light, therefore the absorption coefficient would be 10%.

In a non-MEMS application [153], a bulk SMA spring was actuated with laser powers ranging from 5 – 50 W with bias loads of 1.5, 2.5, and 3.5 N to deform the spring at room temperature in martensite phase. Upon laser irradiation, a temperature rise converted NiTi into austenite phase and a maximum displacement of ~30 mm was measured. A COMSOL Multiphysics model was used to study the heat generated during laser irradiation.

The electrostatic artificial eyelid requires more than 100 V to actuate which limits practicality [154]. In one journal paper a digital micromirror device (DMD) in combination with wavelength multiplexing allowed for selective spectral filtering in defined regions of interest in the scene. The system offers the possibility of automatic attenuation of dazzling laser radiation in the visible spectrum [155]. One paper looked at a comparison of various methods to protect sensors from laser dazzling [156]. Some of the mentioned benefits of a MEMS thermal shutter was fast response and wavelength agnostic operation principle. In 2009 a MEMS thermal shutter was presented [149]. Another paper titled “Complex MEMS device: microshutter array system for space applications” summarized the recent developments of the JWST microshutter arrays

developed by a large team of NASA scientists and engineers [151]. An earlier work (1996) entitled Remote optical detection using microcantilevers [157] started simply with COTS AFM cantilevers. A laser beam with 6 mm diameter, 786 nm wavelength, and cantilevers ranging from 180 - 320 μm in length. Excitation (or pump laser) was modulated from 1-100 Hz. Peak power was 18.5 mW, equating to 65 mW/cm^2. Au/Cr was the bimorph element. SiN was 600 nm thick. Cantilevers were 18 μm wide, spring constant (i.e. bending force) of ~ k = 0.01-0.02 N/m.

Additionally IR laser actuation of bimetal cantilever was used to close a switch in [158]. They showed a remarkable power threshold of ~500 nW. 50 nm thick Au patches formed plasmonic absorption structures, and a small air gap of ~500 nm required only very small deflections of the bimorph to "close the switch".

Several mechanisms are at play with "optical actuation" in MEMS: light radiation pressure (negligible because the photon mass is much less than MEMS structure), photo induced stress, and thermal expansion by heating. To put some numbers to the "light pressure", consider the experiment by [148], where F=(PA)/c, P is light power density, A is mirror (or irradiated area), and c is speed of light. At P = 450 mW/mm^2, A=5E^{-3} mm^2, then F = 7.5 E^{-6} μN, which causes negligible deflection. Therefore, actuations can be primarily attributed to thermal mismatch or phase-change effects.

1.4. Summary of Literature Review and Aim of Dissertation

After a thorough review of the prior literature, several research opportunities were identified which would benefit the community at large. Specifically, if the processing temperatures of NiTi SMA could be lowered, then NiTi could be practically integrated with material sets that

the high processing temperatures of SMA current preclude. These additional platforms or materials sets would include CMOS and soft polymer materials.

At the onset of this PhD endeavor, the fundamental limitations for shape memory MEMS were related to 1) how thin could one go and still be able to measure reversible shape memory effects, 2) how fast could one conceivably actuate the SMA MEMS device (limitations previously existed that would not allow for heat transfer to happen much faster than several 10s, or at most, 100 Hz, and 3) could a micromirror be fabricated using shape memory alloy and demonstrate large, reversible deflections for future applications in beam steering, LIDAR, and medical imaging. By shrinking the volume and heat capacity of the SMA MEMS actuators, it was shown for the first time, that reversible actuation beyond 1 kHz frequencies was possible, verifying that the heat transfer (in other words, the heating and cooling of shape memory alloy), could happen more than 1,000 times per second. Combined with SMA's natural advantages of large displacements, and high work densities, the efforts laid out in this dissertation have demonstrated major breakthroughs in the bandwidth, or speed with which NiTi could be actuated, and thus enabled additional possibilities to use NiTi in microelectronics and MEMS. Shape memory MEMS can certainly now be used for higher frequency actuation applications such as mechanical logic, signal routing, and switching, and at relatively low power and energy consumption.

In this PhD dissertation, specific focus is placed on the extrinsic biasing mechanism enabled from residually stressed or CTE mismatched materials. SU-8 negative epoxy photoresist can be patterned and developed on top of Nitinol, and based on post-bake temperatures around 200°, and the unusually high CTE of SU-8 (~52 ppm/K), to cause significant upward curl in Nitinol MEMS bilayer actuator. In each of these cases, the NiTi is crystallized, or shape set into a flat configuration, MEMS patterned into a suitable size, and then biased into a bent configuration upon

device release. This clever setup achieves a relatively simple bilayer actuator that can be thermally actuated between curled and flat states based on the reversible phase change inherent to Nitinol, and the biasing stress to enable extrinsic two-way shape memory effect (TWSME). For example, without the constant biasing force, the Nitinol actuator could only exhibit the one way shape memory effect (OWSME).

This PhD dissertation demonstrated stressed metal films and stressed SU-8 on NiTi bimorphs capable of reversible actuation. This resulted in tight radius of curvature actuators that were not possible in those previous demonstrations using relatively thick and rigid Si cantilevers as the bias spring. By using thin (~1 μm) and low modulus materials like SU-8, and ultra-thin stressed metals like (Cr and Pt), we achieved large, reversible bending of NiTi film actuators at MEMS scale.

In Chapter 2, low-temperature crystallization (as low as 325 °C) is shown on metallic seed layers which enable epitaxial growth of nanoscale thickness SMA films exhibiting reversible phase-change.

Additionally, there is significant room for improvement in SMA MEMS frequency response as well as a need to reduce the optical irradiance required to induce thermal phase-change. To address these limitations, in Chapter 3, MEMS bilayer actuators are fabricated and due to their extremely low volumes, they are able to be actuated with low power laser irradiation. Chapter 4 demonstrates the low power and fast cycling of SMA MEMS by way of joule-heating. In this chapter, pulsed electrical currents are used to generate heat in the NiTi actuators allowing for the study and characterization of high-frequency actuation. An impressive cycling bandwidth up to 3 kHz was demonstrated, advancing the state of the art.

Finally, Chapter 5 documents the first attempts at fabricating and characterizing an SMA-activated micromirror array device. Due to impressive deflections offered by SMA phase-change, a mirror was deflected up to 29.9 degrees of rotation which based on developments in Chapter 2-4, should be capable of fast and low power application suitable for power constrained environments (i.e. on-chip).

Chapter 2: Fabrication and Characterization of NiTi thin film SMA

As highlighted in the Introduction, Shape memory alloys (SMA) are a class of functional materials characterized by their "memory" of a previous structure after a first-order phase transformation. During this thermally-driven austenite <> martensite transition, recoverable stress is built up within the film, which can be manipulated to do work. NiTi, one of the most widely studied SMAs is known for its exceptional chemical resistance, highest work output per unit volume, and bio-compatibility, with great potential for applications in the medical, aerospace, and robotics industries. Thin films of SMAs have also shown promise for applications in MEMS devices requiring friction free, large displacement, and non-vibrational movements. However, applications of NiTi films remain limited due to high deposition temperatures (>425 °C) required to achieve a high degree of crystallinity to attain the critical SME. Most of the studies have focused on either substantially thick films (>2 μm) which reduce flexibility [53, 133, 159, 160], or post-annealing methods where the temperatures are still above the NiTi crystallization temperature (425 °C) [87, 161]. Deposition and post-annealing processes at high temperatures have several disadvantages. The choices of available substrates are limited, as materials (such as polymers) which degrade at high temperatures cannot be utilized. High residual stress due to thermal gradients can also result in warps or cracks in the film. Furthermore, formation of unwanted complex precipitates can occur at the interface caused by reactions with the substrate which reduce the thickness of the active NiTi layer contributing to SME.

This work explores nanoscale thickness NiTi SMA films deposited at temperatures ranging from 325 °C to 800 °C and thicknesses ranging from 120 nm up to 1.6 μm. The thicker NiTi films deposited at higher temperatures are used to confirm the SME. These developments are documented in Section 2.1 and served as a reliable basis from which the necessary reductions in

temperature and thickness were explored. Section 2.2 details the use of thin metallic seed layers such as Ru and Pt, which served as a pseudo-epitaxial layer to enable crystallizations at lower deposition temperatures. In this section, NiTi films were confirmed to have reversible shape memory effects in films as thin as 120 nm at processing temperatures as low as 325 °C. Finally, Section 2.3 documents characterizations related to NiTi films sputtered onto polyimide (PI) films at temperatures as low as 400 °C and as thin as 400 nm proving that shape memory effects can be achieved when directly deposited onto soft polymeric materials.

2.1. Co-sputtering of NiTi and Ti target onto Si wafer

In this section NiTi films are sputtered onto Si wafers and characterized using stress versus temperature, XRD, and transmission electron microscopy (TEM) methods. Figure 14 shows a schematic of the AJA co-sputter tool used in the development of NiTi SMA film recipes. Substrate rotation was used to maintain high uniformity. Co-sputtering was performed using DC magnetron sputtering from an equiatomic NiTi target and pure Ti target in order to finely tune the films' composition. TEM was performed in order to gain additional insights into the crystallization of NiTi on Si (100). Three samples were analyzed, all of which were deposited for one hour onto Si (100) wafer in heated substrate conditions at 600 °C, 700 °C, and 800 °C. Based on a very thorough literature review, and the additional suite of characterizations performed, crystallization in each of the samples was expected to be apparent.

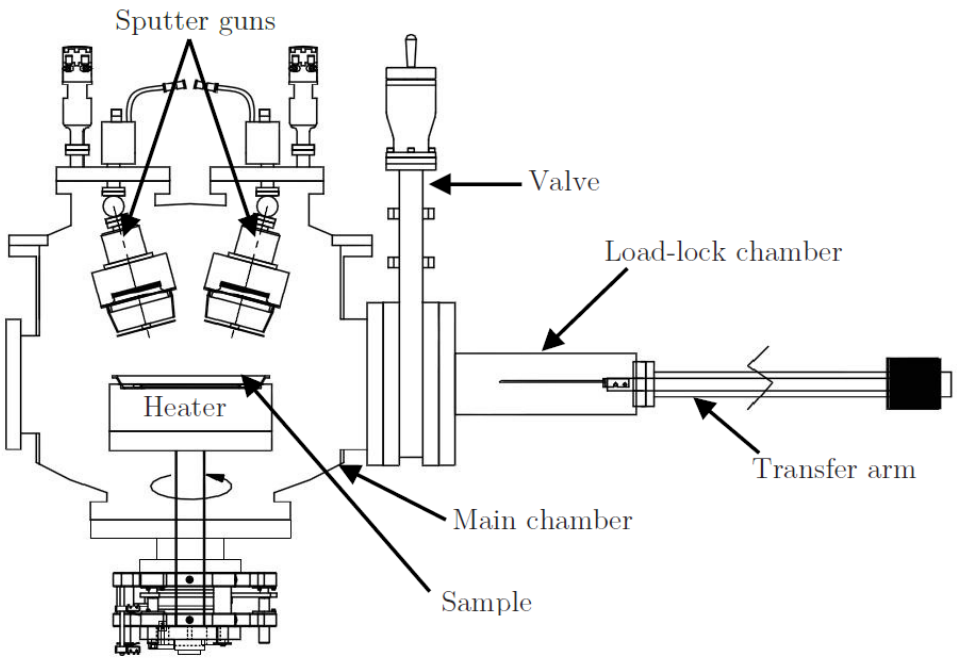

Figure 14 Schematic of AJA co-sputter tool used in the development of NiTi SMA film recipes.

Figure 15 shows the TEM data for NiTi on Si (100) for the 800 °C sample. Thickness was revealed to be 824 nm. In Figure 15A the martensite structure is observed for image recorded at room temperature. In Figure 15B the columnar structure with ~100 nm grain width was revealed for sample imaged at 150 °C, corresponding to the austenite phase. In Figure 15C the equiaxed grains were apparent at the NiTi Si interface, as was the interfacial region where intermixing at high temperatures is expected to happen.

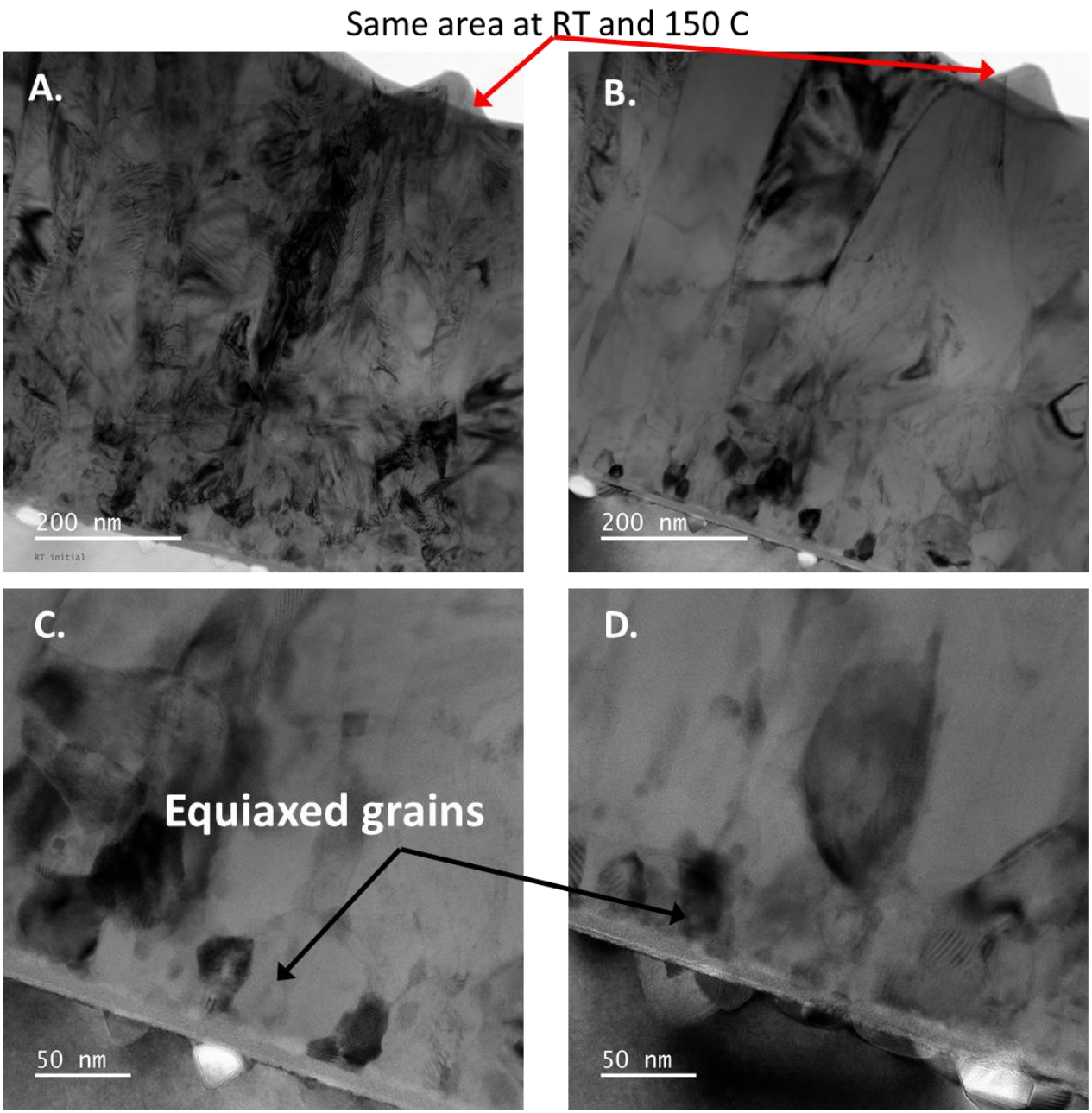

Figure 15. TEM of NiTi on Si (100) sputtered at 800 °C. A) RT martensite structure B) austenitic, columnar grains at 150 °C, C) equiaxed grains near NiTi Si interface and D) equiaxed grains at 150 °C in austenite phase.

There appeared to be a layer of equiaxed grains at the bottom of the film, where NiTi is grown on Si. Figure 16 shows TEM of NiTi on Si (100) sputtered at 700 °C. In Figure 16A the RT martensite structure was apparent, and film thickness was measured to be 880 nm. In Figure 16B

the austenitic phase, columnar grains at 150 °C were approximately 215 nm in width, or about twice as wide as was measured in the 800 °C sample. In Figure 16C equiaxed grains near NiTi Si interface were apparent. Note: during TEM sample prep, all but the bottom ¼ NiTi film was accidentally removed. In Figure 16D equiaxed grains were observed at 150 °C in the austenite phase.

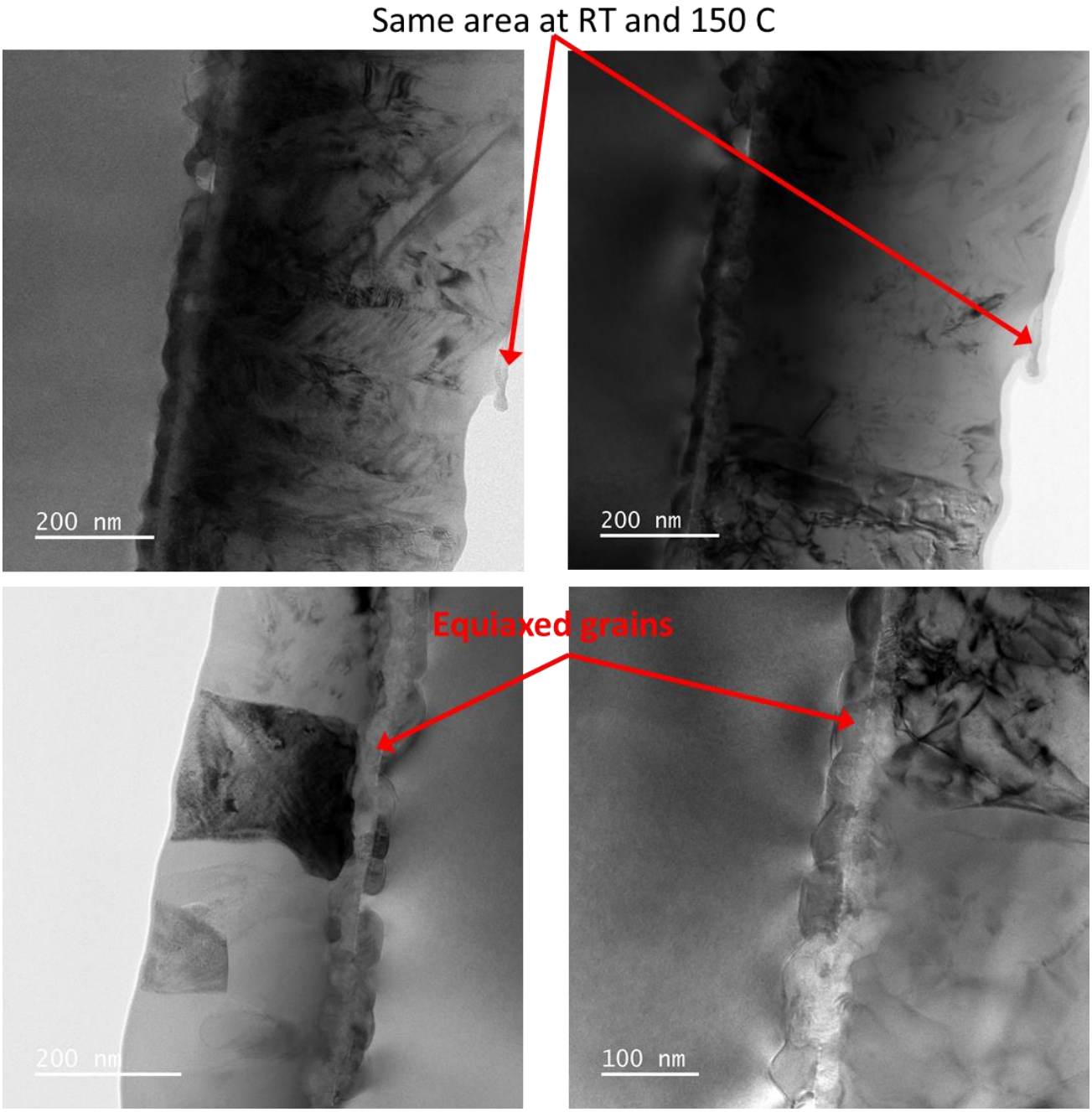

Figure 16. TEM of NiTi on Si (100) sputtered at 700 °C. A) RT martensite structure B) austenitic, columnar grains at 150 °C, C) equiaxed grains near NiTi Si interface and D) equiaxed grains at 150 °C in the austenite phase.

Figure 17 shows a combined plot of four wafers showing excellent repeatability in the NiTi film stress versus temperature plots. Two NiTi wafers were sputtered at 700 °C, and two wafers were sputtered at 800 °C. All other deposition parameters were fixed between all four sputter runs: 5 mTorr chamber pressure during the sputtering, 60 sccm Ar flow, 60 minutes deposition time, 375 W to the NiTi target, and 250 W to the Ti target. Some interesting results were apparent when comparing the sputtered NiTi at 700 °C and 800 °C. The NiTi films seemed to have very comparable residual stress (~50 MPa), but one main difference is the 800 °C sample had an additional ~100 MPa recovery stress. Based on the shape of the curves, this could be attributed to the presence of R-phase in the 800 °C sample. This was confirmed in other samples where only R-phase <> austenite transformation happened above room temperature. In each of these many cases, the narrow hysteresis transformation is ~100 MPa. The R-phase is indicated by the additional, narrower hysteresis portion of the SMA curve. The 800 °C sample had a recovery stress of ~450 MPa and the 700 °C sample had recovery stress of ~350 MPa. All other recipe parameters were held fixed therefore it was concluded that deposition temperature alone can significantly impact the nature of the shape memory effect.

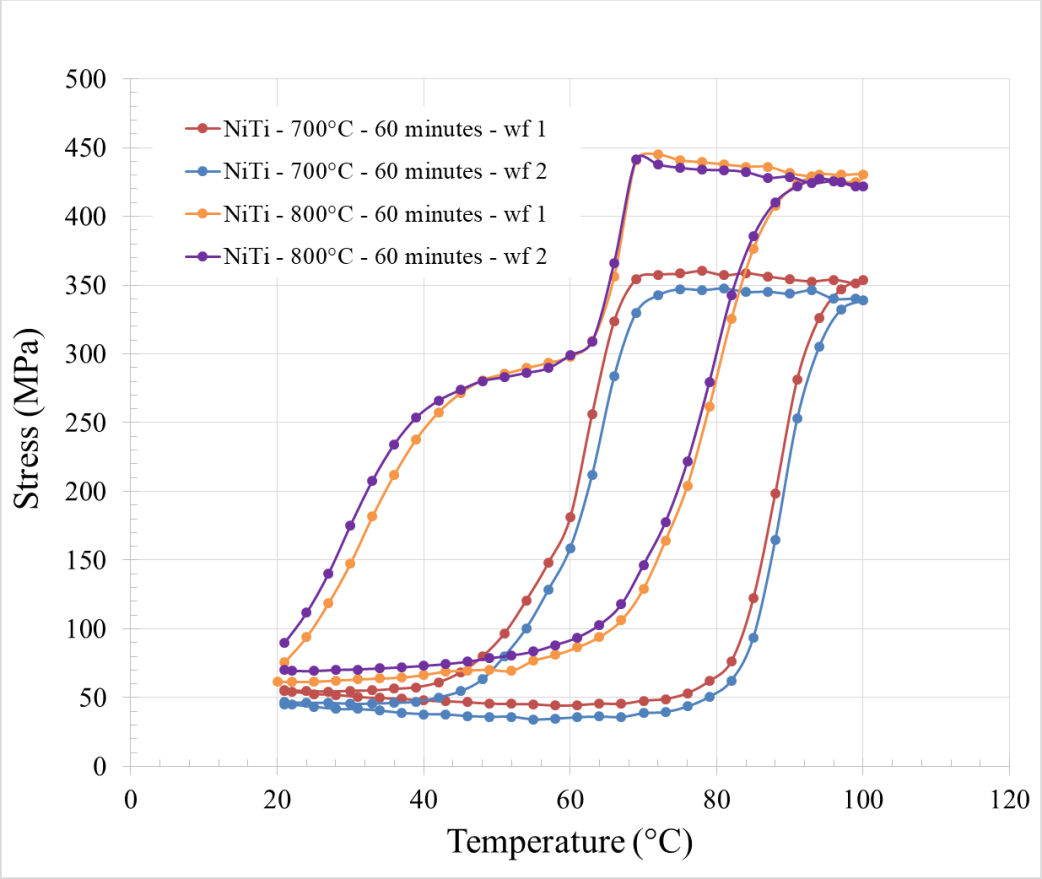

Figure 17. Plot of 4 wafers showing excellent repeatability in the NiTi film stress vs. temperature plots: 2 NiTi wafers sputtered at 700°, and 2 wafers sputtered at 800°C; all other deposition parameters fixed: i.e. 5 mTorr, 60 sccm Ar, 60 minutes deposition, 375 W NiTi, 250 W Ti.

In this section, it was shown that NiTi films deposited onto Si are crystallized and exhibit reversible shape memory effects. Reversible shape memory effects were verified using stress-bow measurements on 4 inch Si wafers coated with NiTi. TEM was used to characterize the NiTi microstructure in martensite and austenite phases. Grains are columnar through a bulk of the thickness, whereas grains in the vicinity of the NiTi-Si interface are equiaxed. Interfacial diffusion was observed at the NiTi-Si interface whereby non-uniform regions of intermixed NiTi and Si were apparent. The following section seeks to mitigate some of these effects through the use of metallic seed layers and reduced temperature depositions. This resulted in epitaxial SMA films

exhibiting reversible shape memory effects at temperatures as low as 325 °C and as thin as 120 nm.

2.2. Co-sputtering of NiTi and Ti target onto Pt and Ru seed layers

There is great interest for integrating NiTi with a variety of MEMS and complementary metal oxide semiconductor (CMOS) devices. One significant limiting factor for NiTi integration is the maximum processing temperature allowed based on various substrates or materials already employed. For example, "soft" substrates like SU-8 or polyimide are often times employed as a MEMS device release layer. Typically SU-8 and PI materials are only stable up to about 300 - 350 °C, above which they experience out-gassing, softening, reflow, significant weight loss, etc. Eventually these materials will melt, so typical SMA crystallization at 500-600 °C is completely prohibited. Recent studies have shown that the presence of a seed layer, such as Pt, significantly increases crystallization of films with sub-micron thickness [39]. Seed layers can also mitigate the formation of precipitates at the film-substrate interface, as well as assist in nucleation of nano-crystallites [162, 163].

To this end, NiTi films were sputtered onto Pt and Ru seed layers in attempt to enable thinner, and lower deposition temperatures to enable SMA integration with a wider variety of substrates including polymers and CMOS. NiTi films were crystallized *in-situ* at deposition temperatures of 325 °C, 450 °C, and 600 °C. The growth and characterization of NiTi thin films using a Ru seed layer with deposition temperatures as low as 325 °C is reported, demonstrating this method is viable for integration into polymer based MEMS fabrication. The dependence of crystallinity and shape memory properties on the deposition temperature (T_D) and film thickness (t) were investigated. Stress-bow, resisitivity and x-ray diffraction measurements were utilized to characterize deposited thin films across the austenite to R-phase transformation. This section

demonstrates that by utilizing a Ru seed layer with a thinner Ti-rich NiTi film (120 nm), crystalline films with good shape memory effect can be achieved. These findings were published in [164].

2.2.1. Sample Preparation

Ti-rich NiTi films were deposited on to (100) silicon wafers coated with a 5 nm thick Ru seed layer (deposited by e-beam evaporation) using DC magnetron co-sputtering of NiTi and Ti targets in the AJA ATC 2200. The Ru seed layer was deposited by thermal evaporation on to Si substrates. During sputtering, dual targets of equiatomic NiTi (375 W) and pure Ti (240 W) were used to compensate for the lower sputtering rate of Ti. The working pressure was set to 5 mTorr while deposition temperature (T_D) was varied from 325 °C to 600 °C. Thickness of the deposited films ranged from 120 nm to 450 nm (controlled by deposition time) and were confirmed by profilometry and SEM cross section. Elemental compositions of films were measured using energy dispersive x-ray spectroscopy (EDX) and are within an error margin of (+/- 1 at.%). Table 1 lists all the measured samples along with their deposition temperature, thickness, and composition. Table 2 lists the corresponding measured grain size in the B2-phase.

Table 1 deposition parameters and composition of NiTi films grown on Ru seed layer

Sample ID	T_{Dep} (°C)	t (nm)	Comp. Ti/Ni (at.%)
Ru600_225	600	225	54/46
Ru400_225	400	225	53/47
Ru325_120	325	120	54/46
Ru325_225	325	225	54/46
Ru325_450	325	450	54/46

Table 2 measured grain size for NiTi on Ru films deposited at temperatures between 325-600°C.

Sample ID	Avg. Grain Size (nm)
Ru600_225	450
Ru400_225	120
Ru325_120	25
Ru325_225	35
Ru325_450	70

Table 1 illustrates the composition of each film is consistent and Titanium rich. This has been shown elsewhere to facilitate crystallization at lower temperatures [23, 51]. Marked improvements in average grain size as deposition temperature is increased can be seen in Table 2. For the fixed deposition temperature (325 °C, the lowest considered in this study), the average grain size was shown to increase as the deposition time increased, consistent with longer time and temperature for the annealing and grain growth.

2.2.2. Characterization

Crystal structure during phase transformation was measured using X-ray diffraction at Beamline 2-1 at the Stanford Synchrotron Radiation Lightsource (SSRL). Grazing incidence x-ray diffraction (GIXRD) measurements (E =17 keV) were conducted during heating and cooling cycles with a temperature range of 26 – 120 °C and rate of 1 °C/min. Depending on the thickness of the film, incidence angle for x-rays was varied between 0.7° and 1° to tune the attenuation length through the film, mitigating signal contribution from the Si substrate. Average grain size for the B2 phase was calculated using Williamson-Hall plots.

Resistivity was measured with four point probe method using the Quantum Design Versalab system with Electrical Transport Option (ETO). In order to investigate the stability of transformation over multiple cycles, resistivity scans in temperature range of 25-100 °C were measured with a ramp of 1 °C /min. The first derivative of resistivity as a function of temperature

was calculated to obtain accurate phase transition temperatures, similar to methods using tangent lines [10]. Hysteresis width was defined as the finish temperature of the phase transformation upon heating minus the start temperature of the transformation upon cooling.

In order to study the martensitic transformation, wafer curvature measurements were performed as a function of temperature. Stresses induced by phase transformations were measured through wafer curvature method using the Toho FLX-2320-S film stress measurement system. The temperature range was set between 20 °C and 100 °C with a rate of 1 °C/min. As the Si substrate is three orders of magnitude thicker than the film, Stoney's equation was utilized to convert the radius of curvature to film stress.

Samples were prepared by sputtering NiTi onto a Ru seed layer on Si wafer as detailed in Table 1. Figure 18 shows the evolution of film stress across the phase transformation. Figure 18A compares films with different deposition temperatures (T_D =600 °C, 400 °C, 325 °C) for same film thickness (225 nm), while Figure 18B compares films with different thickness (t = 450 nm, 225 nm, 120 nm) for the lowest deposition temperature (T_D = 325 °C). The sharp variations in stress indicates a phase change. Figure 18A shows that the NiTi film with T_D = 600 °C (Ru600_225) has the largest recovery stress of 225 MPa with a hysteresis width of 24 °C, characteristic of an austenite (B2) to martensite (B19') transformation. As T_D decreases, a two-step transition is observed for Ru400_225, which further collapses to a much smaller recovery stress profile for Ru325_225. On the other hand, in Figure 18B, a stable transformation hysteresis is observed between 55 °C and 64 °C showing that SME is present in all the thin films with the lowest T_D of 325 °C. Here we note that NiTi films with lower thickness show higher residual stress, whereas films with higher thickness show lower residual stress possibly due to strain relaxation away from the Ru/NiTi interface or precipitate effects as discussed in a later section.

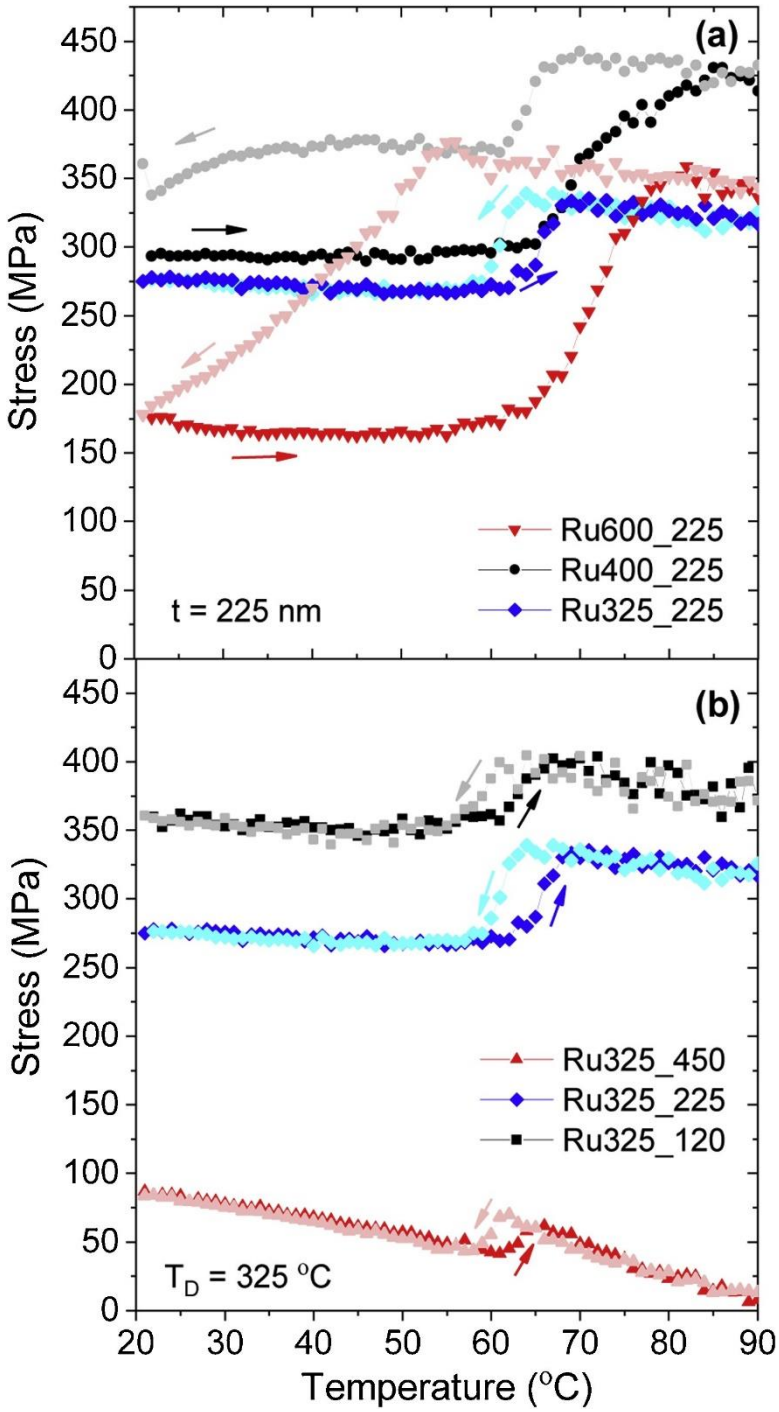

Figure 18 stress vs. temperature measurements for the NiTi on Ru wafers as reported in our paper on ultra-thin, low temperature crystallization of NiTi on Ru seed layer [164]

2.2.3. Characterization by GIXRD measurements

Figure 19 shows GIXRD spectra for NiTi films measured at temperatures below (black) and above (red) the phase transformation. Figure 19A compares NiTi thin films with 225 nm thickness for different values of T_D, while Figure 19B depicts NiTi thin films with varying thickness at a fixed T_D of 325 °C. These spectra were recorded during the heating and cooling cycle from 120 °C to room temperature (only cooling data is shown in Figure 19). For all the samples, R-phase, metastable phase of trigonal structure, was observed at 40 °C with the characteristic (300)R diffraction peak being the most pronounced. Here we note that the subscripts R and C refer to the Miller index notation for the trigonal and the cubic B2 structures respectively, and will be used throughout the section. A shift of (300)R diffraction peak to (110)C diffraction peak was observed upon heating and vice-versa. (3 0)R, (3 2)R, and (232)R diffraction peaks exclusive to R-phase were also observed at room temperature, which subsequently disappeared above the phase transformation temperature. The shift of the (300)R peak and the intensity of the (3 0)R peak during the cooling and heating cycle are plotted in Figure 20. Figure 20B clearly shows that the peak shift from B2 ↔ R is discontinuous with temperature and is not due to thermal expansion. It can be also seen that as T_D decreases the B2 ↔ R transformation temperature slightly decreases and hysteresis width narrows. Average grain size for the B2 phase using Williamson-Hall plots is shown in Table 2. Larger grain size is observed for thin films deposited at higher T_D. Bragg peaks for Ti_2Ni precipitates were also observed in all the films.

The diffraction intensity for the precipitate peaks was dependent on the film thickness and T_D, increasing for higher T_D and thicker films. These precipitates have been previously reported in literature for Ti-rich composition [23, 51, 165]. Interestingly, additional Ti_2Ni peaks were observed for Ru325_450, signaling a more granular precipitate structure that is less coherent with the NiTi matrix. The overlap of some of the Ti_2Ni precipitate peaks with B19' phase peaks makes

it extremely difficult to deconvolute the presence of B19' phase at lower temperatures. However, based on stress-bow measurements (Figure 18), which show narrow and single-step hysteresis loops for all the samples except Ru600_225 and Ru400_225, we can infer that the B19' is absent. Ru600_225, as mentioned above, shows the largest recovery stress of 225 MPa with a wide hysteresis which is a characteristic of a B2 ↔ B19' transformation. This combined with x-ray data indicates towards the coexistence of both R and B19' phase at room temperature. For Ru400_225, GIXRD data at room temperature shows presence of R-phase. Although two-step hysteresis loop in stress-bow measurement could potentially indicate partial transformation from R-phase to B19' near room temperature. This interpretation is also corroborated by electrical resistance measurements. For thin films deposited at 325 °C additional Bragg peaks from TiO_2 were also observed. Although, as it mostly forms on the surface post-deposition, it is not expected to influence the phase transformation.

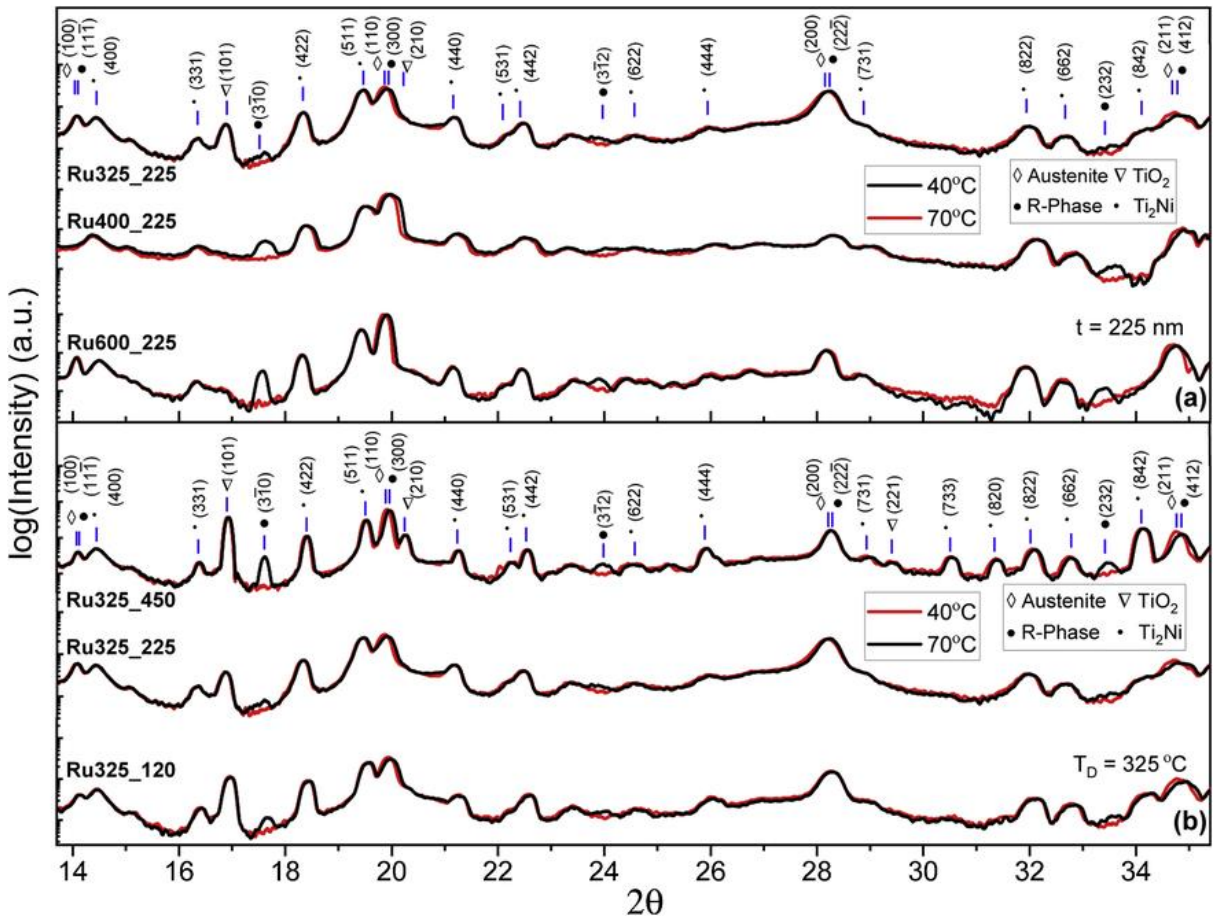

Figure 19. GIXRD spectra above and below R to B2 transformation: (a) NiTi films with different deposition temperatures, T_D = 600 °C, 400 °C and 325 °C, and same film thickness, t = 225 nm, and (b) NiTi films with different thickness t = 450 nm, 225 nm, 120 nm for lowest deposition temperature, T_D = 325 °C.

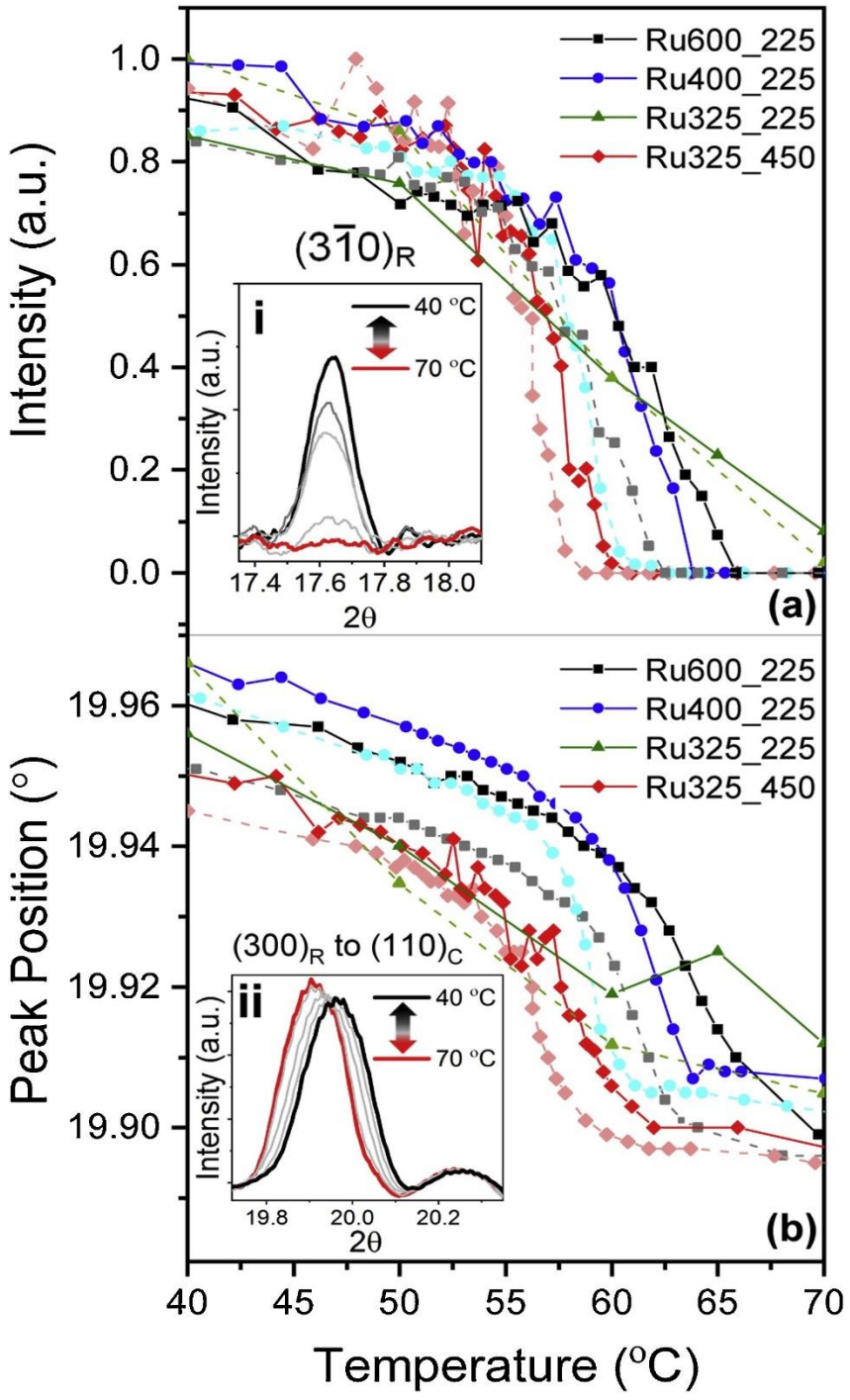

Figure 20. Peak position shift in the NiTi on Ru samples showing transformation between austenite and R-phase as reported in [164].

Pt is one of the only reported metallic seed layers to date regarding NiTi crystallization. Kim showed that by using a Pt seed layer, NiTi films (Ti-rich composition) could be crystallized at deposition temperatures as low as 350 °C, although the shape memory effects were not reported on [39]. They had chosen Pt as a seed layer for the following reasons: ease and availability of Pt synthesis, low specific heat and high conductivity for improving heat dissipation. Theories behind lowered crystallization temperatures are based around surface energies between NiTi and Pt. The interfacial energy of NiTi / Pt is hypothesized to be lower compared to NiTi / Si and NiTi / SiO_2 (common substrates for NiTi depositions), making the overall activation energy barrier for nucleation on Pt lower. In addition to Pt, this work compares against Ruthenium (Ru) seed layers as well. Ru was chosen as an additional transition metal which was readily accessible and easy to deposit by e-beam evaporation techniques. The ultimate goal of this effort was to push towards a thinner NiTi film, targeting 100 nm thickness and progressively lower T_D and still exhibiting SME.

Figure 21 shows XRD plots for NiTi deposited onto (a) Pt and (b) Ru seed layers at substrate temperatures of 500 °C, 400 °C, and 325 °C. NiTi films with T_D = 500 °C showed clear martensitic transformations for NiTi films on Pt and Ru when contrasting XRD spectra taken at RT and 130 °C as shown in Figure 22. The films undergo a clear B2 <> R transformation. R-phase diffraction peaks are apparent in the RT spectra.

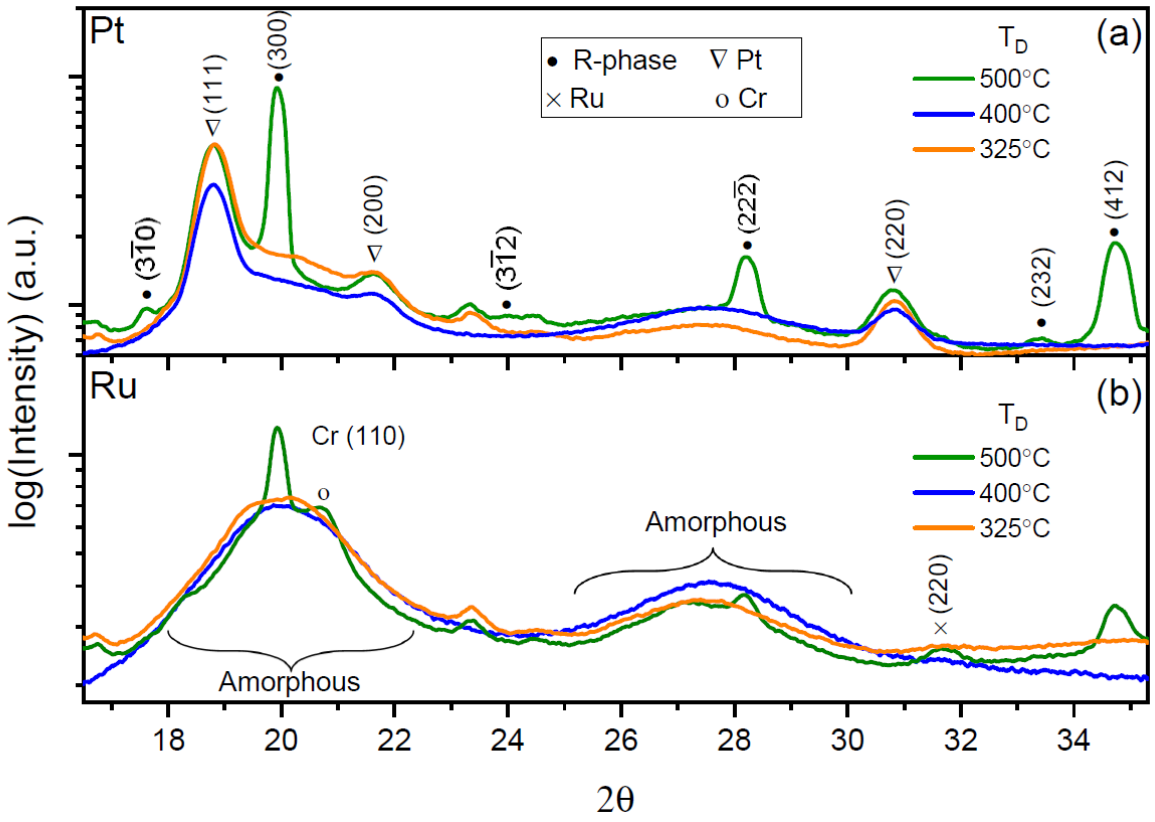

Figure 21 XRD plots for NiTi deposited onto (a) Pt and (b) Ru seed layer at substrate temperatures of 500, 400, and 325°C

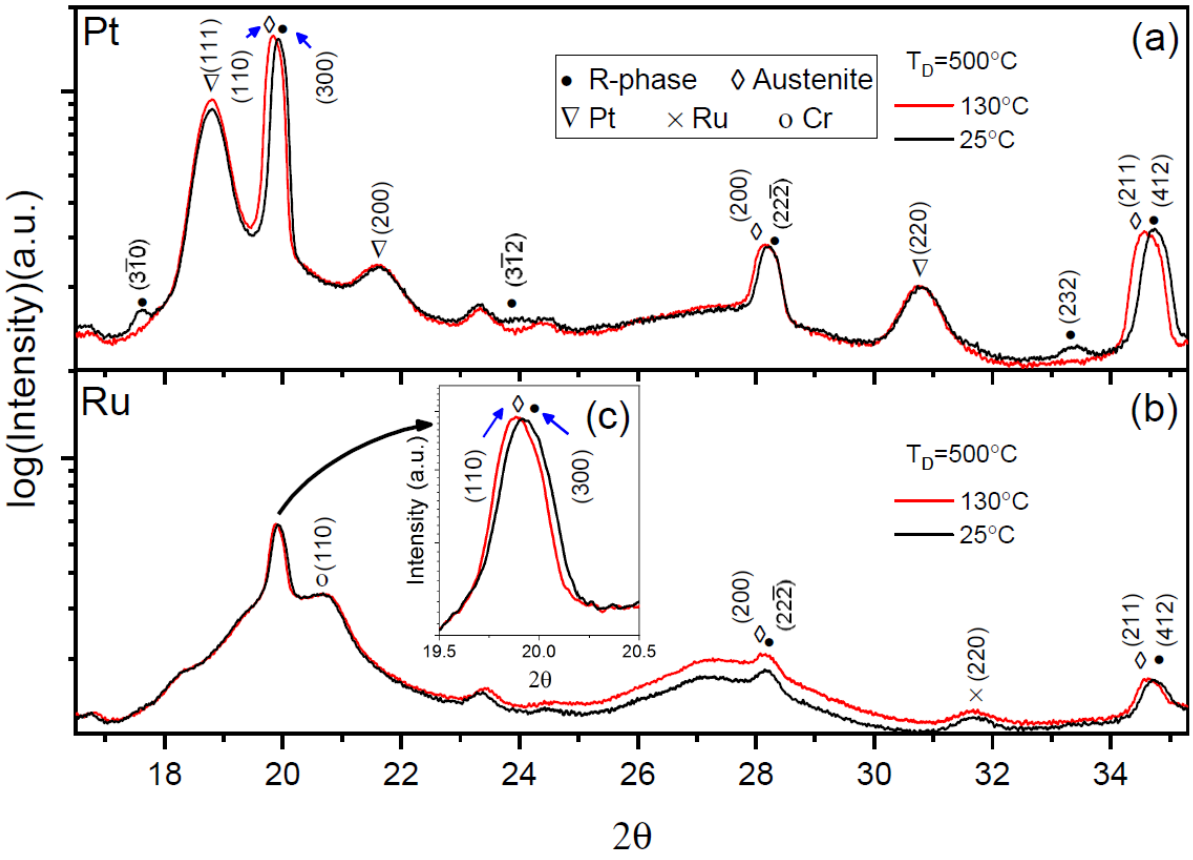

Figure 22 XRD plots (utilizing SSRL beamline) for NiTi on (a) Pt and (b) Ru showing reversible transformation between R-phase and austenite at RT and 130°C

Figure 23 shows the electrical resistivity ρ(T) measurements in the same temperature range as x-ray studies. Multiple cooling and heating cycles show that the phase change between B2 ↔ R-phase is stable. Transition temperatures during the heating and cooling cycle were obtained by taking the derivative of resistivity, (dρ/dT), as shown in Figure 23 f-j, and are reported in *Table 3*. For the cooling cycle, R_s denotes the temperature at which R-phase appears, and R_f marks the temperature when transformation to R-phase is complete. For the heating cycle, A_s denotes the temperature at which austenite appears, and A_f marks the temperature at which transformation to austenite phase is complete. It can be seen that for the same thickness, decreasing T_D results in

narrowing of the hysteresis width ($T_H = A_f - R_s$) while the temperature range ($T_{range} = R_s - R_f$) over which transformation occurs increases. For thin films with T_D = 325 °C, similar trend is observed, as the film thickness decreases, the hysteresis width narrows and the temperature range for transformation increases.

Two-step transition in ρ and (dρ/dT) is observed for Ru600_225 (Figure 23 a and f), indicating possible partial transformation to B19' phase. In addition, the continuous increase in resistivity for Ru400_225 following B2 to R-phase transformation, also points toward partial transformation to B19' phase. This is in agreement with stress-bow and x-ray studies, which indicate coexistence of R-phase and B19' phase for these two samples. A complete transformation to B19' phase is observed below room temperature in all samples as shown by resistivity measurements over a long temperature range.

Table 3. Measured transformation temperatures determined from electrical resistivity vs. temperature experiments.

Sample ID	Cooling		Heating		T_{range}	T_H
	R_S (°C)	R_f (°C)	A_S (°C)	A_f (°C)	(°C)	(°C)
Ru600_225	64	50	53	69	14	5
Ru400_225	62	56	58	65	5	3
Ru325_120	63	40	42	65	23	2
Ru325_225	59	25	26	60	28	1
Ru325_450	60	47	53	64	13	3

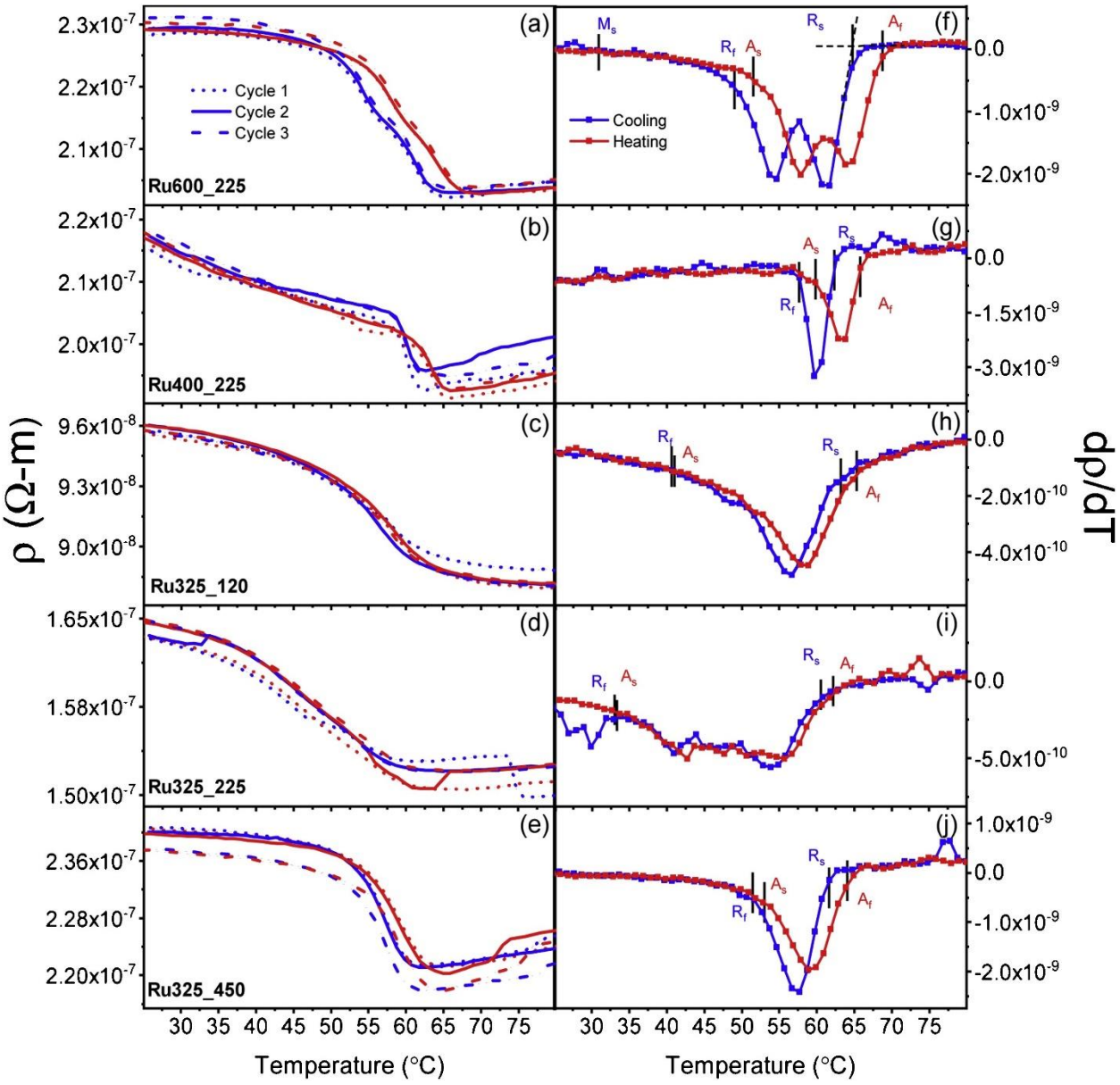

Figure 23. Electrical resistivity measurements for NiTi on Ru films showing reversible transformation between R-phase and austenite (with narrow hysteresis) as reported in our paper on controlling crystallization of NiTi on Ru [164].

2.2.4. Effect of Ru and Pt seed layer

Wafer curvature (Figure 18), GIXRD (Figure 19) and electrical transport (Figure 23) measurements clearly indicate that all the NiTi thin films in this section are crystalline, and undergo a B2 to R-phase transformation with a narrow hysteresis. Furthermore, crystalline thin films with narrow hysteresis for a deposition temperature set to 325 °C were able to be achieved. This is much lower than previously observed for sub-micron NiTi thin films grown on Si substrates (T = 425 °C) [53, 54]. For both equiatomic NiTi and Ti-rich NiTi, only amorphous films have been reported in literature for deposition temperatures below 425 °C. Thus, the observed crystalline behavior of our films cannot be explained due to Ti-rich composition alone. Higher surface roughness of Ru seed layer in comparison to Si substrate can potentially explain this behavior, whereby nucleation sites have lower energy barriers.

Additionally, increased roughness due to Ru seed layer would increase nucleation density leading to a decrease in average grain size, which could also explain the lack of B2 to B19' transformation. Previous studies have shown that the growth of B19' phase usually requires grains sizes higher than 100 nm to achieve significant volume fraction near room temperature [81, 98]. For grain sizes smaller than 100 nm, the transformation temperature for B19' phase reduces dramatically and lowers below room temperature. Experimental and theoretical studies have shown that the energy barrier for B19' increases with smaller grain size lowering the M_s temperature [98, 166, 167]. This is consistent with the observation of partial B2 to B19' transformation for Ru600_225 and Ru400_225 with average grain size of 450 nm and 120 nm respectively, and lack thereof for all the other samples with average grain size in the range of 25–70 nm. The lowering of M_s for the R-phase to B19' transformation also agrees with the resistivity measurements below room temperature.

It is worth noting that only 5 nm of Ru was sufficient to achieve crystalline thin films, making Ru a more efficient seed layer in comparison to Pt where studies have shown that up to 20 nm of Pt is required to obtain lower crystallization temperatures [39, 168]. Further studies focusing on direct comparison between Pt and Ru are needed to understand the effects of both the seed layers on NiTi thin film growth.

2.2.5. Effect of deposition temperature (T_D)

Stress-bow measurements in Figure 18 show that the variation in T_D heavily influences the SME. Thin films with higher T_D show larger recovery stress and hysteresis. For example, Ru600_225 shows a recovery stress of 225 MPa and hysteresis of 24 °C, while Ru325_225 shows a recovery stress of 75 MPa and a hysteresis of 4 °C. This behavior can be explained due to differences in phase transformation behavior, i.e. whether the film transforms from B2 ↔ R, B2 ↔ B19', or B2 ↔ R ↔ B19'. As discussed earlier, for Ru600_225, although Bragg peaks due to B19' are not directly observed due to overlap with Ti_2Ni phase, higher recovery stress as well as large variation in ρ, signify a larger structural distortion than what R-phase alone can produce. Therefore, the transformation pathway for Ru600_225 is transition from B2 to R, immediately followed by a partial transition from R to B19' (double peak structure in ρ), resulting in coexistence of B19' and R-phase at room temperature. For films with lower T_D, such as Ru400_225, the transition between B2 ↔ R and R ↔ B19' starts to separate. This can be seen in Figure 18(a), where two step changes are observed for Ru400_225, as well as in Figure 23(b) where ρ steadily increasing upon cooling, indicating possible partial transformation to B19' phase at a later stage. For the lowest T_D, Ru325_225, full suppression of B19' is observed at room temperature. The shift of transformation temperature to lower values for B19' phase is caused by the R-phase stabilization due to higher residual stresses from both the precipitate and the substrate constraints, and has been

observed in literature [161, 165-167]. Thus, thin films grown at higher T_D show higher recovery stress but wider hysteresis due to partial transformation to B19' phase, while films grown at lower T_D show lower recovery stress and narrower hysteresis due to R-phase transformation. The deposition temperature also influences the grain size of both B2 and Ti_2Ni, which in turn affects the transformation pathway for the martensitic phase. During the growth process, as the film is deposited, it is also being annealed *in-situ* at T_D. Due to this effective annealing, the grain size for B2 phase increases with T_D, as shown in Table 2. Grain size of Ti_2Ni precipitates, which typically form along grain boundaries, also increases with longer annealing times and elevated deposition temperatures [169]. Thus, for elevated T_D, coarsening of both B2 and precipitate occurs resulting in a lower density of Ti_2Ni precipitates [170, 171]. As Ti_2Ni tends to hinder the shear deformation of the matrix during martensitic transformation, lower density of precipitates results in a higher possibility of martensitic transformation and thus better shape memory properties pronounced through increased recovery stress. Furthermore, this increases SME directly due to presence of bigger B2 grains with fewer grain boundaries to hinder the shear transformation to B19'. This is consistent with the observation of larger SME effect for thin films deposited at high temperatures, Ru600_225 and Ru400_225.

The transformation to R-phase is not heavily influenced by precipitate size effect. This is due to the fact that when Ti_2Ni precipitates are small, they tend to form Guinier-Preston (GP) zones, thin disc-like structures. These GP zones are coherent or semi-coherent with B2 and R-phase (but not B19'), thus resulting in B2 to R transformation by shear deformations translating through the GP precipitate with little impedance [24, 165, 170].

2.2.6. Effect of Film Thickness

The transformation range for B2 to R phase increases as the film thickness decreases, shown by the resistivity data in Figure 23(c,d) where a decrease in slope of ρ(T) is observed with thickness. This is likely due to reduction in grain size of B2 phase for lower values of thickness as listed in Table 2. For the film with highest thickness, Ru325_450, the average grain size is higher due to longer deposition time during which grain growth can occur. For thinner films, Ru325_225 and Ru325_120, shorter deposition times result in smaller average grain size with a larger amount of grain boundary interfaces. Strain fields associated with grain boundaries can act as an additional energy barrier and hinder the phase transformation [82, 83, 136, 172]. Thus, larger temperature changes are required to further the shear transformation across grain boundaries, widening the temperature range over which the transformation occurs for Ru325_225 and Ru325_120. The larger amount of grain boundaries in these thin films also result in higher energy barrier for dislocation movement preventing fatigue over multiple cycles [173]. Thus, the presence of grain boundaries further stabilizes the B2 ↔ R transformation over multiple thermal cycles.

Film thickness also influences the grain size of Ti_2Ni precipitates. Longer deposition times for films with higher thickness can result in larger grain size for Ti_2Ni [165, 169]. As discussed earlier, smaller Ti_2Ni GP zones are coherent or semi-coherent with B2 and R phase [165, 174], thus only certain preferred orientations are observed in GIXRD spectra for films with lower thickness, Ru325_120 and Ru325_225, in Figure 19(b). For thicker films, as the precipitate size increases, the GP zones start to form into larger Ti_2Ni crystallites which are incoherent with NiTi. Thus, all possible crystallite orientations are observed in GIXRD spectra for Ru325_450. This also explains the wafer-stress measurements in Figure 18(b), as incoherent Ti_2Ni phase diminishes the SME for Ru325_450, in comparison to the coherent GP zones which allows transformation with little impedance. On the other hand, as the strain fields imposed by GP zones is higher, the residual

stress increases, as observed for Ru325_120 and Ru325_225 films. In comparison, for Ru325_450, the residual stress is lowest due to more granular Ti_2Ni precipitates producing lower strain fields [24].

2.2.7. Summary

The phase transformation in NiTi films deposited on a Ru seed layer was investigated as a function of deposition temperature and film thickness. Stress-bow, GIXRD, and resistivity measurements revealed the B2 to R-phase transition in all the films and indicated towards phase coexistence of R-phase and B19' for films with higher deposition temperature. By utilizing Ru as a seed layer, lower deposition temperatures (325 °C) and sub-micron thin films (120 nm) with the desired SME were able to be achieved. It was also shown that the small grain size and high residual stress in films with lower deposition temperatures stabilizes B2 to R transformation, and lowers the transformation temperature to B19' phase. This work shows that using thin Ru seed layer provides a unique way to achieve lower deposition temperatures than previously achieved for sub-micron thin films.

These results helped enable the application of NiTi films in MEMS devices with wider selection of viable substrate materials including flexible materials such as polymers. The following section details shape memory response in nanoscale thickness SMA films deposited directly onto polyimide at lower processing temperatures.

2.3. Co-sputtering of NiTi and Ti target onto polyimide (PI)

In this section, NiTi is sputtered onto polyimide (PI) films and shape memory effects were verified using nanoindentation, atomic force microscopy (AFM), and XRD methods. *Table 4* lists the deposition parameters used for the NiTi co-sputter directly onto PI films.

Table 4. Deposition parameters for NiTi on polyimide (PI) study.

Sample ID	T_{Dep} (°C)	t (nm)	Comp. Ti/Ni (at.%)
PI_550_400	550	400	52/48
PI_450_400	450	400	52/48
PI_400_400	400	400	52/48

2.3.1. Nanoindentation

In this section NiTi deposition onto soft polymer substrates like polyimide (PI) through a nanoindentation method is investigated. SMA MEMS actuators offer many advantages in terms of low voltage requirements, high work density, and relatively low processing complexity. The majority of SMA films characterization and processing efforts to date have utilized rigid, crystalline materials, such as Si (100) wafers, as both the film deposition substrate and the SMA device release layer. More recently, researchers have demonstrated the deposition of crystalline SMA films on polymer substrates, which opens the application space to soft-bodied robotics, biomechanical systems, and other flexible actuation schemes [13, 49]. However, the SME in NiTi systems typically requires high temperature processing steps, which presents thermal limitations on all prior materials in the fabrication process. The SME is limited by the thermally dependent interdiffusion of NiTi and substrate material, as well as surface oxidation effects. These issues are particularly limiting for submicron films, which have high surface to volume ratios relative to bulk SMA materials. In order to ensure shape memory effects in nanoscale SMA films, these surface oxide and thermal diffusion layers between SMA and substrate will need to be minimized.

Nanoindentation is a common technique for examining the mechanical properties of small volumes of material [175]. Indentation of shape memory films has previously been demonstrated [176-178]. During an indentation test, the load *P* and displacement *h* are monitored on the nN and

nm scales, respectively. A calibrated tip area as a function of contact depth *A(h)* can be used to measure the hardness, *H* according to:

$$H = \frac{P_{max}}{A}$$

A is determined from the contact depth h_c:

$$h_c = h_{max} - \varepsilon \cdot \frac{P_{max}}{S}$$

which accounts for the material deformation that does not result in direct contact with the probe. **ε** is a tip geometric constant roughly equal to 0.75 for a Berkovich tip [175]. The stiffness of the tip/sample contact *S* is defined as the slope of the unloading curve at h_{max}:

$$S = \frac{dP}{dh}$$

The stiffness of the tip/sample contact can be used to determine a reduced elastic modulus through,

$$E_r = \frac{S}{2\beta} \cdot \sqrt{\frac{\pi}{A(h_c)}}$$

Where β is a geometric constant roughly equal to 1 for a Berkovich tip. The sample indentation modulus can then be found through the following relationship that accounts for deformation in the tip and sample during contact:

$$\frac{1}{E_r} = \frac{1 - \nu_i^2}{E_i} + \frac{1 - \nu_s^2}{E_s}$$

Here, E_s, E_i, n_s, and n_i and are the elastic modulus and Poisson's ratio, of the sample and probe, respectively.

In this work, NiTi films were sputtered onto polyimide (PI) films on Si at elevated substrate temperatures for *in-situ* crystallization. These PI films can serve as flexible substrates or device release layers in subsequent MEMS device processing. XRD scans performed at room temperature

showed the presence of martensite and austenite phases in these films in the as-deposited condition, indicative of crystallization and potential for SME. Nanoindentation was used to 1) study the local mechanical properties of the NiTi films deposited at various temperatures, and 2) induce local deformation at various depths relative to the films surfaces. Atomic force microscopy (AFM) studies with *in-situ* heating revealed partial thermally-activated recovery of the nanoindent arrays futher verifying the SME. These results indicate that future NiTi devices fabricated on polyimide films can retain the SME and potentially be used in a variety of applications requiring low-temperature processing and thermal actuation.

2.3.2. Sample Preparation for Nanoindentation Experiments

NiTi films were co-sputter deposited onto PI coated Si substrates for *in-situ* crystallization at substrate temperatures of 400 °C, 450 °C, and 550 °C, also summarized in Table 4. Each NiTi film had a thickness of 400 nm. The deposition conditions in terms of target power and deposition rate are detailed in previous reports on NiTi film characterization and device fabrication on Si wafers [113, 179, 180]. The sputter chamber pressure in the AJA co-sputter tool was maintained at 5mTorr, the film deposition rate was 15 nm/min, and the DC power supplied to the NiTi and Ti targets was 375 W and 200 W, respectively. Substrate rotation was maintained at 20 rpm for achieving maximum uniformity across the wafer surface.

Nanoindentation experiments were performed with a Hysitron 950 Triboindenter with a diamond Berkovich tip. Measurements were performed in load control mode at room temperature. Forces ranges from 100-2500 μN were applied within an array of indents spaced approximately 5 μm apart.

AFM measurements were performed using an Asylum MFP-3D system. The AFM probes used in this study were Veeco Si probes with nominal natural frequency, stiffness, and radius of curvature, of 350 kHz, 40 N/m, and 10 nm, respectively. A heating stage was used for scans with *in situ* temperature control. The temperature was raised at a rate of 120 °C/min; once the desired temperature was reached, the films were allowed to equilibrate for 5-10 min before subsequent AFM scans.

XRD was performed on a Rigaku MiniFlex600 benchtop model tool from 35 - 75° using the theta/2theta collection method. The data collection step size was 0.15 with a step dwell time of 0.5 seconds. Peak location indexing was performed with respect to the main Si (100) peak at 70°.

2.3.3. Characterization by Nanoindentation, AFM, and XRD

Room temperature indentation results on the NiTi films on polyimide substrates are summarized in Figure 24. The indentation elastic modulus and hardness are plotted as a function of contact depth for the various films tested in this study. Note that tests were performed in load control, from 100 - 2,500 μN. The hardness of the 400 °C specimen was more scattered than the 450 °C and 550 °C deposited films, which is likely the result of uneven and uncompleted crystallization at lower processing temperatures. The film deposited at 400 °C showed the elastically stiffest response, in particular for contact depths less than 50 nm. This is likely due to a lower presence of the martensite phase and possibly a partially amorphous phase at the surface. In contrast, the indentation response for the 450 °C and 550 °C films were more compliant and more uniform, with an indentation modulus of 20 - 30 GPa. This result is in agreement with previous mechanical testing on NiTi SMAs that found the elastic modulus of the austenite phase was roughly 2 - 3 times stiffer than the martensite phase [181]. Previous indentation work on NiTi in the martensite phase has shown that material deforms through the following mechanisms: (1)

material immediately under the tip deforms plastically due to the relatively high stresses that exceed the yield stress, (2) material immediately outside the plastic zone deforms through martensitic rearrangement; material in this zone may be recovered through subsequent heating, and (3) material outside the martensitic rearrangement zone, furthest from the tip during indentation, deforms elastically due to the relatively low stresses [182]. Therefore, with the sharp indentation probe used in this study, a Berkovich probe with an approximately 150 nm radius of curvature, a shape memory effect with less than 100% recovery would be expected.

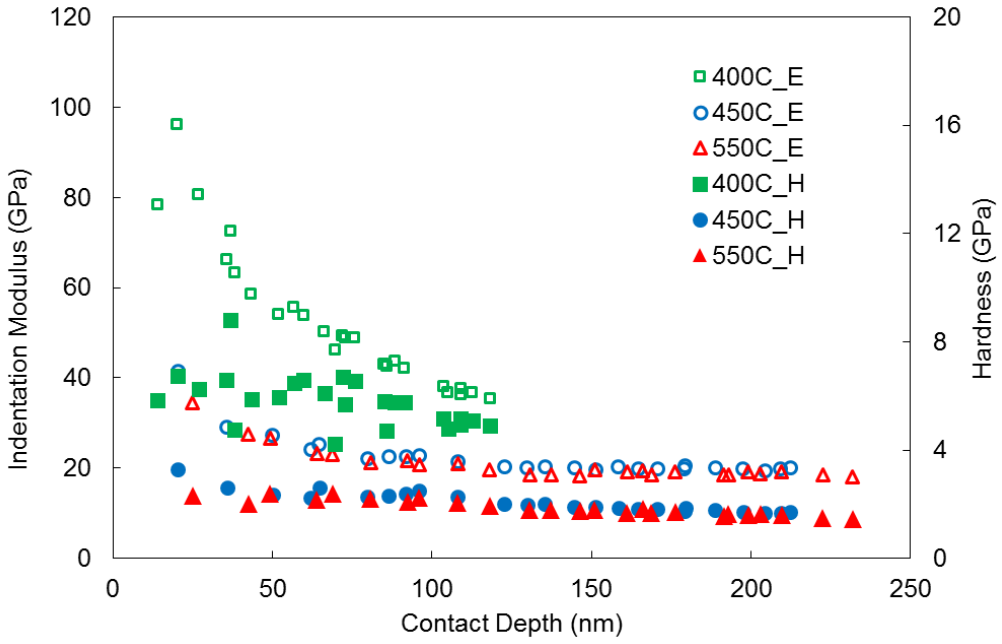

Figure 24. Local mechanical behavior of NiTi films deposited on polyimide substrates at different temperatures as found through nanoindentation at room temperature.

Figure 25 shows an AFM height image of the residual indent in the center of the array placed within the 550 °C film. The corresponding AFM phase image is shown in Figure 26. Apparent grains of 50 - 100 nm can be seen in the images. Considering that measurements at h_c

are elastically influenced by material at a depth of up to $10h_c$, the indentation modulus of the films probed several grains up to several tens of grains depending on the contact depth.

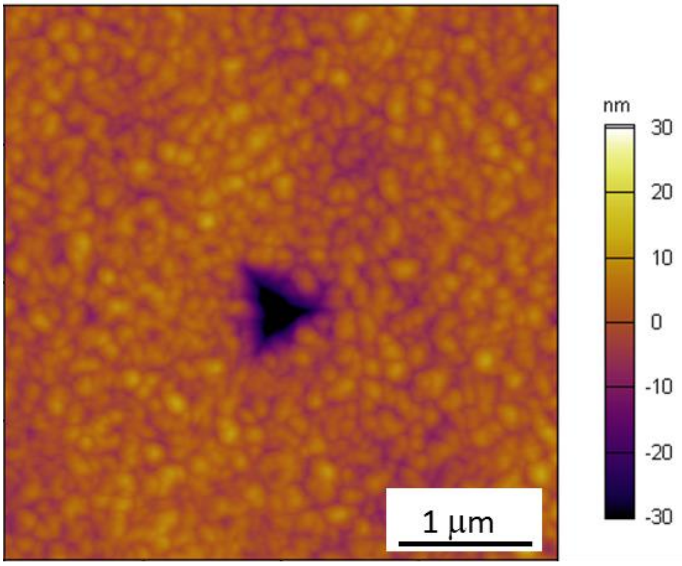

Figure 25. Room temperature AFM height image of residual indent in NiTi film deposited at 550 °C.

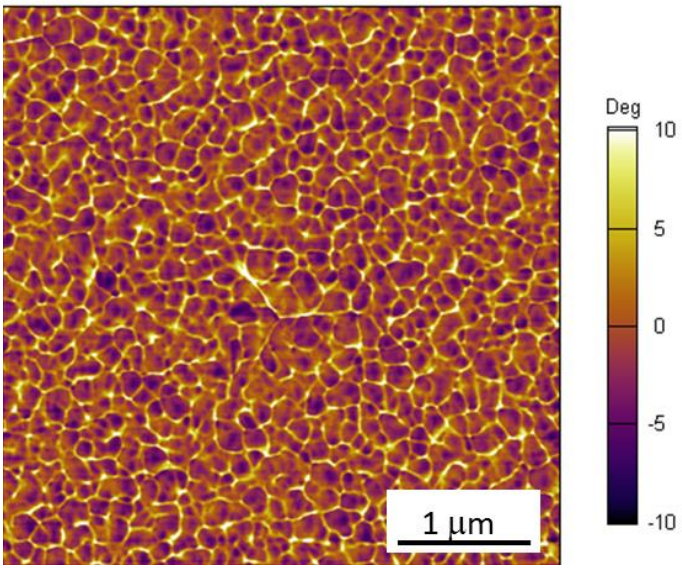

Figure 26. Room temperature AFM phase image of residual indent in NiTi film deposited at 550 °C.

Figure 27 displays AFM height maps with *in-situ* heating in order to characterize the nanoscale recovery of the indents within the film deposited at 550 °C. Room temperature scans of the array revealed the indents of various depths. Sink-in deformation immediately outside many of the indents was also apparent, potentially due to tests of a stiff film on a relatively compliant substrate. AFM scans of the array at 60 °C, 80 °C, and 100 °C are also shown. At 60 °C, partial recovery of the indents could be seen; at 80 °C a relatively large amount of recovery was observed for the majority of the indents; by 100 °C, additional recovery could be seen but the effect was limited. Note that the scratch and pile-up of material seen near the central indent in the 60 °C, and then also in the 80 °C, and 100 °C scans, was due to the thermal expansion of the film for the initial temperature application; the film made contact and then drifted with the probe while the tip was disengaged from the sample. Subsequent scans on the film displayed no loss in resolution or other imaging artifacts indicating that the probe was not damaged during this incidental contact; further heating periods were performed with the probe disengaged at a safe distance from the films.

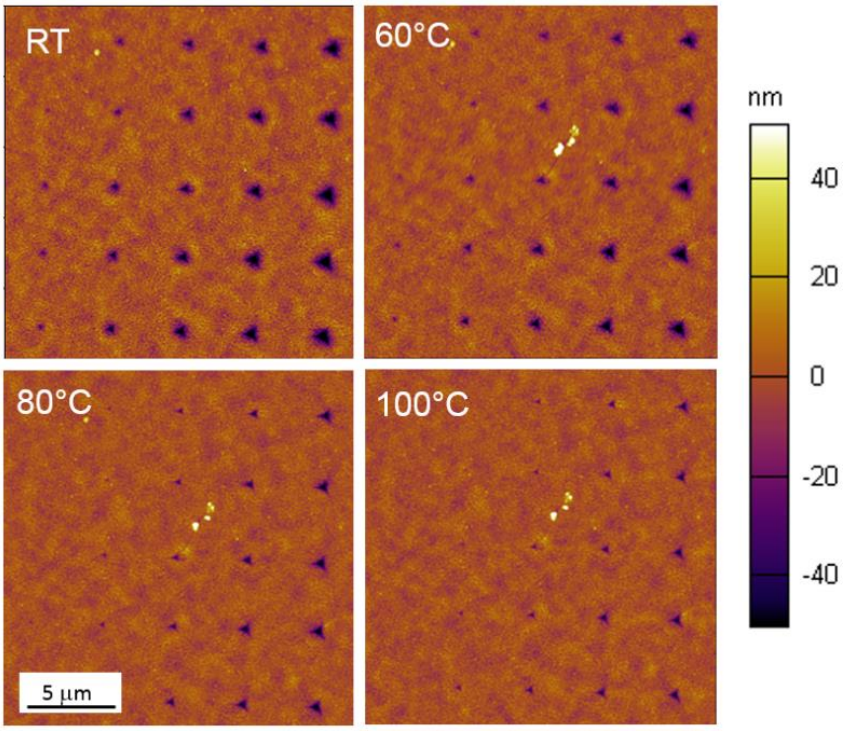

Figure 27. AFM scans on the NiTi film deposited at 550°C. From top left, the indent array on the film surface at room temperature (RT), 60°C, 80°C, and 100°C.

Figure 28 displays AFM height profiles of an indent in the NiTi film deposited at 550 °C. At room temperature, the indent was approximately 75 nm deep, as measured vertically from the deepest position of the indent to the averaged film surface position (height = 0 nm), along a lateral line through one axis of the Berkovich probe (see inset). Recovery at a given temperature *R(T)* can be defined as:

$$R(T) = \frac{h_i - h_T}{h_i} \cdot 100\%$$

where h_i is the indent depth at room temperature and h_T is the indent depth at temperature T. At 60 °C, 80 °C, and 100 °C, the recovery was estimated at 31%, 40%, and 66%, respectively. In comparison, the film deposited at 450 °C had an estimated recovery of 31%, 39%, and 66%, for the same temperature intervals. This indicates that the crystallization of the films was largely

completed at the deposition temperature of 450 °C. In contrast, the film deposited at 400 °C had an estimated recovery of 4%, 28%, and 22% for the same temperature intervals, indicating that this deposition condition was insufficient for the complete crystallization process. The cause of the decrease in recovery from 80 °C to 100 °C for the film deposited at 400 °C is unknown but is likely due to the variability associated with the measurement; more testing is required on indents of similar depth in order to establish an average response. The XRD results indicate that all films were crystallized in their as-deposited condition, and that the larger volume fraction of martensite in the 450 °C, and 550 °C films is the reason for larger extent of nanoindentation recovery. While the results are drawn from a small sample size, they appear to demonstrate that the films are crystallized on the polyimide substrates at 400 °C, with larger volume fractions of thermally transformable martensite present at the higher deposition temperatures.

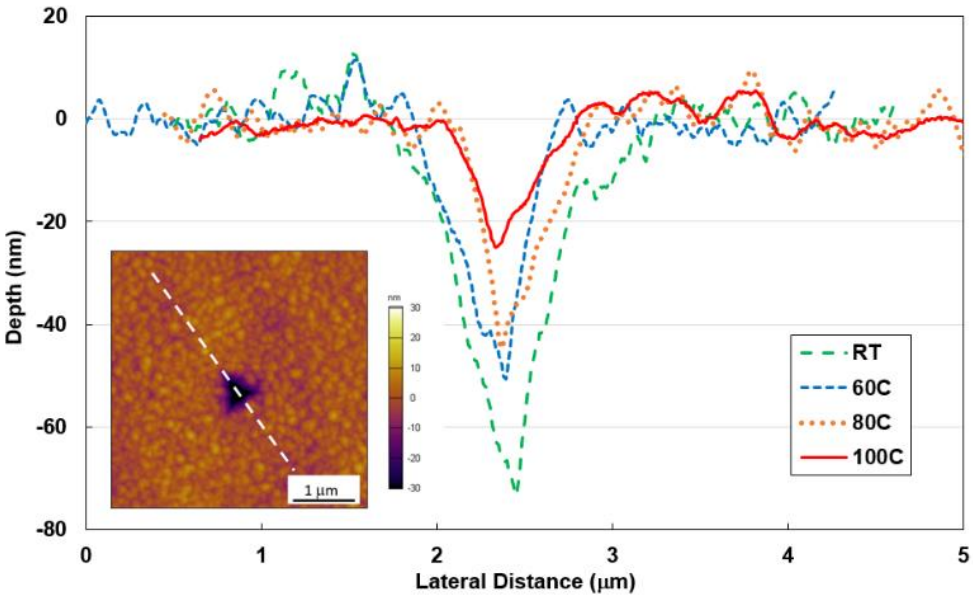

Figure 28. Height profile of center indent in array at various temperatures for the NiTi film deposited onto PI at 550°C.

Figure 29 - Figure 31 show the XRD results for the 400 °C, 450 °C, and 550 °C NiTi films deposited on polyimide. In Figure 29, the 400 °C film is crystallized in the as-deposited condition

as indicated by the sharp B2 austenite phase peak. Small amounts of the martensite phase are indicated in the figure as well. This relatively small amount of martensite phase is responsible for the indentation recovery reported. In Figure 30, the B2 austenite phase is accompanied by larger and more pronounced martensite peaks, indicative of larger volume fractions of the thermally transformable martensite phase present at room temperature in the 450 °C film. This is consistent with the relatively large amounts of indent recovery reported. In Figure 31, the martensite peaks for the 550 °C film also indicate a larger volume fraction, consistent with the recovery data reported.

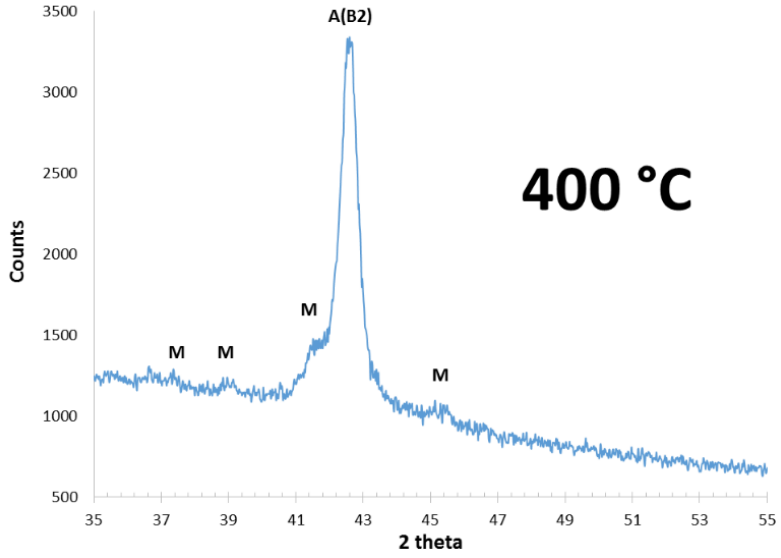

Figure 29. XRD profile for NiTi film deposited at 400 °C onto polyimide

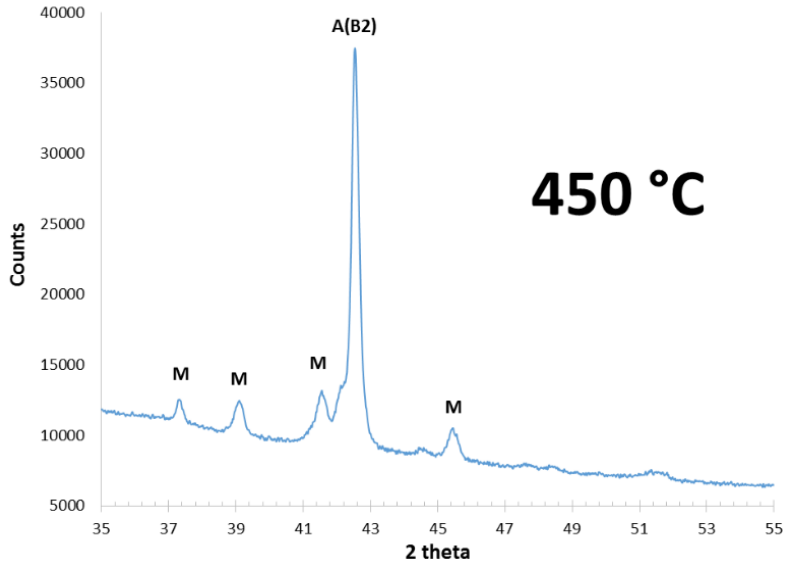

Figure 30. XRD profile for NiTi film deposited at 450 °C onto polyimide

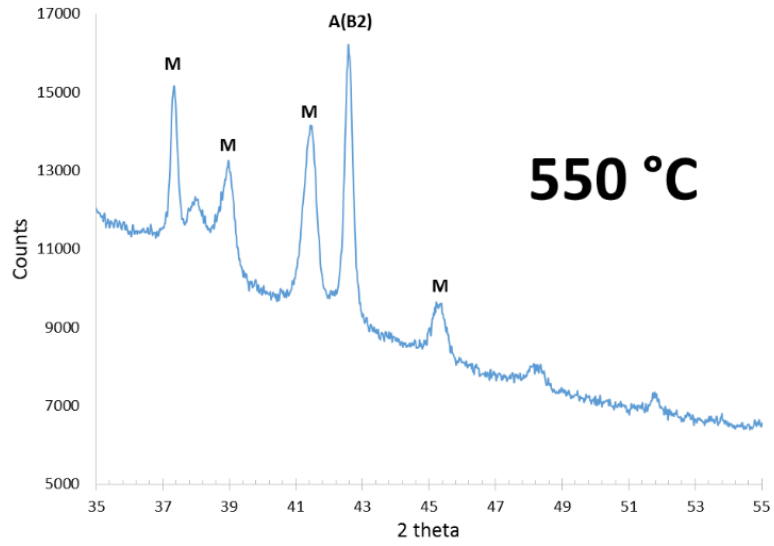

Figure 31. XRD profile for NiTi film deposited at 550 °C onto polyimide

2.3.4. Summary of Nanoindentation Experiments

Equiatomic NiTi films of 400 nm thickness were co-sputtered onto 1.5 µm thick polyimide films on Si wafer at several different processing temperatures (400 °C, 450 °C, and 550 °C). The

films were all confirmed to be crystallized in the as-deposited condition using XRD. The 400 °C NiTi film showed a sharp B2 austenite peak, accompanied by very little presence of martensite phase at room temperature. The 450 °C and 550 °C NiTi samples both showed significant volume fractions of the martensite phase at room temperature, which helps explain larger thermal recovery as shown in nanoindentation. Nanoindentation was used to probe the mechanical properties of the NiTi films deposited onto the polyimide substrates. The indent recovery was characterized through atomic force microscopy with *in situ* heating. Indentation recovery of the films annealed at 450 °C and 550 °C was observed up to approximately 66% of initial deformation, which is likely limited by a plastic deformation zone immediately under the sharp probe. The results are promising for enabling SMA actuator devices processed on polyimide films which could serve as structural release layers or flexible substrates.

In the following chapter, it is demonstrated how some of the previous developments and characterizations allowed established NiTi deposition recipes to be extend towards deposition, crystallization, and characterization of shape memory effects in freestanding SMA bilayer films. Finally, the freestanding SMA MEMS bilayer actuators are shown to actuate at fast rates by irradiating with lower power green laser.

Chapter 3: Fabrication and Laser-Irradiation of SMA MEMS Bilayer Actuators

Chapter 2 highlighted the fabrication and characterization of nanoscale thickness NiTi films exhibiting SME. Those compositions lay the ground work for additional MEMS fabrication resulting in SMA MEMS actuators. This chapter describes the processes used to fabricate, characterize, and test NiTi SMA MEMS actuators resulting in the actuation of NiTi SMA using low-power laser-irradiation. The relationships between curvature radius, recovery stress, and degree of unfolding are elucidated by measuring the bending of SMA MEMS bilayer through the thermally actuated deflections. The following methods were implemented for the experimental characterization of sputtered NiTi films: stress versus temperature for NiTi on 4-inch Si wafer, GIXRD including SSRL beamline, Differential Scanning Calorimetry (DSC), and EDAX (chemical composition analysis).

3.1. Sample Preparation

NiTi films were co-sputtered using an AJA ATC 2200 co-sputter tool, with independent DC power supplies to two different 4-inch targets. The targets used were a 99.995% purity $Ni_{50}Ti_{50}$ target and a pure Ti target. The nominal process involved 375 W supplied to the NiTi target and 250 W supplied to the Ti target. Substrate rotation helped obtain optimal uniformity for a nominal deposition rate of 15 nm/min. Depositions were carried out under an argon (Ar) atmosphere at either 2, 5 or 10 mTorr. Over the course of hundreds of NiTi film depositions and subsequent wafer bow vs. temperature measurements, “best practices” were identified for producing thin films of NiTi that exhibited large amounts of recovery stress. Initially, NiTi was co-sputtered at room temperature onto Si and then post-sputter annealed at 600 °C for one hour in vacuum. NiTi was

also sputtered onto AZ 9245 photoresist, lifted off, and *in-situ* annealed at 600 °C for 10 minutes in the DSC followed by 3 °C/min heating and cooling characterizations. Additionally, NiTi was co-sputtered onto thin Pt seed layers on Si and bare Si using a 600 °C substrate temperature, resulting in crystallized films as-sputtered. This was confirmed with XRD measurements and post-sputter stress vs. temperature curves.

Several material characterization methods were carried out as in other studies. Energy dispersive x-ray spectroscopy (EDS) was used to determine film composition analysis using a Hitachi S-4500 scanning electron microscope (SEM) equipped with a PRISM60 Princeton Gamma Tech detector, using a beam acceleration voltage of 20 kV. XRD was performed using a Rigaku XRD tool on control samples of Pt on Si in as-evaporated conditions, as well as in 600 °C vacuum annealed conditions. XRD was also performed on the following bimorph material stacks: NiTi on Si and NiTi on Pt on Si.

DSC was performed on a Perkin Elmer machine using a heating/cooling rate of 40 °C/min for an *in-situ* anneal scan up to 600 °C, and a rate of 3 °C/min to characterize phase transformation temperatures in the SMA films for scans between ambient and 100 °C. For DSC sample preparation in particular, films were sputtered onto a sacrificial photoresist layer using an unheated deposition, released in acetone, and then rinsed with deionized water (DI), and dried before loading into DSC sample pans. The mass of each sample was recorded before and after the DSC run to verify adequate drying prior to the 600 °C anneal.

Additionally, NiTi material for DSC experiments were prepared in a manner that more closely matched the eventual device fabrication. First, the alloy was co-sputtered onto Si using a 600 °C substrate temperature and then patterned with an array of 100 µm diameter windows to the substrate spaced every 300 µm. The film was dry released using a XeF_2 etch. The resulting NiTi

flakes were collected and loaded into the DSC and XRD tool for analysis.

Stress versus temperature measurements were performed using a Toho FLX-2320-S wafer bow tool with controlled heating and cooling from 25 °C to 100 °C with a heating and cooling rate of 1 °C/min. For these experiments, films of NiTi were prepared by sputtering onto 4-inch Si wafers and vacuum annealing at 600 °C, 500 °C, and 450 °C to crystallize the material. Additionally, several NiTi films on Si wafers where the NiTi was sputtered under 600 °C substrate conditions were measured. In later efforts, these films with NiTi *in-situ* anneals of 325 °C, 350 °C, 375 °C, 400 °C, 425 °C, and 500 °C were characterized. Wafer bow was measured experimentally from 25 °C to 100 °C at a 1 °C/min heating and cooling rates, which allowed the calculation and plotting of the temperature-dependent residual stress in the NiTi film for each wafer sample based on Stoney's equation (1).

$$\sigma = \frac{E}{6(1-\nu)} \frac{{h_s}^2}{h} \left(\frac{1}{R} - \frac{1}{R_o}\right) \qquad \text{(eq. 1)}$$

Here, σ is the stress in the thin film, and E, ν, and h_s are Young's modulus of Si, Poisson ratio of the Si substrate and the thickness of the Si substrate, respectively. h represents the NiTi thin film thickness and R and R_o represent the radii of curvature of the NiTi film- Si substrate composite and the curvature of the bare Si substrate. An extended version of Stoney's equation (2) was used in order to calculate the stress in the NiTi layer when deposited on a thin Pt film on Si wafer. Here, σ_{NiTi} is the stress in the NiTi layer, and σ_{Pt} represents the stress in the annealed Pt layer. The variable h_{NiTi} represents the NiTi thin film thickness, and R and R_o represent the radii of curvature of the NiTi film and the annealed Pt/Si substrate, respectively.

$$\sigma_{NiTi} = \frac{E\,{h_s}^2}{6(1-\nu)h_{NiTi}} \left(\frac{1}{R} - \frac{1}{R_o}\right) - \left(\frac{6(1-\nu)}{E}\right) \left(\frac{\sigma_{Pt}(h_{NiTi+Pt} - h_{NiTi})}{{h_s}^2}\right) \qquad \text{(eq. 2)}$$

3.2. Device Fabrication Process

The device fabrication process and thermal operation is shown schematically in Figure 32. Starting with a 4-inch DSP Si wafer, 170-nm Pt was evaporated onto the wafer backside to protect Si from etching during the final device release step with XeF_2. Lift-off patterning of a Pt layer ranging between 20 nm and 200 nm in thickness, using a 10-nm Cr adhesion layer was performed, followed by a blanket sputtering of equiatomic NiTi at 600 °C, using the sputtering process parameters outlined previously [168, 183]. This process yielded crystallized NiTi as confirmed with XRD measurements. The Pt bimorph layer was selected to 1) withstand the 600 °C anneal required to crystallize NiTi, while other metals such as gold (Au) could not survive the necessary anneal temperatures and 2) to impart residual stress to bend the actuator in martensite phase post-release. In order to pattern the NiTi devices, a positive tone resist (Shipley 9245) was lithographically patterned as shown in Figure 32A. Cantilever devices were then wet-etched using a 1:1:10 solution of hydrofluoric acid (HF), nitric acid, and DI water as shown in Figure 32B. A combination of PRS 3000 and O_2 plasma ash was used to strip the resist after the patterning step.

After the blanket deposition of functional NiTi/Pt bimorph layers, rigid Au frames were optionally electroplated into lithographically patterned regions as shown in Figure 32C to confine cantilever bending to one direction. Later device iterations where cantilever length was intentionally limited to 20 μm or narrower, allowed for the Au electroplate step to be skipped, as the device length was much greater than device width, and bending was naturally confined to one dimension. As a final device release step, an AZ 5214 resist layer was patterned and developed to protect the Si front side during a xenon difluoride (XeF_2) dry-etch release, and to confine etching to exposed Si in the immediate vicinity of the devices as shown in Figure 32D. After release, when device temperature reached 70 °C, the devices actuated towards a flatter position as sown in Figure

32E. Released devices were inspected in a scanning electron microscope (SEM) and then subjected to thermal-actuation testing and characterization.

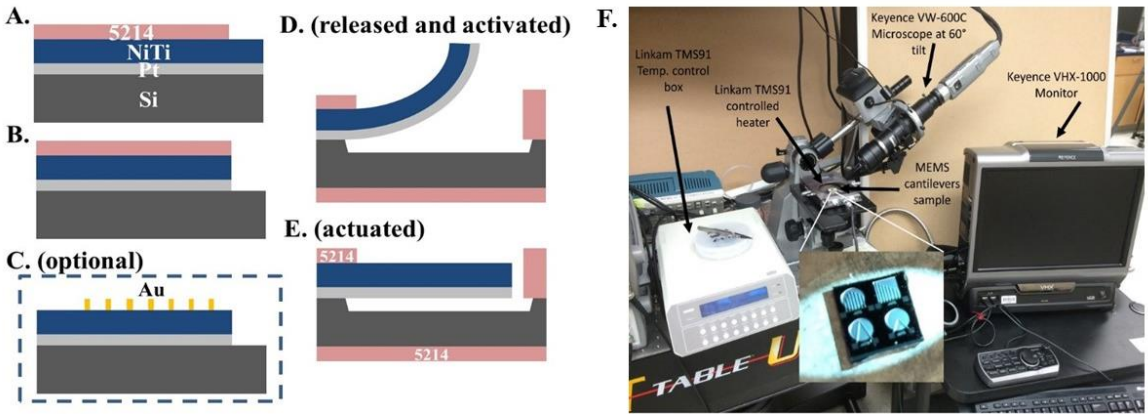

Figure 32 Process flow for NiTi on Pt MEMS SMA actuators with dry release and experimental setup for actuation tests.

3.3. Device Testing and Characterization Process

To characterize the temperature-dependent equilibrium curvature of the NiTi on Pt MEMS cantilevers, a diced 7 mm x 7 mm substrate was positioned on a 1 inch hotplate connected to and controlled by a Linkam TMS91 temperature control box. For this experiment, the sample chip was gradually heated and cooled at 3 °C/min, to match the rate of the wafer bow measurements taken for the stress versus temperature data. A Keyence VHX-1000 digital microscope equipped with the VW-600C camera was used. This microscope has a working distance between the objective lens and the focal plane, and can tilt to obtain a side view of an actuating cantilever as depicted in Figure 32F.

A 400 mW, 532 nm green laser exiting a 400 µm diameter optical fiber was used to irradiate and heat released cantilevers with a known optical intensity level. Optical density filters (ThorLabs) were used to control the laser irradiance levels. The distance from the optical fiber exit

and therefore laser spot size were fixed at 1 mm, which allowed calculation of the optical intensity. A Photron Fastcam camera connected to a microscope to record video at 2,000 frames per second (fps) or more was then used to measure temporal data on activation time.

3.4. Results and Discussion

3.4.1. Transformation Response

An equiatomic composition was achieved as determined by EDX measurements, which yielded Ni:Ti atomic ratios of near-equiatomic composition. Table 5 lists the various process combinations of different NiTi and Ti target powers to arrive at suitable settings to yield equiatomic NiTi. Deviation from equiatomic favored slightly Ti-rich compositions no more than 53 at.% Ti. Film thickness measurements at multiple locations in addition to post-sputter resistivity measurements indicated that film uniformity was greater than 92%, across a 4-inch wafer. This was based on 25 measured resistivity values in a circular pattern starting at wafer center and propagating outwards where the final circular ring of measurements were near the wafer diameter on a single NiTi deposited wafer. Resistivity measurements across multiple deposition runs varied less than 5% for the nominal NiTi co-sputtering process.

Table 5 EDX measurements for equiatomic NiTi co-sputter recipe development.

	Target Power (W)			
Process	**NiTi**	**Ti**	**Dep. Rate (nm/min)**	**Composition**
1	375	30	12.5	$Ti_{40}Ni_{60}$
2	375	60	12.5	$Ti_{42}Ni_{58}$
3	375	150	13.5	$Ti_{45}Ni_{55}$
4	375	250	15.0	$Ti_{50}Ni_{50}$
5	300	375	15.0	$Ti_{57}Ni_{43}$

Differential Scanning Calorimetry (DSC) is widely used in SMA studies to determine phase transformation temperatures for crystallized samples of thin-film material. The reversible SME is clearly demonstrated when an endothermic reaction takes place upon heating (martensite to austenite transformation), followed by the reverse (austenite to martensite) exothermic reaction upon cooling from high temperature. A series of DSC scans were performed and determined that the crystallization temperature for each alloy, as indicated by a large exothermic reaction, which for the equiatomic alloy peaked at 468 °C and completed by 600 °C as shown in Figure 33A.

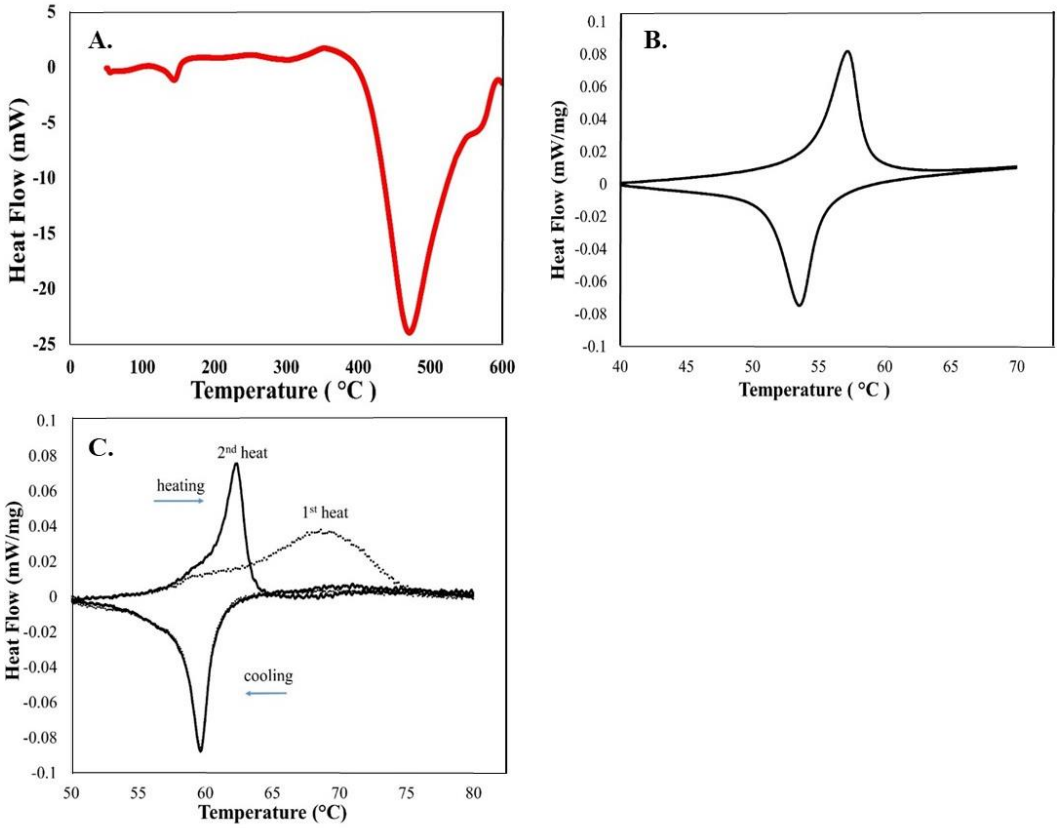

Figure 33 DSC curve for a) amorphous co-sputtered NiTi in DSC crystallization scan, b) 2 µm $Ni_{50}Ti_{50}$ annealed to 600 °C in the DSC, c) NiTi flakes after patterned and dry-released from Si substrate

To test for a shape memory effect, a 3 °C/min scan from RT to 100 °C after the sample had been annealed at 600 °C for 10 minutes in the DSC tool was performed. Each sample mass was at least 5 mg, with up to 16 mg tested. Figure 33B shows a DSC heating and cooling scan for equiatomic $Ni_{50}Ti_{50}$ immediately following the 600 °C anneal in DSC tool under flowing N_2. Other Ni-rich samples did not exhibit a SME above ambient temperatures, which is generally expected for off-equiatomic NiTi, especially in Ni-rich cases, where phase change has been reported as low as -100 °C. Only the equiatomic NiTi and Ti-rich sample recipes exhibited a SME when characterized using DSC. The heating scan at 3 °C/min shows the martensite to austenite phase transformation completed at 58 °C. The cooling scan shows the reverse austenite to martensite

peak transformation completed at 50 °C, indicating that the lifted off, and thus stress free NiTi, has very narrow temperature hysteresis.

The DSC data in Figure 33C for a 1.6 μm NiTi film, sputtered onto Si at 600 °C, and wet-etch patterned and dry released via the XeF_2 dry etch, exhibits the interesting effect that the full SME was only apparent after an initial heating and cooling cycle. This effect was unique to released structures of NiTi on Si, which showed an initial broadened exothermic reaction from the temperature range of about 55-75 °C, indicating that the NiTi seemed only partially crystallized during this initial heating to 100 °C . The strong endotherm upon cooling seemed to indicate more complete crystallization, allowing a more complete phase change to occur. Subsequent heating and cooling, starting with the second cycle shown in Figure 33C shows a more typical reversible nature with a phase change centered about 61 °C, similar to the sample in Figure 33B where NiTi was released from photoresist.

3.4.2. Transformation Microstructure

In order to better understand the effects of Pt-property changes due to the high temperature processing of NiTi, we generated control samples of evaporated Pt on Si wafer. B shows the thermal stress scan on 200 nm Pt on Si wafer. Residual stress is low, on the order of about 140 MPa tensile. Figure A shows the XRD profile for this film. The Pt (111) peak is pronounced in the as deposited condition. Annealing this Pt film on Si wafer to simulate what would happen during high temperature NiTi processing revealed several significant effects in the Pt layer. 1) Platinum silicides are formed as evident in Figure B. The Pt (111) peak is completely gone, and various Pt-Si peaks are all that remain. Figure A shows that these newly-formed Pt-Si phases have very high tensile residual stress, on the order of 2.2 GPa. A highly tensile stress region directly below the NiTi would also be expected to cause an initial downward curvature of NiTi/Pt bilayer.

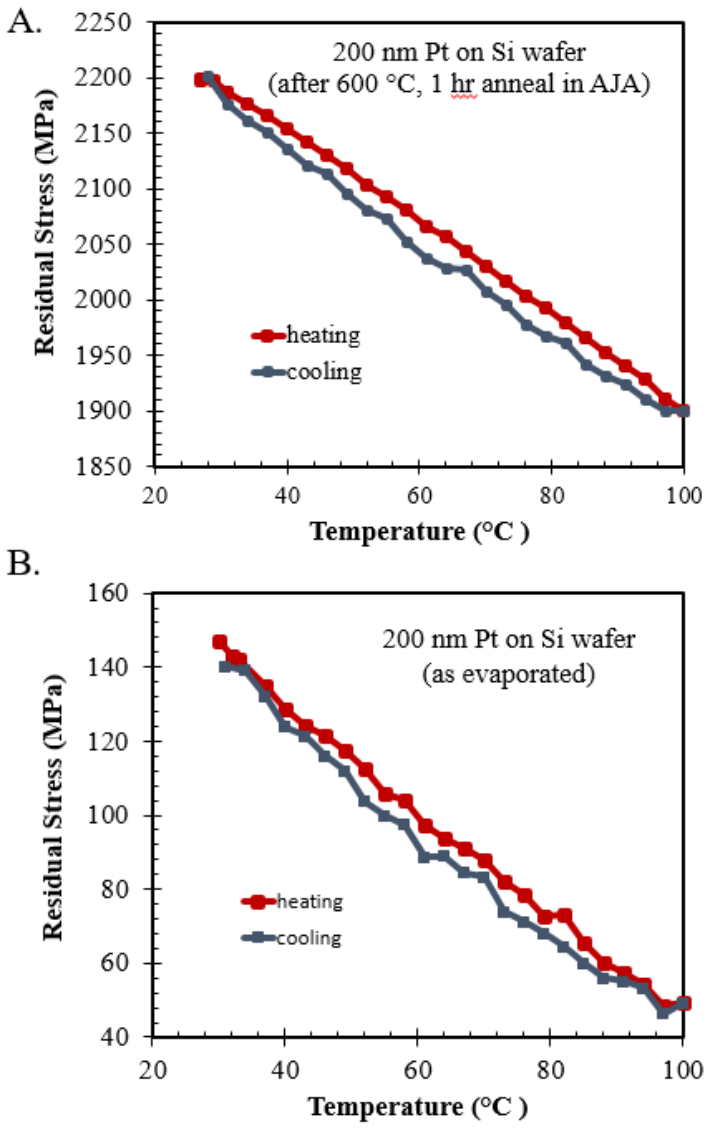

Figure 34 Residual stress as a function of temperature for (a) 200 nm Pt on Si (100) wafer starting with 150 MPa tensile stress, (b) same stress scan on 200 nm Pt on Si (100) annealed in vacuum for 1 hour at 600°C, whereby Pt interdiffuses with Si and gets converted into platinum-silicide. We confirmed Pt-Si peaks using XRD measurements.

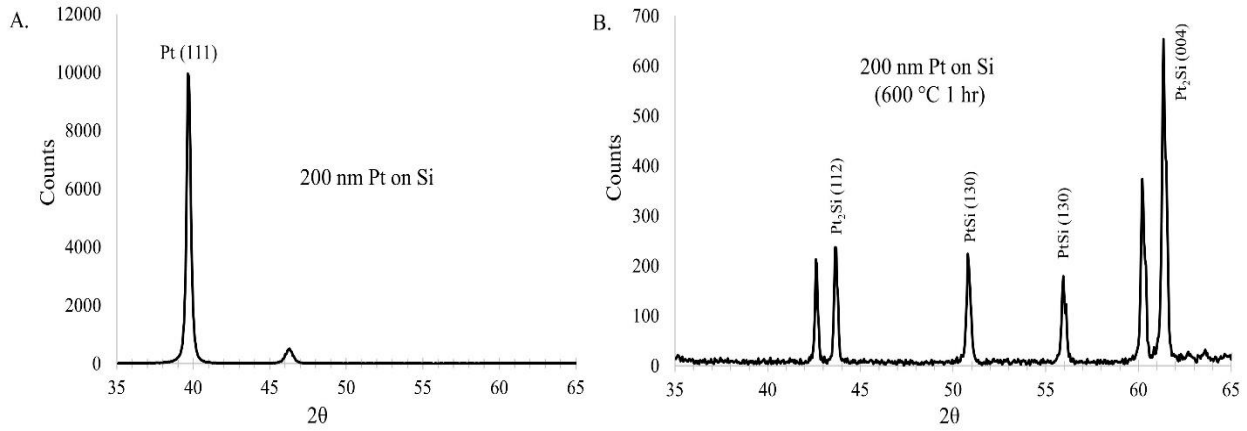

Figure 35 XRD scan for A) 200 nm thick, e-beam evaporated, (111)-oriented Pt on Si (100) and B) same 200 nm Pt film on Si (100) after vacuum anneal, 1 hour, 600°C, whereby Pt mixes with Si to form various platinum silicide compounds that result in order of magnitude increase in film tensile stress; 2.2 GPa as measured with wafer bow tool.

XRD was also used to further study the crystallography of the in-situ annealed NiTi on Si, and NiTi on Pt seed layer. Figure shows various martensite peaks for 981 nm thick NiTi on 200 nm Pt on Si (100), all of which are capable of thermally transforming into the austenite phase upon heating.

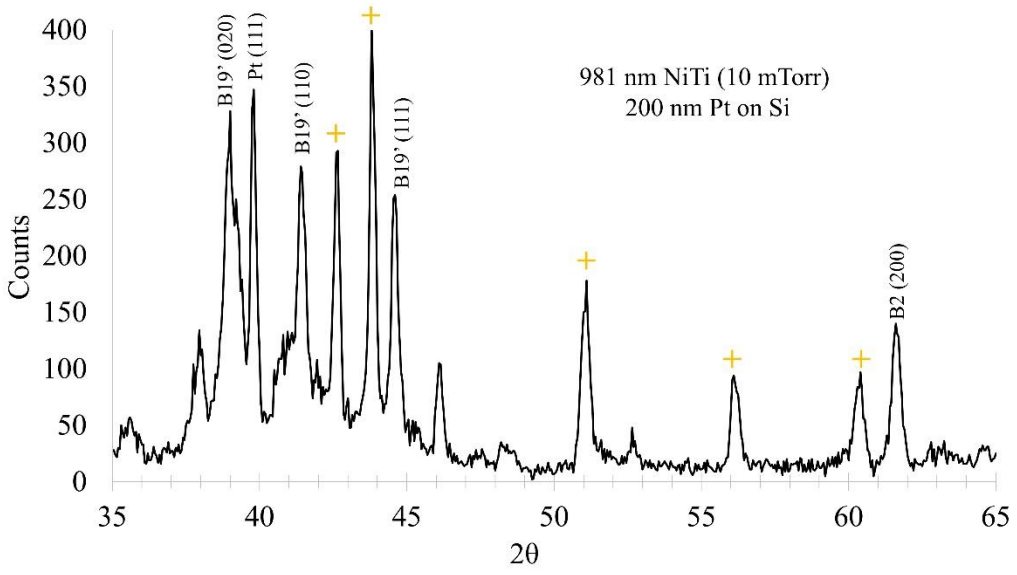

Figure 36 RT XRD scan: ~1 µm thick NiTi on 200 nm Pt on Si (100). Various Martensite peaks (B19') are measured in addition to Platinum Silicide peaks (yellow +).

In Figure 37 the XRD curves for NiTi films of 269 nm and 1.6 µm thickness are compared. Both films were sputtered onto Si wafer at 600 °C deposition conditions. The 1.6 µm NiTi wafer appears to have more significant volume fraction of martensite phase compared to the 269 nm thick NiTi. In fact, no austenite peak is measured in the 1.6 µm film indicating a fully martensitic film, capable of thermal transformation into austenite was achieved.

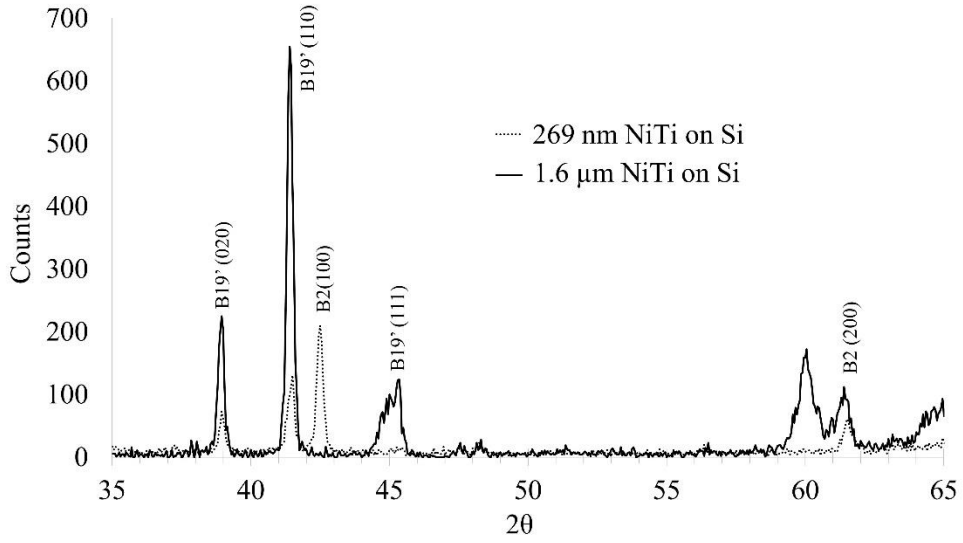

Figure 37 RT XRD scan of 269 nm thick NiTi overlaid with 1.6 um thick NiTi on Si (100) wafer. 1.6 µm wafer appears to have more significant volume fraction of M-phase compared to 269 nm thick NiTi. A volume fraction is computed as M-counts/A-counts and expressed as a %.

The microstructure associated with the transformation behavior of the NiTi films was investigated in more detail using supplemental XRD measurements in as-released and "activated" conditions. Figure 38 attributes the difference between the initial SME in released films to the SME following the first heat and cool cycle to a low temperature, thermo-mechanically induced ordering of NiTi crystals. XRD results show additional crystallization, or an appearance of an austenite peak, after heating the dry released NiTi flakes to 100 °C and allowing them to cool to room temperature (RT).

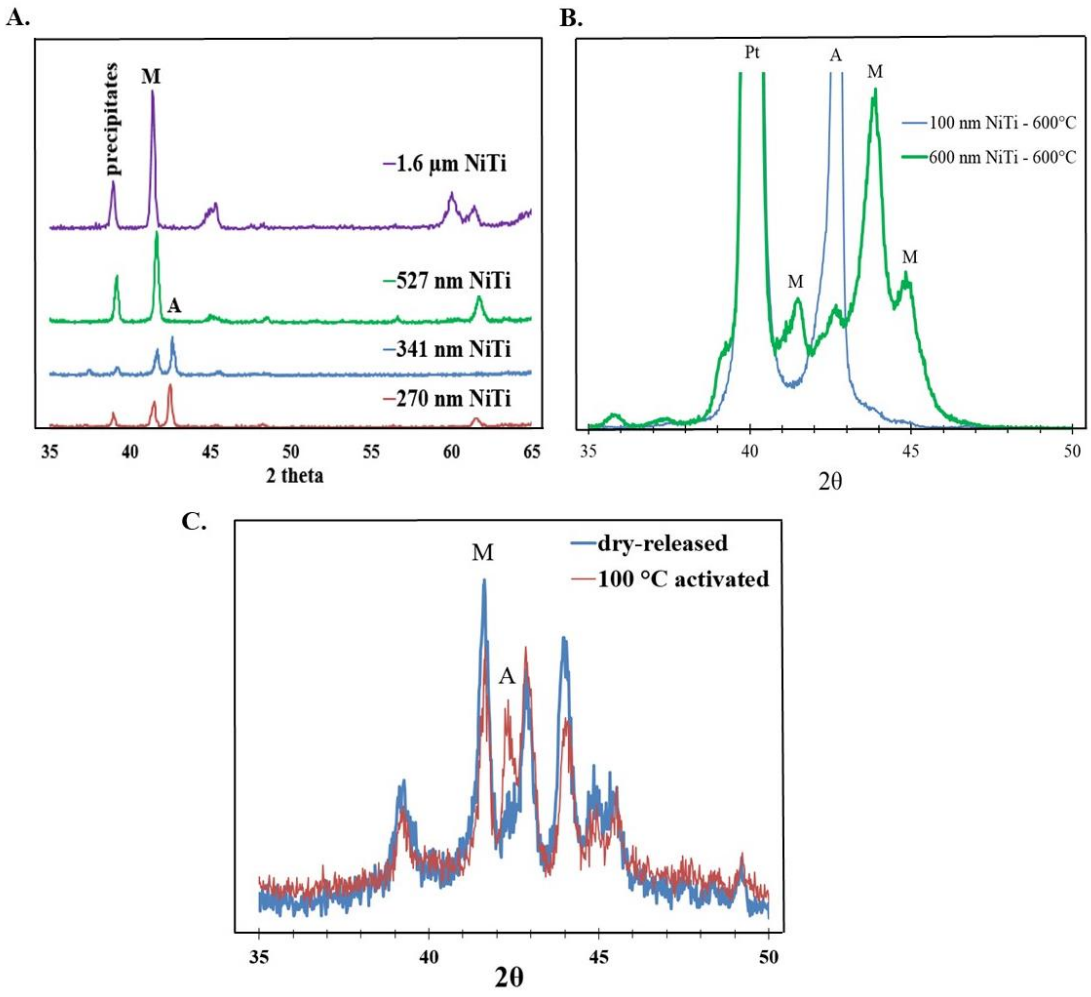

Figure 38 XRD spectra for a) in-situ crystallized NiTi on Si (100) wafer of various thickness, b) in-situ crystallized NiTi or various thickness on Pt "seed" layer on Si, c) 1 µm thick NiTi sputtered onto Si at 600 °C, wet etch patterned, and dry released in (blue) as-released, and (red) thermally activated conditions.

XRD was used to characterize NiTi on Si and NiTi on thin films of Pt on Si. The XRD data for NiTi of various thickness (270 nm to 1,600 nm) on Si in Figure 38A shows that the NiTi had a martensite phase present at RT, providing additional confirmation for reliable above-ambient phase change characteristics. The data for the two thinner cases also exhibited an austenite phase at RT, indicating a mix of both phases, as opposed to the desired fully martensitic phase. Figure

38B shows more detailed XRD spectra for 600 nm and 100 nm thick NiTi on 20 nm Pt, where different indicators of the martensite phase are present at RT for the 600 nm film. A Pt layer was used to provide a bimorph structure for the fabrication of out-of-plane actuators, and these XRD data confirm the presence of the desired room temperature Martensite B19' phase, indicating that thermal transformation into austenite would be accompanied by stress-induced actuation.

On the other hand, although the 100 nm NiTi film appeared crystallized with an austenite phase detected, no martensite was present in this material. Therefore, actuation above room temperature for this particular 100 nm film recipe was not expected. It is possible that additional aging at 600 °C could tune the microstructure to encourage a martensite phase at RT as shown previously in 100 nm films. Complicating some of the XRD analysis a bit, is that Pt-Si peak is in same location as austenite phase peak (42.5°).

3.4.3. Residual Stress in Constrained NiTi and Bimorph Films

The third method of characterization involved stress versus temperature measurements. Figure 39A shows a reversible phase change with onset at 60 °C upon heating for two different NiTi sputter deposition pressures of $Ni_{50}Ti_{50}$ on 200 nm Pt. Since NiTi was sputtered onto a thin film of Pt on Si for this set, the modified Stoney's equation (2) was used to determine the NiTi film stress. Assuming the thickness of the two films to be similar, the film sputtered at 5 mTorr exhibited a higher value of recovery stress, defined as the difference between initial stress and stress in the presumably austenitic phase at elevated temperature. Both films had a similar initial or residual stress of around 300 MPa. The maximum residual stress values peaked around 70 °C for each wafer in this experiment, and the process was reversible when cooled back to RT.

Figure 39B shows that the trend of higher recovery stress (approximately 900 MPa) at lower deposition pressure was the same for two 525 µm thick NiTi films, which in this case were

deposited onto Si and stress values were determined with standard Stoney equation (1). Residual stress was lower (70 MPa) for NiTi sputtered onto Si at 5 mTorr compared to the NiTi sputtered at 10 mTorr (230 MPa). Lower residual stress would generally be desired to reduce unwanted deformation of MEMS structures fabricated based on NiTi. These results are also useful, providing confirmation that the SME is similar when NiTi was deposited onto Pt or Si.

Wafer bow stress measurements were also performed on thinner films of 341 nm and 270 nm NiTi which were sputtered onto Si at 600 °C substrate temperature. Figure 39C shows a reversible SME in 341 nm and 270 nm films sputtered at 10 mTorr. Therefore, significant micro actuation should be achievable in even thinner films. Interestingly, the SME as indicated by stress versus temperature here was apparent in each case during the first heat and cool immediately following the NiTi sputter deposition cycle. This is in contrast to the released flakes characterized using DSC in Figure 33C which required an initial heat and cool activation cycle before the full SME was apparent.

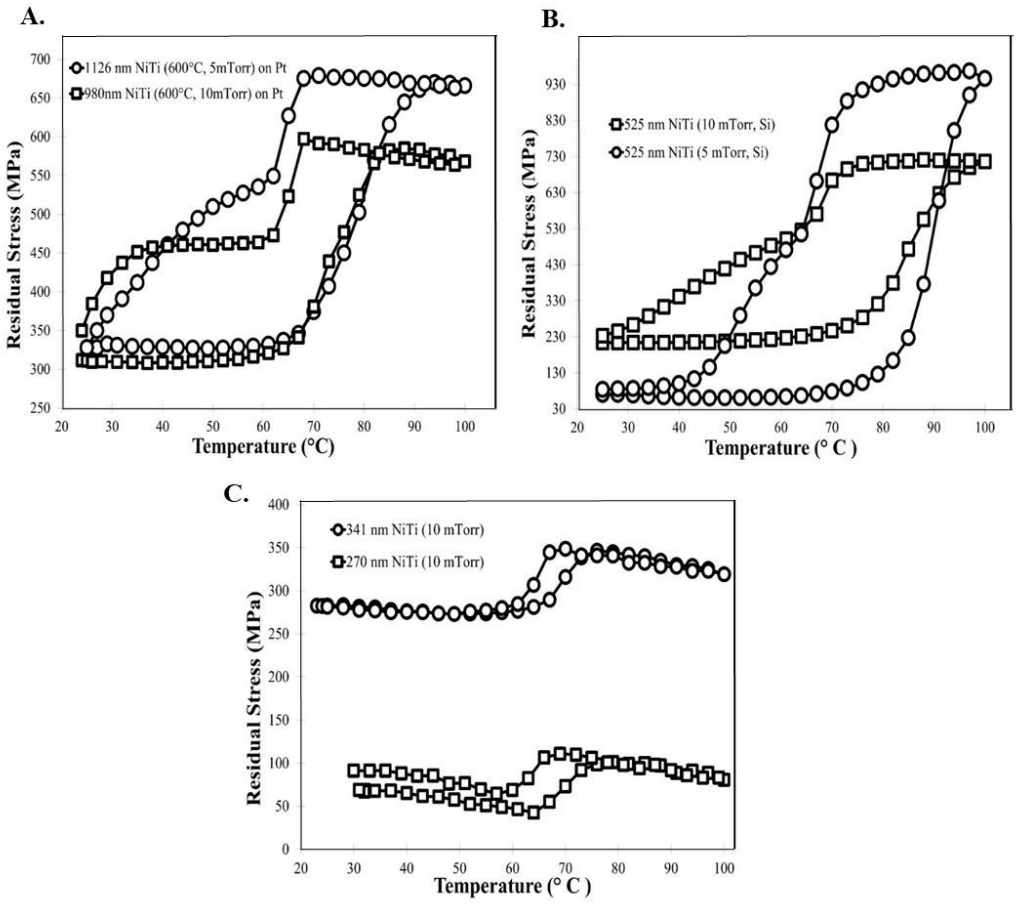

Figure 39. Stress vs. temperature plots for NiTi sputtered at 600 °C under different pressures onto 200 nm Pt for NiTi A) near 1 µm thickness, B) near half micron thickness, C) approaching 100 nm minimum film thickness for SMA properties.

3.4.4. Bending Characterization of Released Bimorph Actuators

We released micromachined cantilevers of NiTi on Pt by performing a dry etch release as described previously. Figure 40B shows a SEM image of released 1.4 µm thick NiTi on 200 nm Pt cantilevers with electroplated Au segments, 200 µm in width and with initial downward curvature. The downward curvature is likely attributed to the combination of room temperature residual stress in the Pt and NiTi layers, the latter of which presumably had only partially crystallized or partially ordered grains as suggested by the DSC results in Figure 39A. After an

activation heating and cooling cycle was performed, the devices had an out of plane curvature of 1.2 mm upward.

The application of Klein and Miller's equations [184] for a bi-layered structure with an initial strain differential $\Delta\epsilon_0$ between the layers yielded a predicted radius of curvature of 1.22 mm, calculated by assuming a strain differential arising primarily from thermal expansion coefficient differences between Pt and NiTi. Given that both films cooled from a deposition temperature of 600 °C:

$$\Delta\epsilon_0 = \int_{T_\infty}^{600°C} (\alpha_{NiTi} - \alpha_{Pt})dT \qquad (3)$$

Using α_{Pt} = 8.8x10^{-6}, α_{NiTi} = 6.6x10^{-6} for the martensite phase from 25 °C to 60 °C, and α_{NiTi} = 11x10^{-6} for the austenite phase from 60 °C to 600 °C, $\Delta\epsilon_0$ = 0.001111. The predicted radius of curvature resulting from this strain differential value was in excellent agreement with the fabricated NiTi/Pt bilayer. Incidentally, if one assumes only partial crystallization at the elevated deposition temperature, and an austenitic NiTi thermal expansion coefficient approaching that of the less-ordered martensitic phase, cooling from 600 °C would result in a negative strain differential and consequent negative curvature. This negative curvature is consistent with observations in Figure 40 for devices immediately following release. Measured results for activated films were also plotted in Figure 41B. For 200 nm Pt and NiTi films greater than 1 μm, model and experimental agreement was good. For 20 nm Pt, released radius of curvature agreement was better at the thin NiTi thickness value of 100 nm, although no SME, upon release or upon thermal cycling, was experimentally observed in the 100 nm film.

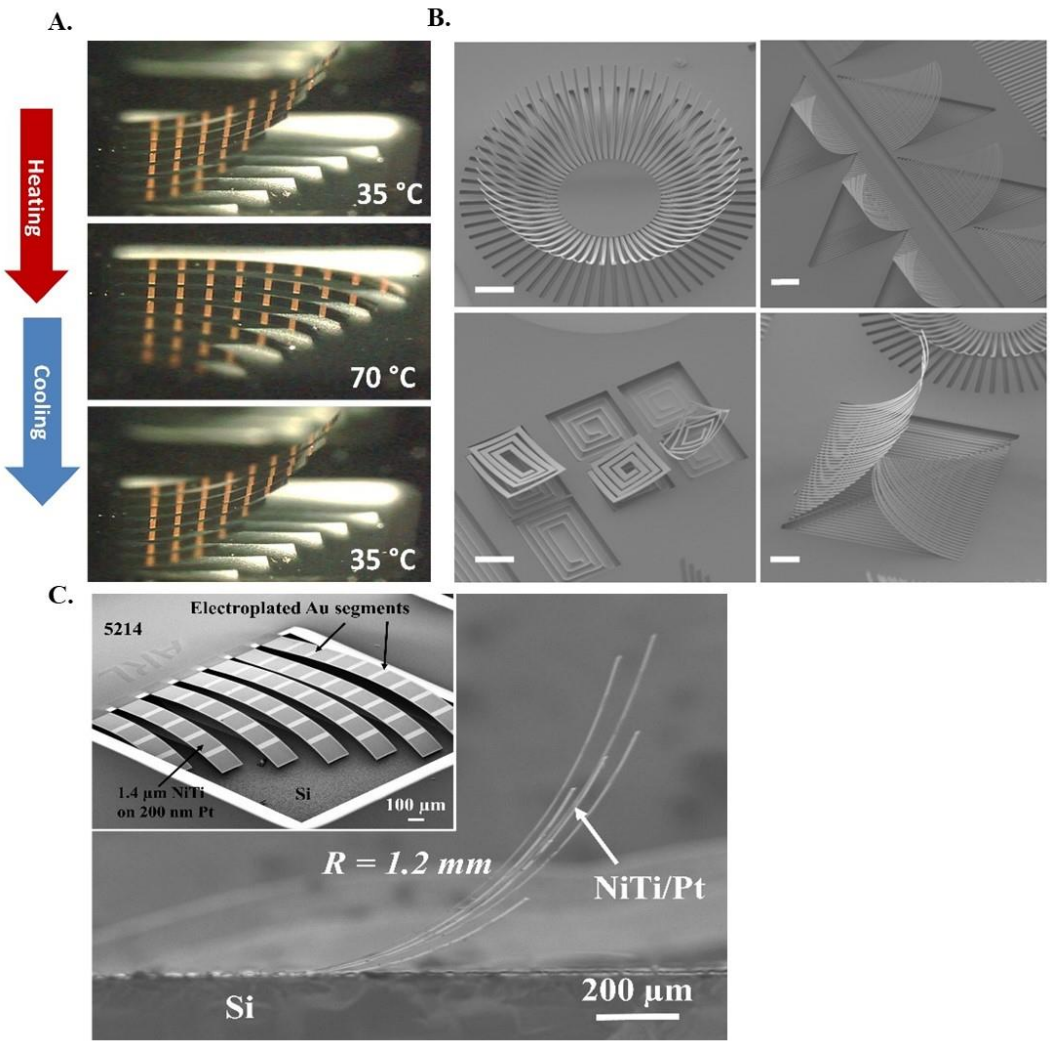

Figure 40 A) optical microscope video frame from thermal actuation, B) SEM images of various released structures from the 600 nm NiTi on 20 nm Pt fabrication run structures with 100-200 µm R_C (scale bars 100 µm), C) SEM of 1.4 µm NiTi on 200 nm Pt bimorphs in as released (curled down) and thermally activated (curled up) positions.

Figure 40B shows typical devices and test structures patterned in 600 nm NiTi on 20 nm Pt layers and released where activated curvature measured between 100-200 µm (upward curl) across different regions of the wafer. Equilibrium heating and cooling experiments were also conducted on released 1.4 µm NiTi on 200 nm Pt devices at 3 °C/min, consistent with DSC and stress versus temperature scans, while simultaneously recording video. Figure 41 includes the

video frames of the released and activated cantilevers ranging in length from 700 µm to 2 mm and a starting upward curvature of 1.2 mm. Upon heating above 70 °C, the phase change was mostly completed. At 100 °C, the devices were curled slightly downward into the Si pocket, with NiTi completely transformed into austenite at this point. These devices were thermally cycled over 50 times, with no optically discernable difference in starting and ending states. Figure 40 shows similarly curled and activated cantilevers for 600 nm NiTi on 20 nm Pt with cantilever length between 20 µm and 1 mm.

3.4.5. Optical Irradiation of SMA MEMS

Cantilever actuation under optical irradiation was also tested. As shown in Figure 41C, 1.4 µm thick NiTi on 200 nm Pt devices actuated into their downward state within 25 ms when irradiated at 7.2 W/cm^2. A slower actuation time of 230 ms was observed at 1.44 W/cm^2. The radius of curvature for the 600 nm NiTi / 20 nm Pt stack was 5.4 times tighter (200 µm) compared to the 1.2 mm curvature in the 1.4 µm thick NiTi stack. For the tightest curling (200 µm) 600 nm thick NiTi devices, a dynamic optical actuation experiment was performed where actuation time at various laser intensities was measured. These results are plotted in Figure 41A.

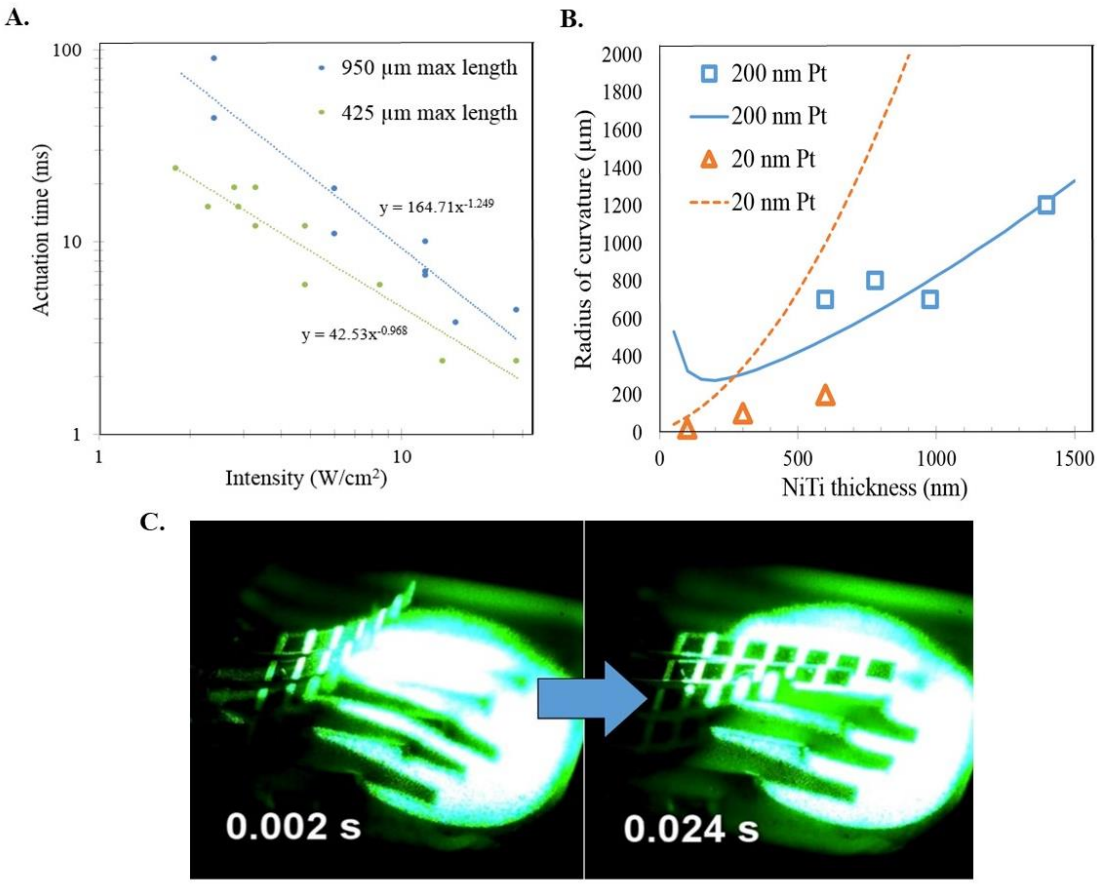

Figure 41. A) actuation time vs. laser irradiance for 600 nm NiTi on 20 nm Pt bimorphs, B) calculated and measured curvature radius for thermally activated NiTi on Pt bimorphs (1.4 µm on 200 nm Pt) C) Demonstration of passive laser irradiated device-specific actuation with a 532 nm "green" laser (~7.2 W/cm^2) in 24 milliseconds for the 1.4 µm thick NiTi device stack.

Devices demonstrated rapid actuation ranging from 2 ms to 90 ms, depending on optical power density as shown in Figure 41A. As would be expected for a cantilever beam clamped on one end to a heat sink, the actuation time followed a $1/I^2$ (I, being intensity) power law. Overall, the devices could be fully actuated in under 20 ms with intensities as low as 2 W/cm^2. The response time decreased to 3 ms with intensities over 14 W/cm^2.

3.5. Summary

This work used co-sputtering processes to deposit NiTi films and anneal them *in-situ*. The transformation behavior was verified with differential scanning calorimetry and XRD. The SME response was measured using wafer bow versus temperature measurements. Using this SMA material, which was co-sputtered at 600 °C and 5 mTorr chamber pressure with a near equiatomic composition, multiple device wafers of NiTi on Pt bimorph actuators were fabricated to characterize device bending radius for multiple NiTi and Pt thicknesses. Specifically, these device wafers allowed for the study of device radius of curvature for three different NiTi thicknesses on 20 nm Pt and four different NiTi thicknesses on 200 nm Pt. The 1.4 µm NiTi on 200 nm Pt could be actuated between 1.2 mm curvature and flat states. The device radius of curvature was reduced by a factor of 5.4 times when a thinner 600 nm NiTi on 20 nm Pt actuated between 200 µm curvature and flat states. The 100 nm thick NiTi devices did not exhibit the shape memory effect, consistent with XRD showing only austenite phase present at RT. As a demonstration for alternative actuation methods without the need for a wired power source, the optical actuation of our devices using a 532 nm "green" laser was also tested. Complete actuation was observed in under 3 ms for optical intensities down to 14 W/cm^2, indicating the potential for deployment in a variety of dynamic applications, such as passive-response, micro shutters and thermal switches.

In the following chapter, additional SMA MEMS actuators capable of electrical actuation were fabricated. The motivation in the following chapter is to address the limitations surrounding high-frequency actuation. The joule-heated SMA MEMS are characterized using laser Doppler Vibrometry starting at low frequencies and progressing to frequencies into the kHz using a pulsed electrical current to actuate the NiTi.

Chapter 4: Fabrication and Electrical Actuation of SMA MEMS Bilayer Actuators

4.1. Introduction

A major drawback for SMAs in many applications has been the low frequency response, which is typically on the order of 1 - 100 Hz or lower. In MEMS applications, the higher surface-to-volume ratios have enabled responses to be improved by an order of magnitude or more. By further shrinking the SMA film thickness and device dimensions, the frequency response may be improved even further. In this chapter a new, simplified process for fabricating sputtered, thin film SMA MEMS actuators based on NiTi alloy that consisted of only one photo step to pattern the actuators using SU-8 is presented. A fast actuation frequency response of up to 3,000 Hz with turn on voltages as low as 0.5 V for devices exhibiting microns of cantilever tip deflection over millions of cycles is demonstrated, indicating these new SMA MEMS actuators have potential application for low voltage switching, modulation and tuning. It was also possible predict their performance using an analytical model of a bimorph actuator. The following section details the development of an analytic model to guide the fabrication of NiTi and SU-8 bilayer actuators.

4.2. Modeling Curvature and Actuation of the SMA / SU-8 bilayer

Analytical modeling was used to obtain anticipated bi-layer stacks that would exhibit maximized deflections and help guide the fabrication of NiTi SMA bi-layer actuators. In other words, prior to the fabrication of NiTi / SU-8 bilayer actuators, an analytical model was developed to determine the expected deflections and curvature radius in the bi-layer MEMS. The modeling identified Micro-opto-electro-mechanical-systems (MOEMS) textbook (Motamedi) gives an

equation for phase-change induced deflection in a NiTi SMA film on Si cantilever. This model was extended to stressed SU-8 on top of NiTi. The recovery stress of NiTi film in part determines how much deflection is experienced during the thermally driven phase change. Key factors in determining optimal bending are the young's modulus (i.e. stiffness) of the bimorph members, thickness ratios, and length of cantilever.

$$\delta = \frac{3E_c\sigma_{rec}t_c t_f(t_c+t_f)l^2}{E_c^2t_c^4+E_fE_c\left(4t_c^3t_f+6t_c^2t_f^2+4t_ct_f^3\right)+E_f^2t_f^4} \quad \text{(eq. 4.1)}$$

Here, subscript c denotes cantilever substrate and subscript f denotes NiTi film.

Extended to the bi-layer SMA system, where NiTi serves as the bottom cantilever substrate, and a thin film of stressed SU-8 is deposited on top, (eq. 4.1 becomes):

$$d = \frac{3E_{NiTi}\sigma_{rec}t_{NiTi}t_{SU-8}(t_{NiTi}+t_{SU-8})l^2}{E_{NiTi}^2t_{NiTi}^4 + E_{SU-8}E_{NiTi}(4t_{NiTi}^3t_{SU-8}+6t_{NiTi}^2t_{SU-8}^2+4t_{NiTi}t_{SU-8}^3)+E_{SU-8}^2t_{SU-8}^4}$$

where:

σ_{rec} = recovery stress of the SMA MEMS actuator;
d = deflection of the SMA MEMS actuator;
l = total length of the SMA MEMS actuator;
E_{NiTi} = elastic modulus of NiTi layer;
E_{SU-8} = elastic modulus of SU-8 layer;
t_{NiTi} = thickness of NiTi layer;
t_{SU-8} = thickness of SU-8 layer.

The one factor that always complicates NiTi SMA bimorph actuator modeling is the inherent nonlinear changes in mechanical, material, and electrical properties in hysteretic manor. To this end, calculations were carried out using both martensite phase, austenite phase, and intermediate combinations.

Austenite phase (higher temperature, i.e. 80-100 °C)

$$E_{NiTi} = \sim 80\ GPa$$

Martensite phase (lower temperature, i.e. RT-50 °C)

$$E_{NiTi} = \sim 30\ GPa$$

Based on hundreds of SMA wafer stress scans, NiTi recovery stress, σ_{rec} is typically in the range of 300 - 500 MPa. Therefore, this range was used for preliminary calculations. The range of NiTi film thickness used in these calculations was 0.5 – 2.0 µm, as this is the range of NiTi film thickness investigated throughout this dissertation's body of work. Figure 42 depicts a plot of deflection of SU-8 on NiTi beam. NiTi thickness is varied. Constant in the calculation is E_{NiTi} = 80 GPa, recovery stress of 400 MPa, SU-8 modulus of 2 GPa, SU-8 thickness of 1.0 µm, and 200 µm length beam.

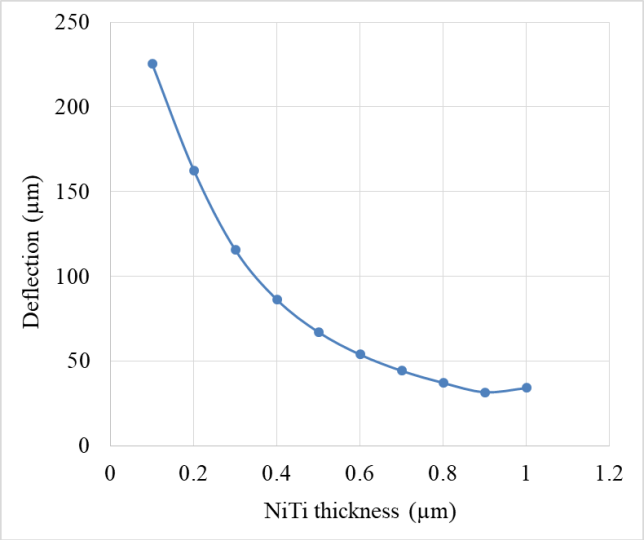

Figure 42 plot of deflection of NiTi / SU-8 beam. NiTi thickness is varied. Constant in the calculation is E_{NiTi} = 80 GPa, NiTi recovery stress of 400 MPa, SU-8 modulus of 2 GPa, SU-8 thickness of 1.0 µm, and 200 µm length beam.

At first glance this would seem to imply that the thinner NiTi beam should recover larger deflections during the phase change. This is presumably due to the significant reductions in beam

stiffness for thinner beams. This finding provided additional motivation to develop and optimize thinner NiTi SMA deposition recipes for significant amounts of recovery stress.

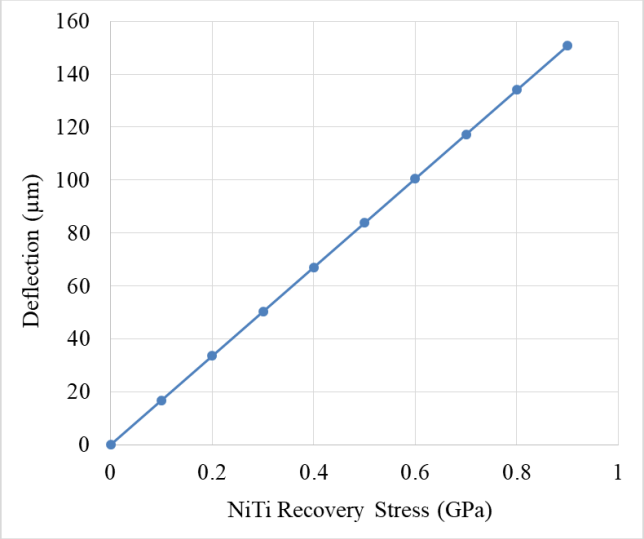

Figure 43 Calculated Deflection of NiTi cantilever based on NiTi recovery stress (MPa)

Figure 43 assumes fixed NiTi thickness (0.5 µm), and varies the recovery stress (MPa) in the NiTi film. This parameter is ultimately less tunable, but nonetheless typically measured recovery stress in NiTi films is 300 - 500 MPa (i.e. 0.3 - 0.5 GPa), thus according to the calculation, there is a linear dependence on recovered deflection during phase change and the NiTi recovery stress. In several instances, recovery stress of ~ 900 MPa have been measured, so although a less common occurrence, this curve is still based in reality. Therefore, as it would have intuitively been expected to be the case, a higher recovery stress film (based on wafer bow versus temperature), would give the benefit of increased deflections due to the shape memory effect. In the next section, we extend the modeling of the SMA phase change of SU-8 on NiTi bimorph actuator configuration.

4.2.1. Contour Plots for SU-8 on NiTi bilayer

It has been reported, that there exists a relationship between sputtered NiTi film thickness and the corresponding recovery stress. In this section, an analytical model and optimization problem for SMA-induced deflection was formulated and solved in MATLAB's Optimization Toolbox. *Figure 44* presents a data plot from literature review relating the recovery stress in NiTi film to the NiTi film thickness. A maximum recovery stress of 600 MPa happens for NiTi films with thickness in the range of 750 nm. Below 500 nm film thickness, the recovery stress due to SME begins to significantly drop off and eventually vanishes altogether as was shown in several references [11, 92].

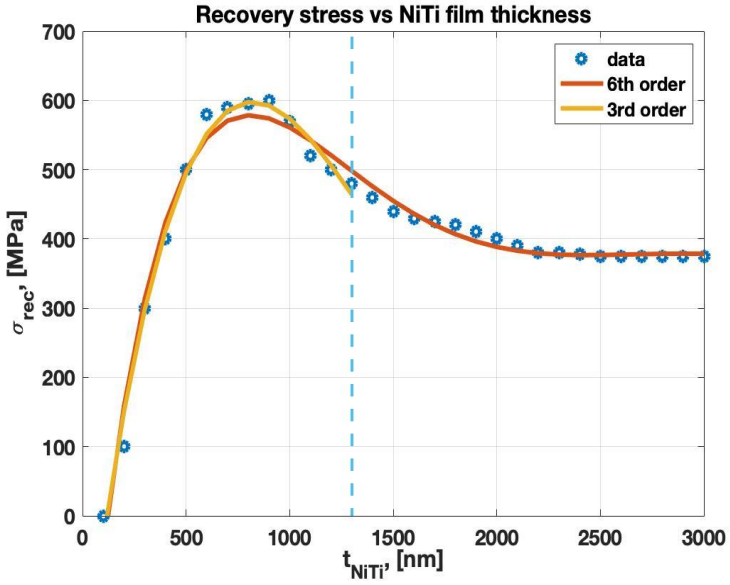

Figure 44 Relation between recovery stress (MPa) and NiTi film thickness (nm) adapted from [11].

The first optimization problem seeks to maximize deflection of the SU-8 / NiTi bilayer by calculating deflection for every combination of SU-8 and NiTi thicknesses over realistic upper and lower bounds. In other words, minimizing the negative deflection was formulated and solved. The

following optimization problem was solved to arrive at optimal NiTi and SU-8 thicknesses which would yield the most phase-change induced deflections.

$$minimize:$$

$$f = \frac{-3E_{NiTi}\sigma_{rec}t_{NiTi}t_{SU-8}(t_{NiTi}+t_{SU-8})l^2}{E_{NiTi}^2t_{NiTi}^4 + E_{SU8}E_{NiTi}(4t_{NiTi}^3t_{SU-8} + 6t_{NiTi}^2t_{SU-8}^2 + 4t_{NiTi}t_{SU-8}^3) + E_{SU-8}^2t_{SU-8}^4}$$

Subjected to:

$$g_1: 100\times10^{-6} - l \le 0;$$
$$g_2: l - 300\times10^{-6} \le 0;$$
$$g_3: 150\times10^{-9} - t_{NiTi} \le 0;$$
$$g_4: t_{NiTi} - 1300\times10^{-9} \le 0;$$
$$g_5: 200\times10^{-9} - t_{SU8} \le 0;$$
$$g_6: t_{SU8} - 2000\times10^{-9} \le 0;$$
$$g_7: -\sigma_{rec} \le 0$$
$$h_1: \sigma_{rec} - 5.36\times10^{26}{t_{NiTi}}^3 + 2.15\times10^{21}{t_{NiTi}}^2 - 2.45\times10^{15}t_{NiTi} + 2.58\times10^{8} = 0$$

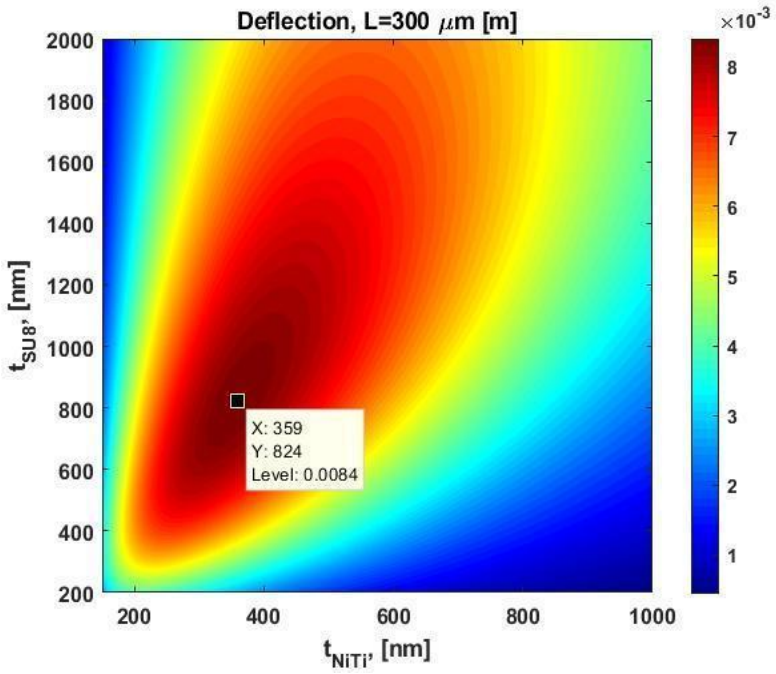

Figure 45 Optimization contours for the case where SU-8 elastic modulus is 2 GPa. Variables considered are individual layer thicknesses: NiTi (x-axis) and SU-8 (y-axis).

Based on this model, it was expected that the largest SMA induced deflection would occur for the case of NiTi thickness of 359 nm and SU-8 thickness of 824 nm as shown in Figure 45. After solving the optimization problem for single objective (maximize the deflection), the model was extended to multi-objective case which would try to simultaneously maximize deflection and curvature.

4.2.2. Multi-objective Optimization Problem Formulation

The curvature of a bilayer elastic material is given as [184].

$$K = \frac{-E'_{SU8} t_{SU8} E'_{NiTi} t_{NiTi} (t_{NiTi} + t_{SU8})}{G(E'_{SU8} t_{SU8} + E'_{NiTi} t_{NiTi})} \Delta\varepsilon$$

where

$$G = E'_{SU8} t_{SU8}^2 \left(\frac{t_{NiTi}}{2} - \frac{t_{SU8}}{6} - \theta\right) - E'_{NiTi} t_{NiTi} \left[t_{SU8} \left(t_{SU8} + \frac{t_{NiTi}}{2}\right) + \frac{t_{NiTi}^2}{6} + \theta(2t_{SU8} + t_{NiTi}) \right]$$

and

$$\theta = \frac{t_{NiTi} t_{SU8} (E'_{NiTi} - E'_{SU8})}{2(E'_{SU8} t_{SU8} + E'_{NiTi} t_{NiTi})}$$

and

$$\Delta\varepsilon = (\alpha_{SU8} - \alpha_{NiTi})\Delta T$$

Here ρ is the curvature radius generally expressed in units of μm. Δε is a strain differential term resulting from CTE mismatch and temperature difference experienced during the processing. θ is a correction factor used in the placement of neutral plane. E' is the biaxial modulus defined as E/(1-v) where v is Poisson ratio and E is Young's modulus. Poisson ratios are assumed to be 0.22 for SU-8 and 0.33 for NiTi. α_{SU-8} is reported to be 52*10-6/°C. α_{NiTi} (depending on austenite or martensite phase) is reported to be 6.6 or 11*10-6/°C. For simplicity sake, an intermediate value of α_{NiTi} = 9*10-6/°C is used. Units for theta term is nm or m. Units for G term is Pa*nm3 or Pa*m3.

Therefore, unit for curvature is in nm or m. Δε term is unitless. The following optimization problem is solved.

Curvature is:

$$K = -\frac{E'_{SU8}t_{SU8}E'_{NiTi}t_{NiTi}(t_{NiTi}+t_{SU8})}{G(E'_{SU8}t_{SU8}+E'_{NiTi}t_{NiTi})}\,\Delta\varepsilon$$

Maximize:

$$\rho = \frac{1}{K} = -\frac{G(E'_{SU8}t_{SU8}+E'_{NiTi}t_{NiTi})}{E'_{SU8}t_{SU8}E'_{NiTi}t_{NiTi}(t_{NiTi}+t_{SU8})\Delta\varepsilon}$$

Subjected to:

$$g_1: 150\times10^{-9} - t_{NiTi} \le 0;$$
$$g_2: t_{NiTi} - 1300\times10^{-9} \le 0;$$
$$g_3: 200\times10^{-9} - t_{SU8} \le 0;$$
$$g_4: t_{SU8} - 2000\times10^{-9} \le 0;$$
$$h_1: G - E'_{SU8}t_{SU8}^2\left(\frac{t_{NiTi}}{2}-\frac{t_{SU8}}{6}-\theta\right) - E'_{NiTi}t_{NiTi}\left[t_{SU8}\left(t_{SU8}+\frac{t_{NiTi}}{2}\right)+\frac{t_{NiTi}^2}{6}+\theta(2t_{SU8}+t_{NiTi})\right] = 0$$
$$h_2: \theta - \frac{t_{NiTi}t_{SU8}(E'_{NiTi}-E'_{SU8})}{2(E'_{SU8}t_{SU8}+E'_{NiTi}t_{NiTi})} = 0$$

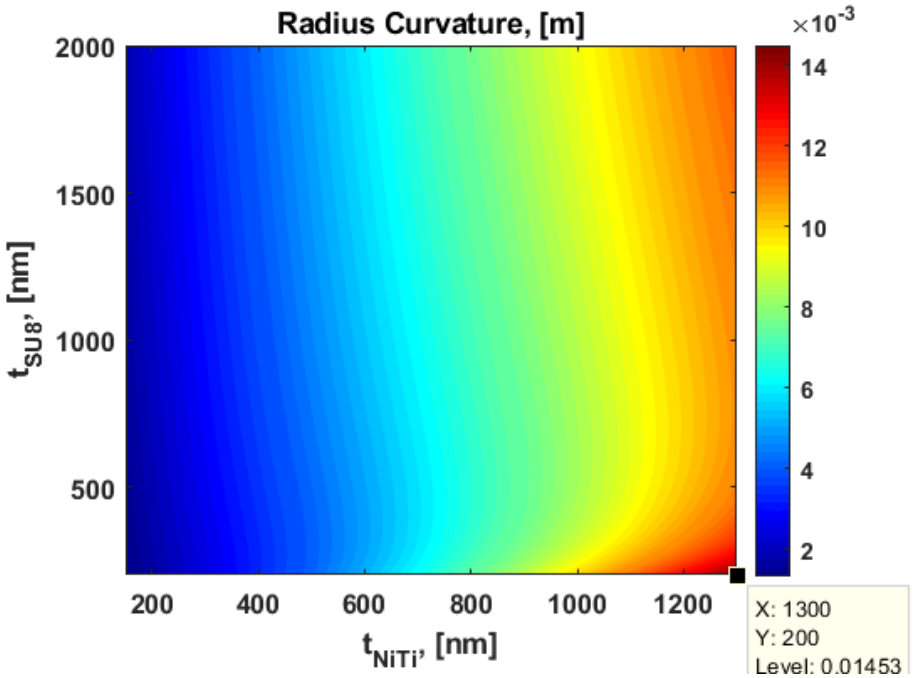

Figure 46 MATLAB generated contour plot of Curvature Radius [m], against the primary design variables (i.e. t_{NiTi} and $t_{SU\text{-}8}$).

Curvature Radius is maximized for the thickest values of NiTi and thinnest values of SU-8. The result is intuitive because this is the stiffest beam (from the perspective of thickest NiTi with much larger Young's modulus compared to SU-8). Thinner SU-8 means the effect from strain differential and CTE mismatch-induced stress contribution is minimized and contributes less to curvature radius. Overall, this means that upper bound on NiTi thickness and lower bound on SU-8 thickness are active constraints for objective function 2.

For the multi-objective optimization problem, the deflection and curvature radius of *SMA* bimorph actuator are maximized simultaneously. So, the multi-objective optimization problem can be stated as following:

maximize:

$$\mathbf{f_1}: \rho = -\frac{G(E'_{SU8}t_{SU8}+E'_{NiTi}t_{NiTi})}{E'_{SU8}t_{SU8}E'_{NiTi}t_{NiTi}(t_{NiTi}+t_{SU8})\Delta\varepsilon}$$

$$\mathbf{f_2}: d = \frac{3E_{NiTi}\sigma_{rec}t_{NiTi}t_{SU8}(t_{NiTi}+t_{SU8})l^2}{E_{NiTi}^2 t_{NiTi}^4 + E_{SU8}E_{NiTi}\left(4t_{NiTi}^3 t_{SU8} + 6t_{NiTi}^2 t_{SU8}^2 + 4t_{NiTi}t_{SU8}^3\right) + E_{SU8}^2 t_{SU8}^4}$$

Subjected to:

$$\mathbf{g_1}: 100 \times 10^{-6} - l \leq 0;;$$
$$\mathbf{g_2}: l - 300 \times 10^{-6} \leq 0;$$
$$\mathbf{g_3}: 150 \times 10^{-9} - t_{NiTi} \leq 0;$$
$$\mathbf{g_4}: t_{NiTi} - 1300 \times 10^{-9} \leq 0;$$
$$\mathbf{g_5}: 200 \times 10^{-9} - t_{SU8} \leq 0;$$
$$\mathbf{g_6}: t_{SU8} - 2000 \times 10^{-9} \leq 0;$$
$$\mathbf{g_7}: -\sigma_{rec} \leq 0;$$

$$\mathbf{h_1}: \sigma_{rec} - 5.36 \times 10^{26} {t_{NiTi}}^3 + 2.15 \times 10^{21} {t_{NiTi}}^2 - 2.45 \times 10^{15} t_{NiTi} + 2.58 \times 10^8 = 0;$$
$$\mathbf{h_2}: G - {E'}_{SU8} t_{SU8}^2 \left(\frac{t_{NiTi}}{2} - \frac{t_{SU8}}{6} - \theta\right) - {E'}_{NiTi} t_{NiTi} \left[t_{SU8} \left(t_{SU8} + \frac{t_{NiTi}}{2}\right) + \frac{t_{NiTi}^2}{6} + \theta(2t_{SU8} + t_{NiTi}) \right] = 0;$$
$$\mathbf{h_3}: \theta - \frac{t_{NiTi}t_{SU8}\left({E'}_{NiTi} - {E'}_{SU8}\right)}{2({E'}_{SU8}t_{SU8} + {E'}_{NiTi}t_{NiTi})} = 0.$$

Due to the conflicting nature of the two objective functions, the contour plot for the multi-objective function has changed substantially. Maximizing the radius is favored by a larger t_{NiTi} as opposed to a smaller thickness required to maximize deflection. The optimal solution of multi-objective function as shown in Figure 47 has a larger $t_{NiTi.}$

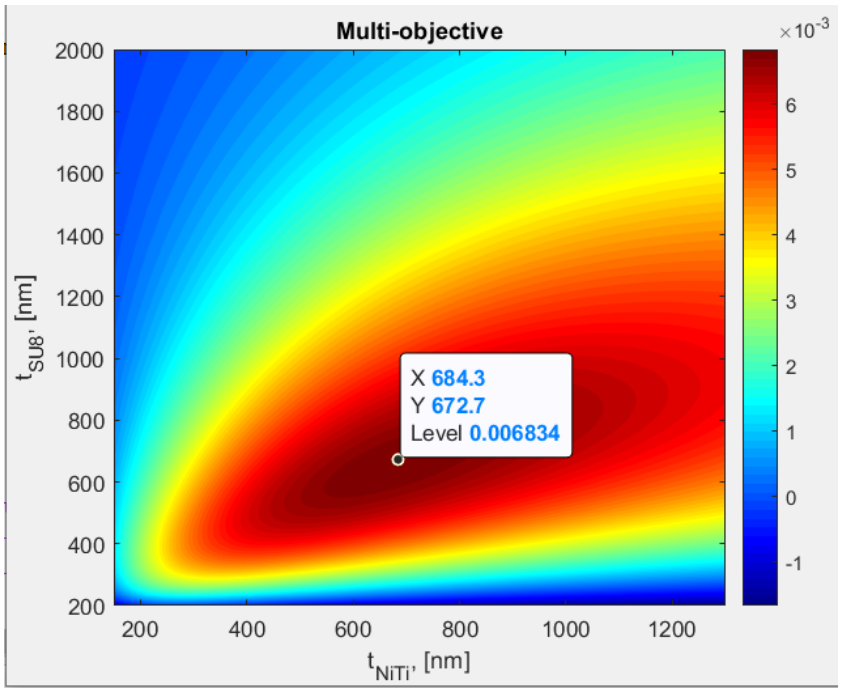

Figure 47 Optimal Solution for simultaneous multi-objective optimization of deflection and curvature radius.

Once the optimal objective values for deflection and curvature were established, a sensitivity analysis regarding the following variables was performed, which experimentally could be varied with relative ease. The thickness values x1 and x2, corresponding the NiTi and SU-8 thicknesses, can be changed by varying the spin speed for SU-8 coating: faster spins corresponding to thinner films of SU-8 and vice-versa. For NiTi, longer sputter time would be used for thicker films and vice-versa. Young's modulus can be varied by deposition conditions for NiTi and curing/baking temperatures and conditions for SU-8. To perform the sensitivity analysis for Objective 1 (which dealt with maximizing deflection), the optimal thickness for SU-8 was kept fixed and NiTi thickness was varied to investigate how it changes. Similarly, a function was plotted (as shown in Figure 48) which showed how the maximum deflection would be expected to change for small changes in NiTi and SU-8 elastic modulus. As NiTi elastic modulus spans the range of

40 – 80 GPa, the changes in maximum deflection are not significantly affected. A maximum deflection is expected for the lower bound on NiTi modulus.

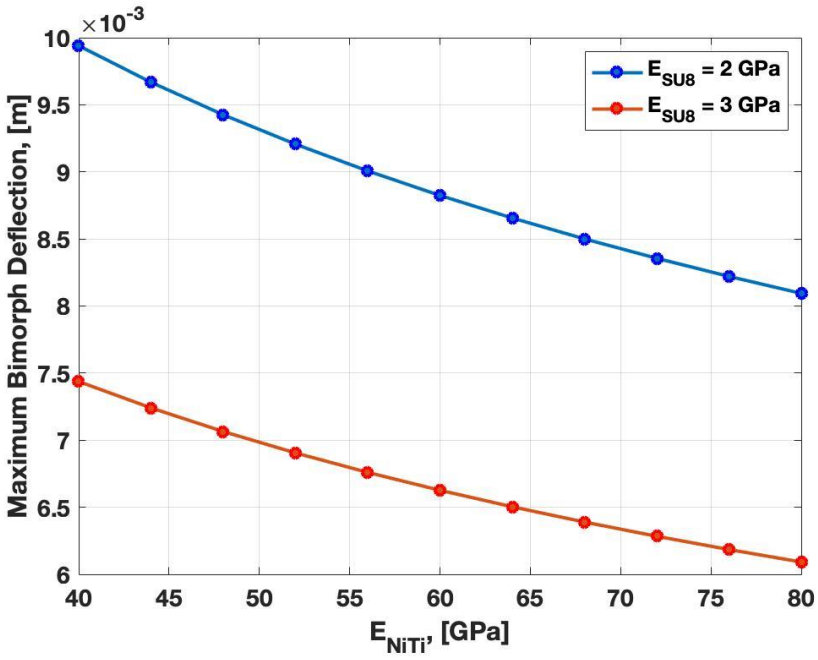

Figure 48 Maximum bimorph deflection with a variation of Young's modulus of NiTi and SU-8 layer

4.2.3. Summary

This section described the analytical model and optimization problem developed for SU-8 on NiTi bi-layer. The model was used to guide the fabrication in the following section. In other words, the model influenced the targeted thickness values for NiTi and SU-8 which were shown to exhibit the largest deflections induced by SMA phase-change. The following section details the material and device fabrication of SU-8 on NiTi MEMS actuator, which was influenced by the modeling presented in this section.

4.3. Material and Device Characterization and Fabrication

Figure 49 shows a measured stress versus temperature loop typical for NiTi martensite-austenite phase change with important definitions defined for recovery stress, thermal hysteresis, as well as the austenite start, austenite finish, martensite start and martensite finish temperatures.

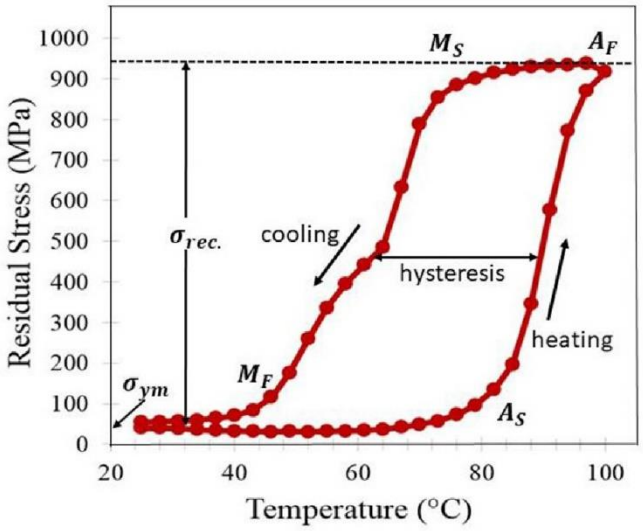

Figure 49 Stress versus. temperature hysteresis loop for 270 nm thick SMA film on Si wafer (5 mTorr deposition pressure) depicting important parameters including A_s, A_f, M_s, M_f, recovery stress, residual stress, and thermal hysteresis.

A large reversible stress difference (~900 MPa) was measured in the 270 nm thick sample deposited at 5 mTorr as shown in Figure 49, which was chosen as the starting wafer for the joule-heater actuator device study. The optimal thickness according to the model was 370 nm, so future iterations could possibly explore additional device fabrications to target even more deflections resulting from the SMA phase-change. This is most likely due to the phase change between B19' martensite and austenite which is accompanied by larger transformation stresses and strains as well as much larger thermal hysteresis. The thermal hysteresis is ~40 °C. A_s is 75 °C, A_f is 95 °C, M_s is 65 °C, and M_f is 40 °C. The residual stress is actually quite low, around 50 MPa. The NiTi was

deposited onto a heated wafer (600 °C) for 18 minutes, at 15 nm/minute to obtain an *in-situ* crystallized NiTi SMA film of 270 ± 5 nm thickness as shown Table 6.

To fabricate the joule heater devices, the following sequence was performed for the device build. This process is similar to what was reported on in [179], where NiTi was deposited onto Pt. Here, the main difference is that NiTi was deposited onto Si, as opposed to a Pt 'seed' layer. The process flow is detailed in Figure 50. NiTi was blanket co-sputtered at 600 °C substrate temperature onto the Si wafer. Ion milling through the NiTi film using a photo patterned layer of ~2 µm thick AZ 5214e photoresist. With this pattern, the joule heater was etched on top of the Si wafer with larger NiTi bond pads (200 µm squares) to eventually land contact probes. Another layer of the ~2 µm thick AZ 5214e photoresist was spin coated and developed to define exposed Si etch regions around the NiTi joule heater devices. This resist also masked off the bulk of the Si wafer surface during the device release process, which consisted of a xenon difluoride (XeF_2) etch to undercut the devices. A 1 µm thick film of SU-8 2000.5 negative photoresist was spin coated on top of the NiTi. After photomask exposure and pattern the SU-8 was only remaining on top of the NiTi beam and the NiTi bond pads were exposed in order to facilitate experimental electrical characterizations. The SU-8 was spin coated at 4,000 rpm and baked for 2 minutes at 95 °C, and exposed with a contact aligner and mask plate at 160 mJ cm^{-2}. The complete SU-8 2000.5 recipe used is detailed in Table 7. Upon release, the devices curled upwards, most likely due to the thermal expansion mismatch between NiTi and SU-8. In the austenite phase of film deposition the CTE of NiTi is reported to be near 11ppm/°C compared to SU-8 which is reported as ~53 ppm/°C. The larger rate of contraction of the uppermost SU-8 layer would result in the stress profile the results in upward curl, as was seen in the released devices.

This SMA bimorph device is similar to the microgrippers reported by Gill [18], in that both

used a photopatternable polymer with CTE much larger than NiTi and subsequent thermal processing to induce an out of plane beam curvature once released from substrate.

Table 6 Deposition parameters used for NiTi film in the SU-8 on NiTi joule heater actuator fabrications.

NiTi deposition in the AJA ATC co-sputter tool	
NiTi target power (W)	375
Ti target power (W)	250
NiTi thickness (nm)	270
Deposition time (min.)	18 min at 15 nm / min.
Deposition temperature (°C)	600
Argon Flow (sccm)	60
Sputter pressure (mTorr)	5

Table 7 Parameters used to fabricate SU-8 on top of patterned NiTi actuator.

SU-8 2000.5 fabrication (Microchem corp.)	
Material	SU-8 2000.5
Spin Speed (rpm)	4000
SU-8 thickness (μm)	1
Soft Bake	2 min. @ 95°C
Exposure	160 mJ cm^{-2}
Post exposure bake (PEB)	4 min @ 95°C
Develop	50 sec. in SU-8 developer
Rinse	Fresh SU-8 developer + IPA

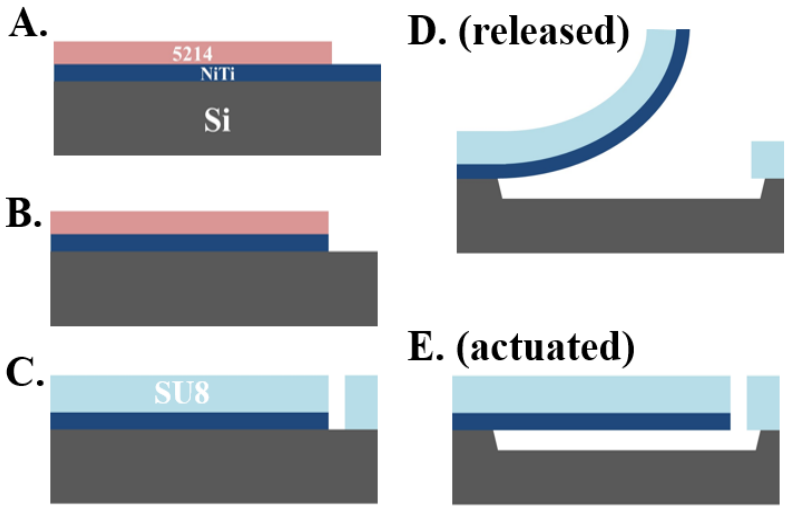

Figure 50 Process Flow for SU-8 on NiTi MEMS actuators

Well known Stoney's equation was used to back out the NiTi residual stress based on measured film and wafer thicknesses and measured wafer curvature pre and post film deposition. The deflection of a bi-layer cantilever due to a temperature variation is expressed by the following equation, where the geometric parameters are those indicated in

$$\delta = L^2 \frac{3(1+m)^2}{t\left[3(m+1)^2 + (1+mn)\left(m^2 + \frac{1}{mn}\right)\right]}(\alpha 2 - \alpha 1)(\Delta T)$$

α_1 and α_2 are the thermal expansion coefficients (CTE) of the bottom and top layer materials; n is the ratio of young's modulus of layer 1 and 2 (Y_1/Y_2). M is the ratio of layer 1 and layer 2 thickness, t is the total cantilever thickness. The equation used to model radius of curvature is given as:

$$\frac{1}{R} = \frac{6m}{t(m+1)^2}(\alpha 2 - \alpha 1)(T - T0)$$

Where R is the radius of curvature and t, m, and α are same as above.

The joule heater SMA device geometry and cross-section of fabricated SU-8 on NiTi MEMS actuators devices is depicted in Figure 51. Figure 52 shows the measured radius of curvature of the released SU-8 on NiTi as a function on SU-8 post bake temperature. There is a clear dependence showing that hotter post bake temperature results in a beam with tighter curling radius once released from the substrate.

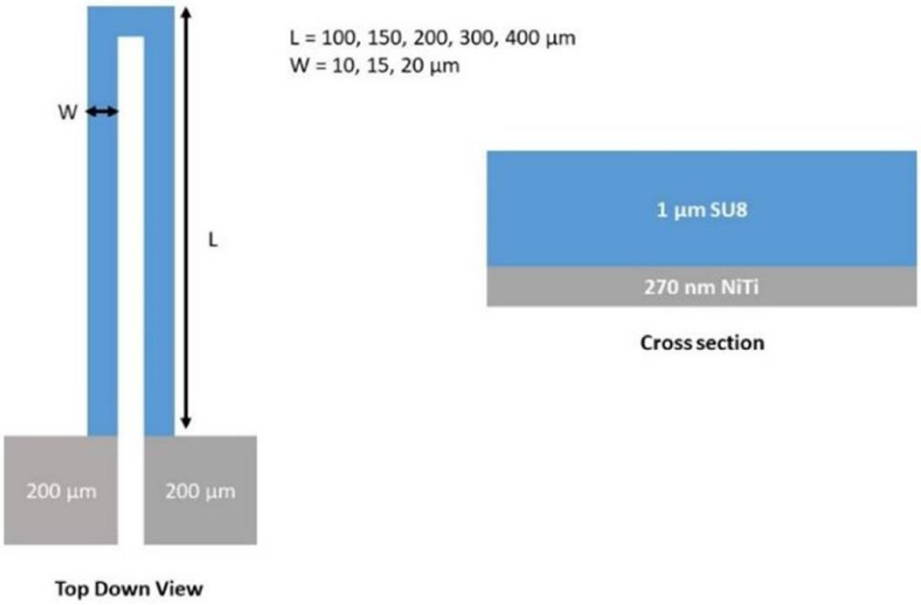

Figure 51. Schematic of the fabricated MEMS SMA bimorph actuators (top down view), and cross section. NiTi is grey and SU-8 is blue.

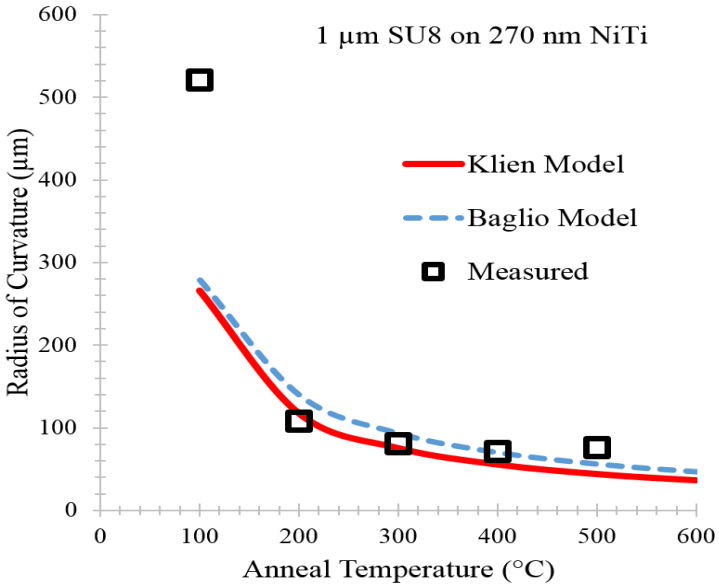

Figure 52. Modeled and measured radius of curvature for 50 µm length cantilevers, 5 µm wide of 1 µm SU-8 on 270 nm NiTi for various SU-8 post-bake temperatures

4.4. Device testing and actuation demonstrations

For the electrical actuation tests on joule heater devices, Laser Doppler Vibrometry (LDV) was used to record cantilever displacement. The laser was focused 20 µm from the base of the cantilever beam to measure the displacement at that point, which was then related to the radius of curvature using Euler-Bernoulli beam theory from which the displacement was derived. An arbitrary signal generator was integrated, capable to produce arbitrary voltage profiles (i.e. square, triangle, sinusoidal) to actuate the bimorph structures.

A microscope image snapshot of the LDV experiment is shown in Figure 53. The interrogation spot is focused on the SU-8 on SMA beam with an initial upward curl and deflection of 0 µm. When actuated with a voltage input, the cantilever deflects downward, hence the negative cantilever deflection. The maximum deflection appears to be 1.2 µm at the interrogation spot. Figure 58 shows optical image of the cantilever at 0.0 V and 1.0 V, whereby a significant uncurling

of the cantilever due to thermal phase-change is obvious.

Figure 61 shows the joule heater beam deflection response at a 2 Hz with 1 V excitation. Although, not shown here, this same device has been cycled at 2 kHz for over one million cycles. The SMA cantilever deflection is also shown in Figure 62 over a voltage sweep from -0.6 to 0.6 V, with an absolute turn on voltage of 0.5 V. Using a curve fit to the bending beam, it was determined that the bending radius was 178 +/- 12 μm at room temperature and 789 +/- 8 μm upon actuation, which corresponds to a radius change of 611 μm. This significant change in curvature radius as a result of heat-induced phase change is shown in Figure 59.

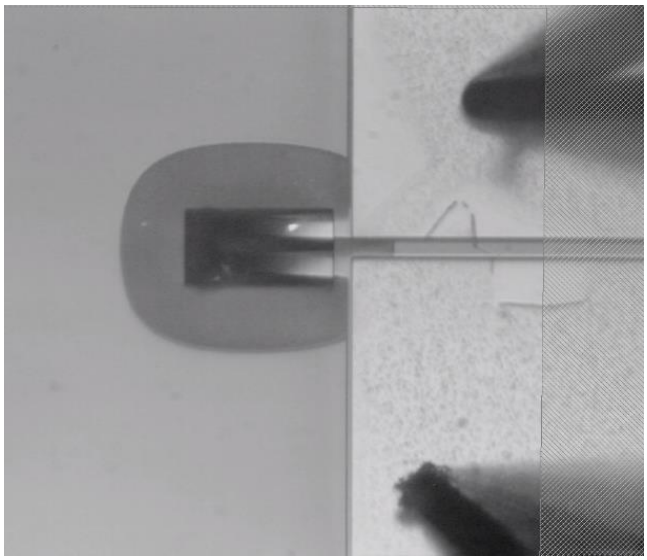

Figure 53. Snapshot of the LDV experiment with patterned NiTi probe pads, joule heater resistor (upward curl), and laser spot focused on a single beam of the joule heater (white dot).

Figure 58 shows optical microscope pictures of the device under no load and actuated with 1.0 V continuous bias. The uncurling of the device towards a flatter position is very clearly seen in this view. Figure 59 shows the Olympus LEXT confocal microscope "image" for the beam unheated and at 100 °C on hotplate. The curvature of the beam from these measurements was used to determine the radius of curvature in unheated and actuated states. According to the stress-

temperature loop, it would be expected that the SMA beam is fully actuated at 100 °C. Figure 60 shows SEM image of released joule heater beam. In this image the bilayer SU-8 / NiTi beam curls out of the substrate due to residual stresses built up during the fabrication process. In other words, large CTE mismatch between NiTi and SU-8, combined with thermal processing to cure the SU-8, results in a stressed interfacial region, that induced curvature of the bi-layer upon release from substrate. The composite beam is clearly curled upwards and image contrast makes it easy to discern the NiTi bond pads (white) and the SU-8 photoresist (grey).

4.4.1. Electrical Characterization of the NiTi SMA Bimorph Joule Heater Actuators

SU-8 on NiTi joule heater device were tested using pulsed electrical currents to joule-heat the NiTi and induce the phase-change. Figure 53 shows a microscope picture of a typical device. In the CAD design, three different beam widths (10 µm, 15 µm, 20 µm),and five different beam lengths (100 µm, 150 µm, 200 µm, 300 µm, 400 µm) were fabricated. By ramping current in intervals from 2-25 mA and measuring voltage, we were able to determine NiTi device resistance (Ohms) based on ohms law, V = IR. We measured resistance through the joule heater NiTi devices to vary between 64 - 173 Ohms. Naturally, the shortest and widest beam designs had the least resistance (i.e. ~25 Ohms for 20 µm wide, 100 µm long). The largest measured resistance was indeed the longest beam with narrowest beam width (400 µm long, 10 µm wide). Table 8 summarizes the inferred device resistance for each of the various lengths and widths of the joule heater. The results match what would be expected. In other words, the lowest device resistance (24.8 Ohms) corresponds to the shortest and widest beam, and the highest resistance corresponds to the longest and most narrow beam (173.2 Ohms).

Table 8 NiTi joule heater device resistance inferred from current and voltage measurements.

	Resistance (Ohms)		
Length (µm)	**10 µm wide**	**15 µmwide**	**20 µm wide**
100	64.1	48.2	24.8
150	128.8	50.6	56.8
200	107.8	69.4	61.8
300	121.8	103.6	65.6
400	173.2	93.4	84.6

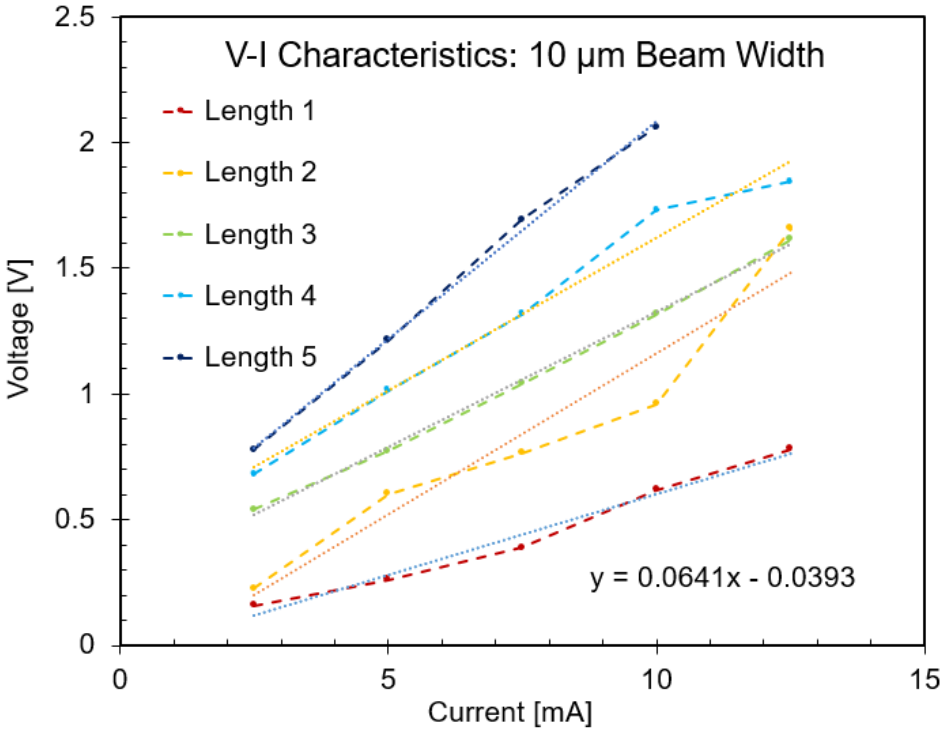

Figure 54 measured current and voltage (IV) data used to determine device resistance in the NiTi joule heaters for 10 µm wide beams of varied length.

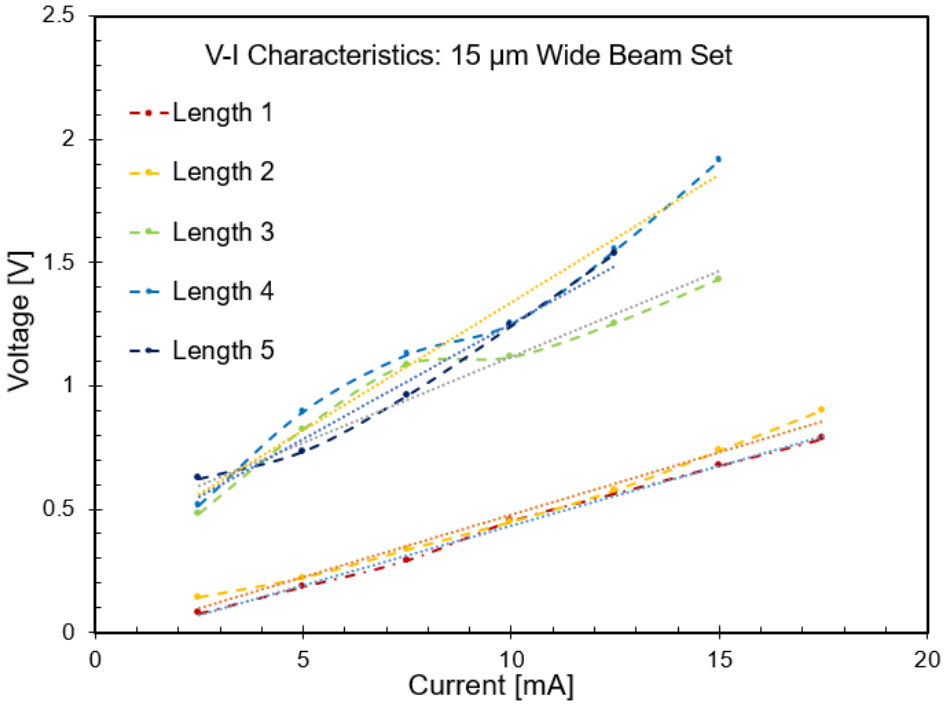

Figure 55 measured current and voltage (IV) data used to determine device resistance in the NiTi joule heaters for 15 µm wide beams of varied length.

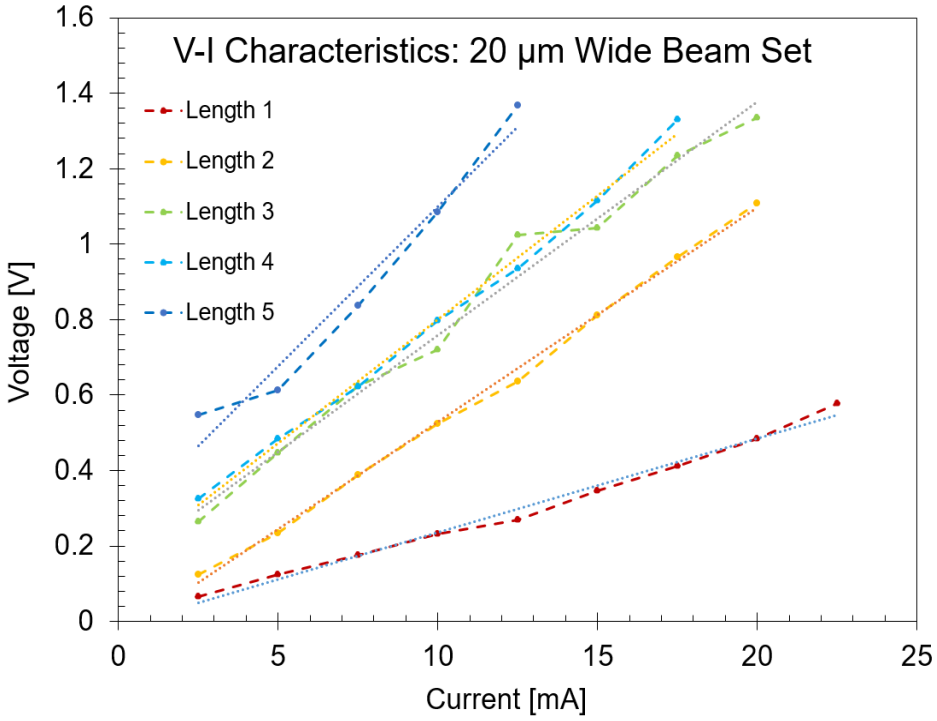

Figure 56 measured current and voltage (IV) data used to determine device resistance in the NiTi joule heaters for 20 µm wide beams of varied length.

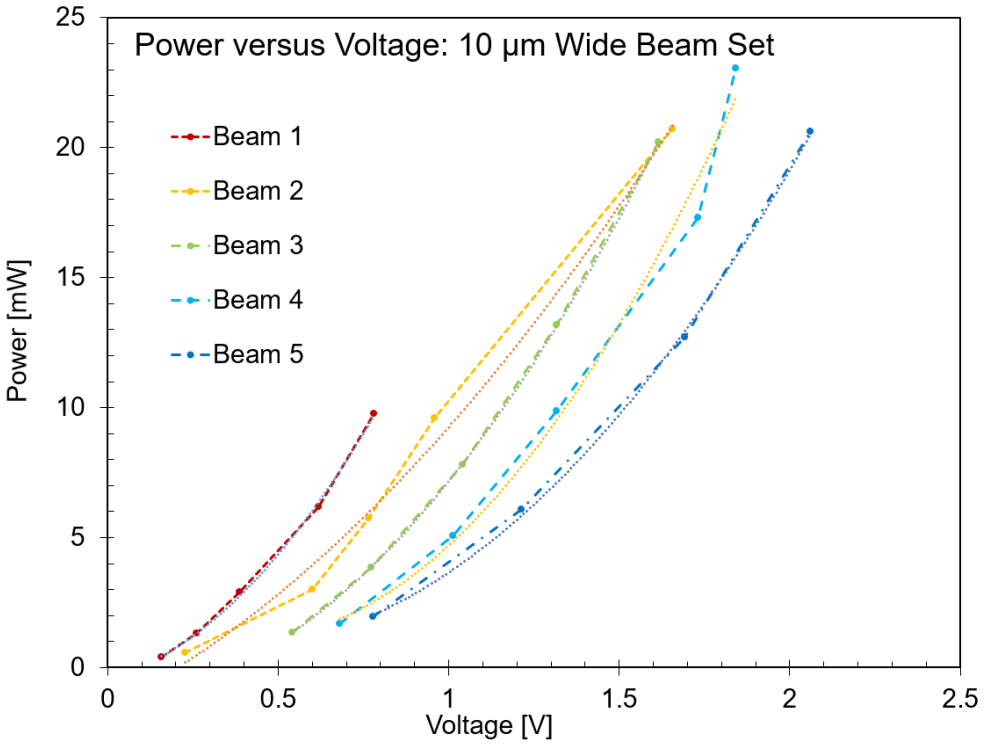

Figure 57 measured power vs. voltage for the 10 µm wide beam set

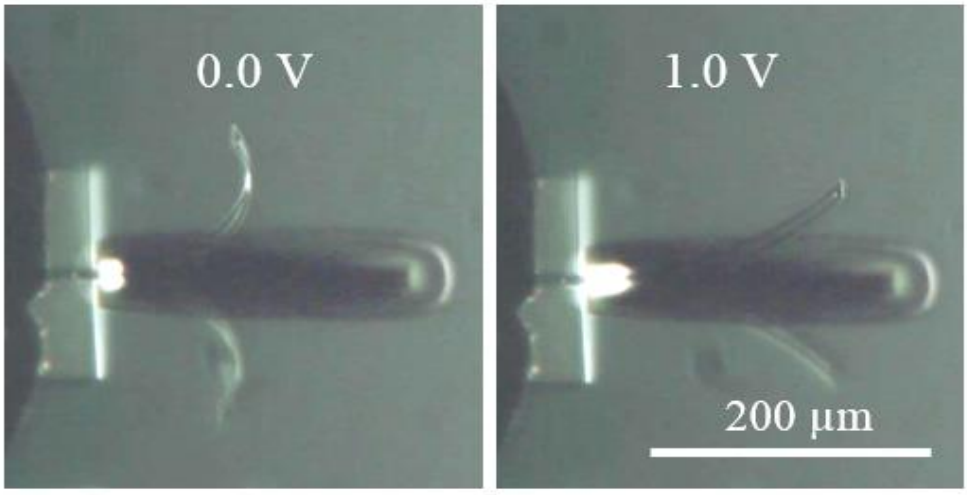

Figure 58. NiTi SMA Joule heater device at 0 V and actuated with 1.0 V.

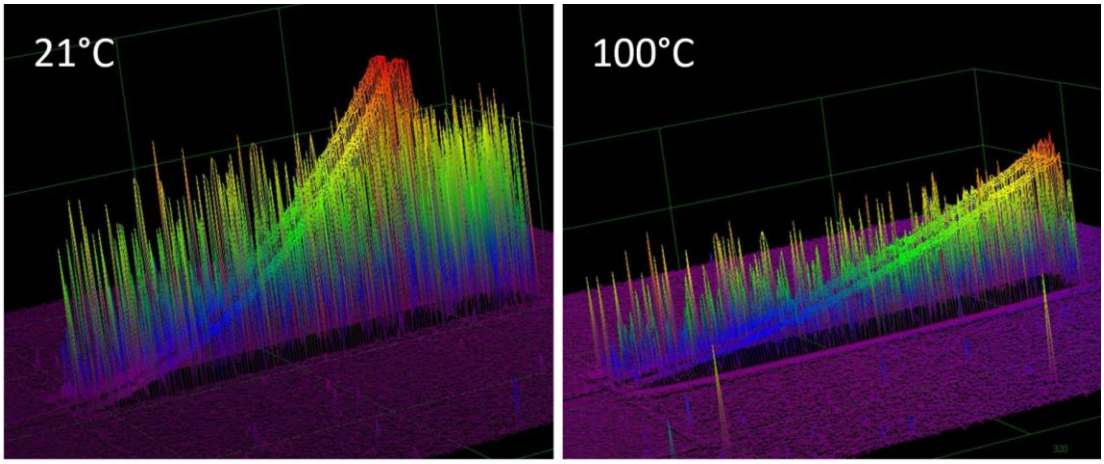

Figure 59. Optical profilometer measurement of SU-8 on NiTi SMA beam at room temperature and 100 °C on hotplate.

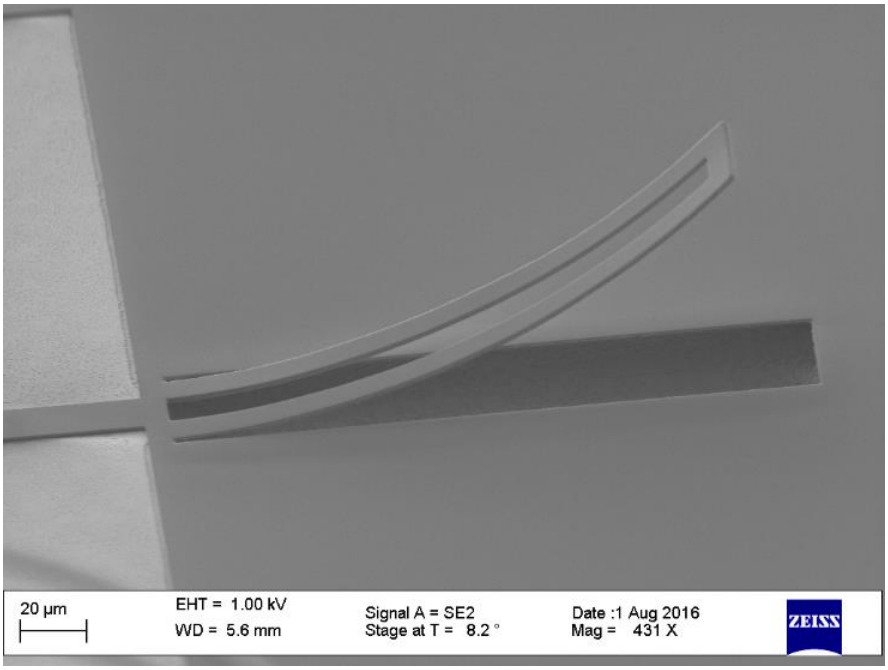

Figure 60. SEM image of released Joule heater SU-8 on NiTi SMA bimorph device.

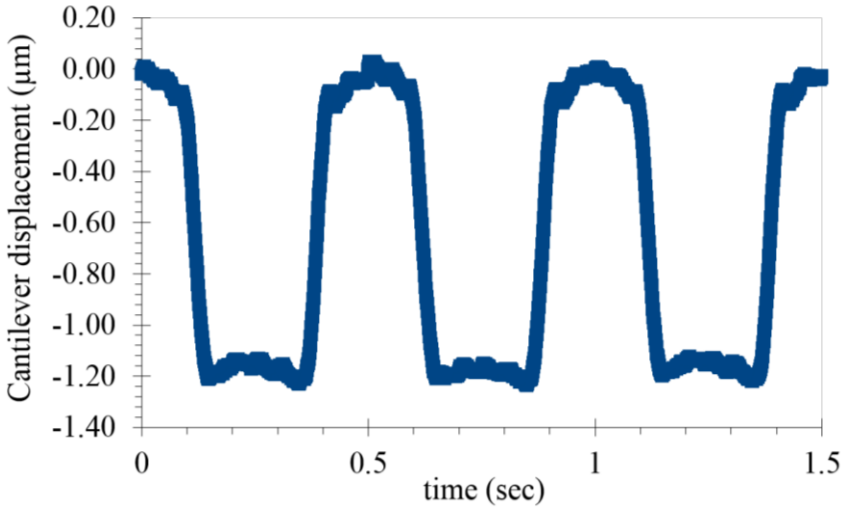

Figure 61. NiTi joule heater cantilever displacement vs. time at 2 Hz with a 1.0 V excitation pulse.

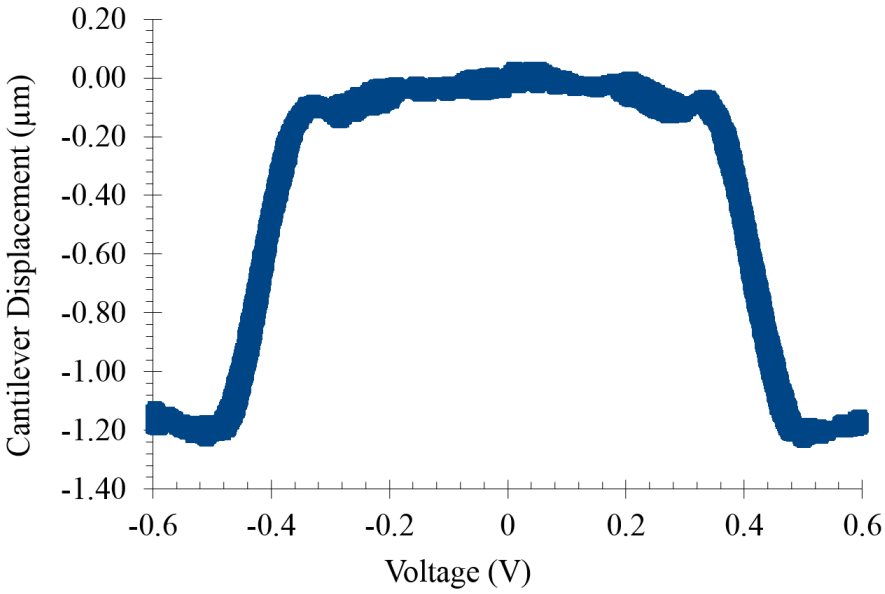

Figure 62. NiTi joule heater cantilever displacement vs. voltage showing a turn-on actuation voltage, V_{act} = 0.5 V.

The device was cycled using pulsed voltage loads, and deflection versus time data recorded at 500 Hz, 1 kHz, and 3 kHz with a 1.0 V excitation, as shown in Figure 63 - Figure 65. Duty cycle

of the pulse was 50%. At higher frequencies, the device did not reach the maximum deflection values (1.2 µm) that were seen in quasi-static actuation. However, these results indicate that partial heating and cooling could be achieved reversibly on these timescales at a reduced deflection amplitude. These reversible deflections were still at least an order of magnitude greater than the deflection due to CTE-mismatch alone. It is important to note, the response is not perfectly symmetric during a cycle due to the fact that the surface-controlled free convective cooling response is slower than that associated with the volumetric joule heating. At 1 kHz, a total displacement of 576 nm was measured after ring down. Ringing occurs at the resonant frequency of the beam, which is measured to be 33.33 kHz, in good agreement with a calculated value of 33 kHz.

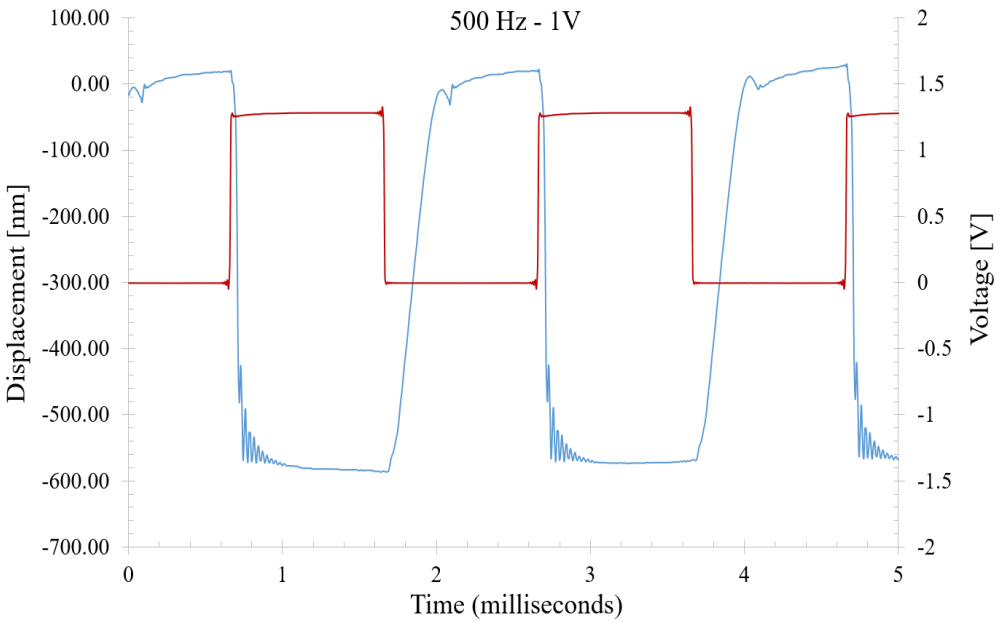

Figure 63 measured device deflection at 500 Hz square wave actuation

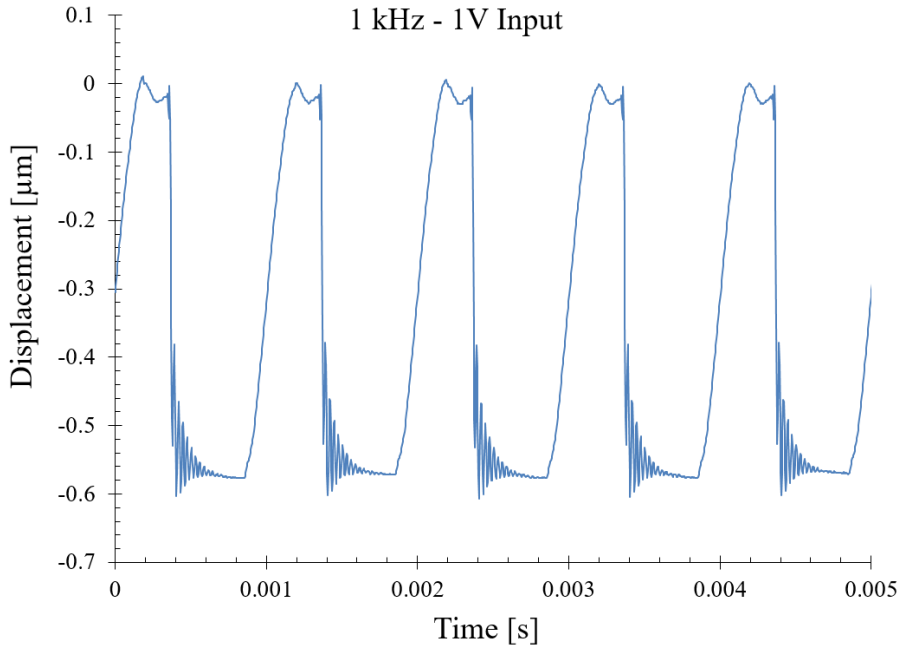

Figure 64 measured device deflection at 1 kHz square wave actuation.

4.5. Results and Discussion

A passive Nickel-SU-8 bimorph actuator was presented in 2010 [185]. Similar to the SMA MEMS actuator presented in this chapter, this device was actuated using a modest 0.5 V input to create joule heating. Since they measured 43 µm displacement on a 830 µm length cantilever, and a constant moment beam has a squared displacement profile, at just 30 µm length, their device would have only deflected 0.05 µm. Therefore, by using active SMA, compared to Ni coupled with SU-8, this work achieved a 20X increase in displacement (1.2 µm) for the same voltage input.

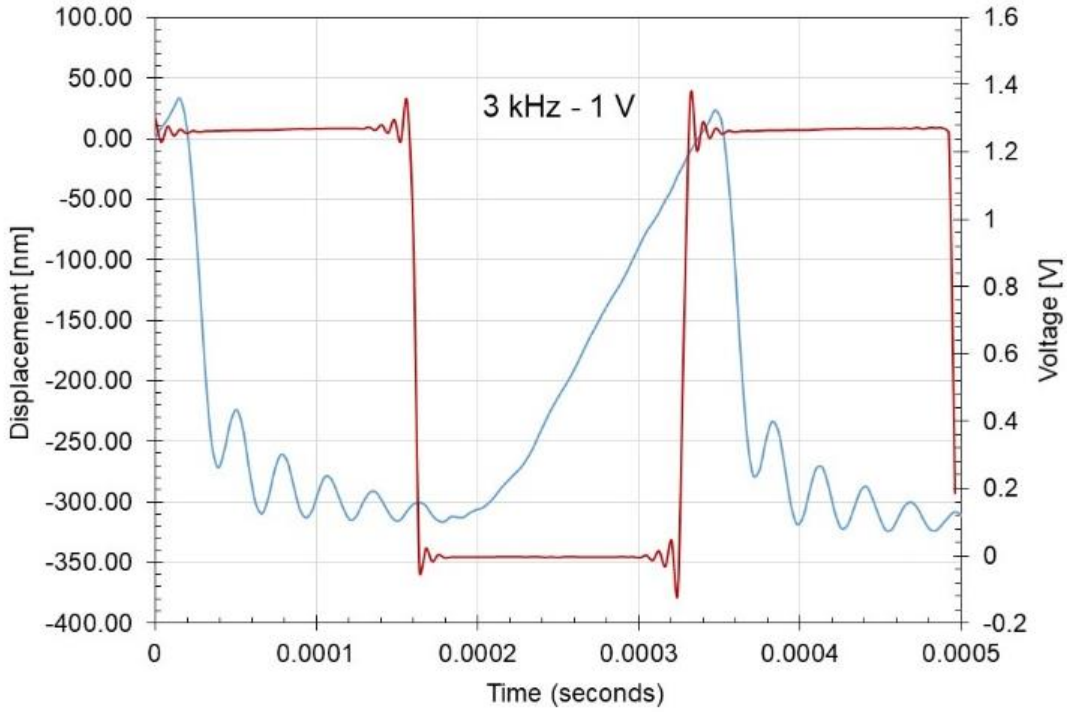

Figure 65 Measured displacement in the SU-8 on NiTi actuator at 3 kHz, 1.0 V pulsed actuation

4.6. Summary

Ultrathin SMA films made from NiTi were sputter deposited on Si wafers using a new, simpler fabrication process that consisted of only one photo step to pattern the NiTi actuators using SU-8. A bending model for thin film bimorph actuators was also used to predict the radius of curvature for device stacks of SU-8 on NiTi after release. There was a clear dependence of radius of curvature on the SU-8 post-bake temperature, which is fundamentally linked to the thermal expansion coefficient mismatch between SU-8 (~52 ppm/K) and NiTi (~8 ppm/K). This work has also shown the dependence of curvature radius and deflection resulting from phase-change on the relative thickness of the SU-8 and NiTi film stacks.

When heated on a hotplate, the actuator devices phase change and actuate into a flatter position, a process that is reversible once the device cools below a critical phase change temperature. However, the thermal mass of the hotplate makes the response time very slow.

Therefore, by using joule heating, this effort determined it was possibly to actuate the devices much more rapidly with a turn on voltage as low as 0.5 V, indicating that small volume SMA actuator can have very low actuation thresholds. A corresponding maximum deflection of 1.2 μm was measured for low a frequency (2 Hz) response. The actuators were able to cycle up to 3 kHz, however, the devices exhibited reduced deflections due to reduced thermal changes induced by the joule heating. Since the surface-controlled free convective cooling is much slower than the volumetric joule heating, it should be possible to recover this deformation via forced convection, and to even achieve higher actuation frequencies.

In the following chapter, the design, fabrication, and actuation of a micromirror array device based on the sputtered shape memory alloy thin films developed in the previous chapters is reported. This demonstration is the first ever reported micromirror array fabricated and actuated from shape memory alloy.

Chapter 5: Fabrication of the NiTi SMA MEMS Optical Micro Mirror Array

5.1. Introduction

MEMS micromirrors have seen commercial successes in beam steering, LiDAR, and projection technology. MEMS micromirrors [148, 186, 187] have been successfully developed and actuated with electrostatic and VO_2 based actuation, but never before with shape memory alloy. SMA could impart some extremely large deflections not possible based on these other actuation methods at MEMS scale. This chapter seeks to build upon the developments presented in chapters 2-4, and fashion a micromirror array based on SMA actuator. A novel actuator design taking advantaged of nested segments of bent-rigid-bent beams enabled a larger degree of curling in the released SMA micromirror.

5.2. Fabrication and Characterization

In order to build the SMA optical mirror arrays (OMA) previous experimental developments related to the SMA processing in the previous chapters were utilized. Information about how to control the curvature radius (using bias stress films like Pt or SU-8), combined with established SMA sputtering recipes enabled the fabrication of preliminary SMA micro-mirror arrays. SMA film on a Pt device wafer with good hysteresis curve (stress-temperature loop) served as the starting point for the SMA MEMS micromirror fabrications. Figure 66 shows two SMA wafers that were fabricated for the preliminary SMA mirror fabrication runs. Liftoff patterning alignment markers on the wafer was enabled by using 5214 negative tone resist (image reversal) and a Cr / Pt alignment marker evaporation (10 nm / 100 nm) step. In a subsequent processing step, 5214 positive tone resist was patterned to ion mill through the NiTi/Pt bi-layer film stack to

define the square mirror element and the actuator arms. The relatively thick NiTi was used for the rigid beam segments and the shutter element as it is relatively flat and highly reflective as a "mirror". The NiTi/Pt was used as a "bending" portion of the actuator. A final device release was performed using XeF_2 etch developed in previous chapters for the SMA MEMS cantilever. Generally, longer etches were performed on the SMA mirror here (500 – 1,000 cycles XeF_2) because the device would drop below the wafer plane during release. After device release, SEM inspection was performed, in addition to hotplate actuation under confocal microscope and laser actuation under microscope.

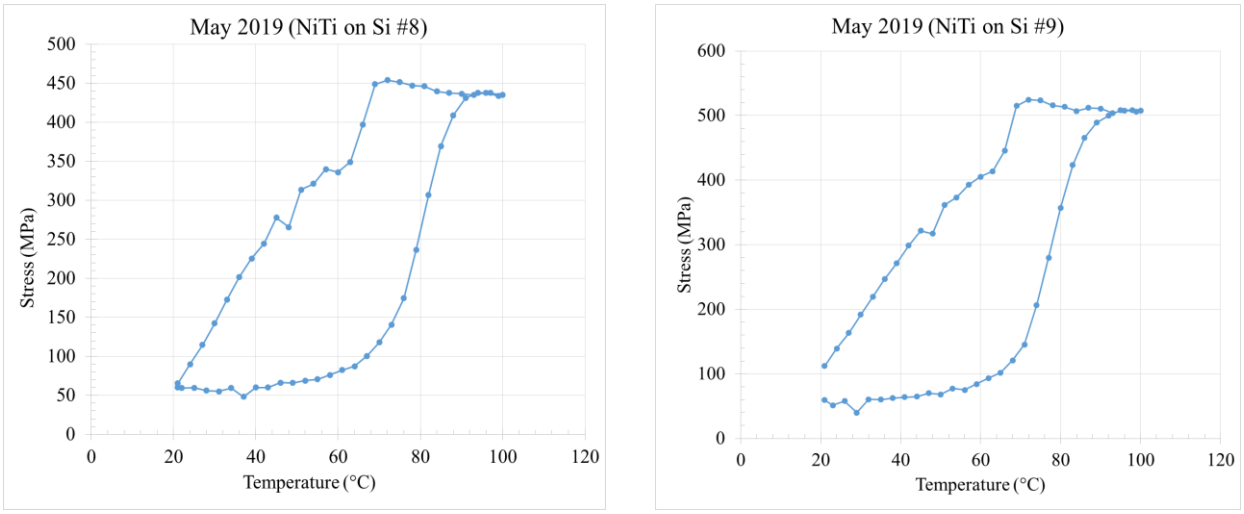

Figure 66. Stress-temperature loops for NiTi SMA micromirror wafer fabrications.

Regarding the operational concept of the mirror array, Figure 67 shows a schematic top-down view of a micromirror array in the 'open' configuration. In other words, the SMA actuator beams would be curled with a specific curvature radius such that the rigid mirrors would be vertically oriented. This configuration would maximize incident light propagation through the open windows. Figure 68 shows the micromirror array once the SMA actuator has been thermally activated. The flat mirror plates would assume a flat orientation and transmitted light would be

minimized. This design would serve as a basis for an optical modulator or beam steering configuration, on-chip.

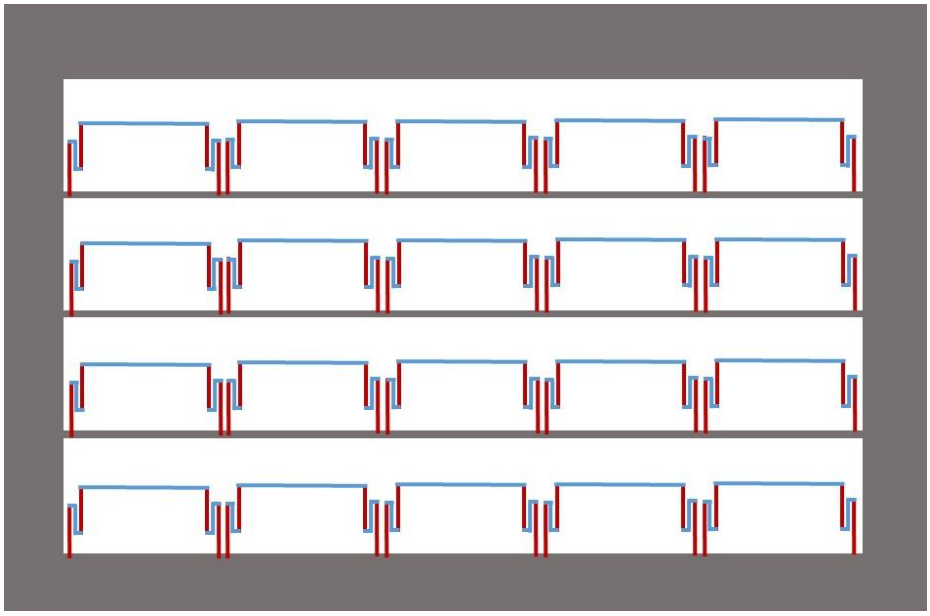

Figure 67 SMA Shutter or "mirror" array in the cold, open position.

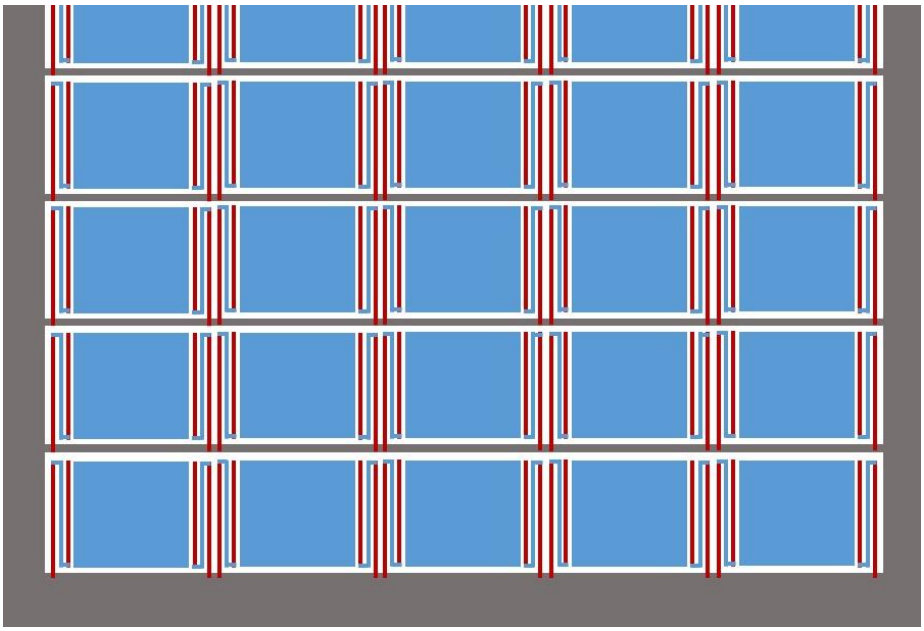

Figure 68. SMA Shutter array in the "hot" closed configuration.

5.3. Characterization and Device Testing of SMA Mirror Actuation

SEM inspection was a first step to inspect the fabrication and release of the MEMS mirror. Figure 69 shows a released SMA micro-mirror. As expected from efforts in previous chapters, residual stresses build up during fabrication, and cause the cantilevers to curl upwards upon release. In this design, the actuator arm is comprised of two bending segments connected by a rigid segment. This results in a more pronounced beam curvature and more deflection in the mirror. *Figure 70* shows a closer look at the alternating bent-rigid-bent SMA actuator beam. This concept is referred to as nested hinge design.

A LEXT microscope integrated with a hot plate was used to characterize the mirror. A three-dimensional scan was recorded at room temperature and at 80 °C. In a LEXT confocal microscope image, the shutter dropped ~17 µm below the substrate upon release. Heating on the hotplate showed significant amounts of actuation of the shutter, presumably due to the SME. The top of the shutter translated through a tip deflection of maximum 17 µm at room temperature, down to ~ -5 µm upon heating to 80 °C, accounting for a translation of 23 µm displacement. More importantly, the angular change in mirror angle for the flat mirror plate went from + 23.3 degrees, through flat (0 degrees), to a maximum tilt of – 6.6 degrees, corresponding to a total tilt angle change of 29.9 degrees. Future iterations should seek to optimize the mirror to operate between a starting vertical orientation, and a flat position when actuated (a 90° rotation). This would facilitation beam steering on-chip as mirrors could be turned on or off to route optical signals through various waveguides or fiber optic cables.

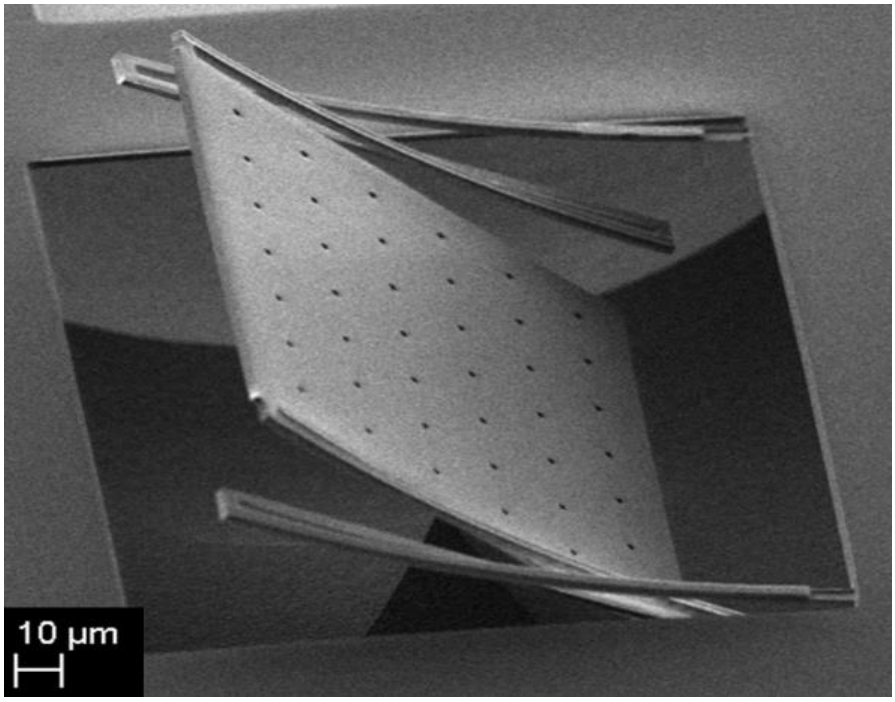

Figure 69. SEM of released NiTi SMA optical mirrors (single device).

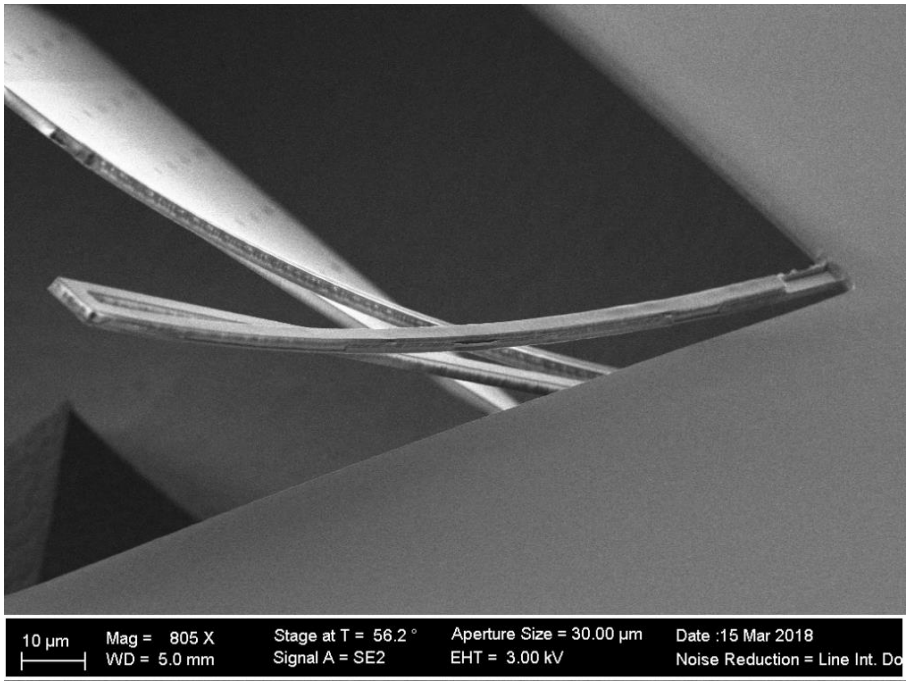

Figure 70. SEM zoomed in look at the nested hinge actuator concept. Easily distinguishable is the bent segment, rigid segment, and bent segment, resulting in increased tip angle.

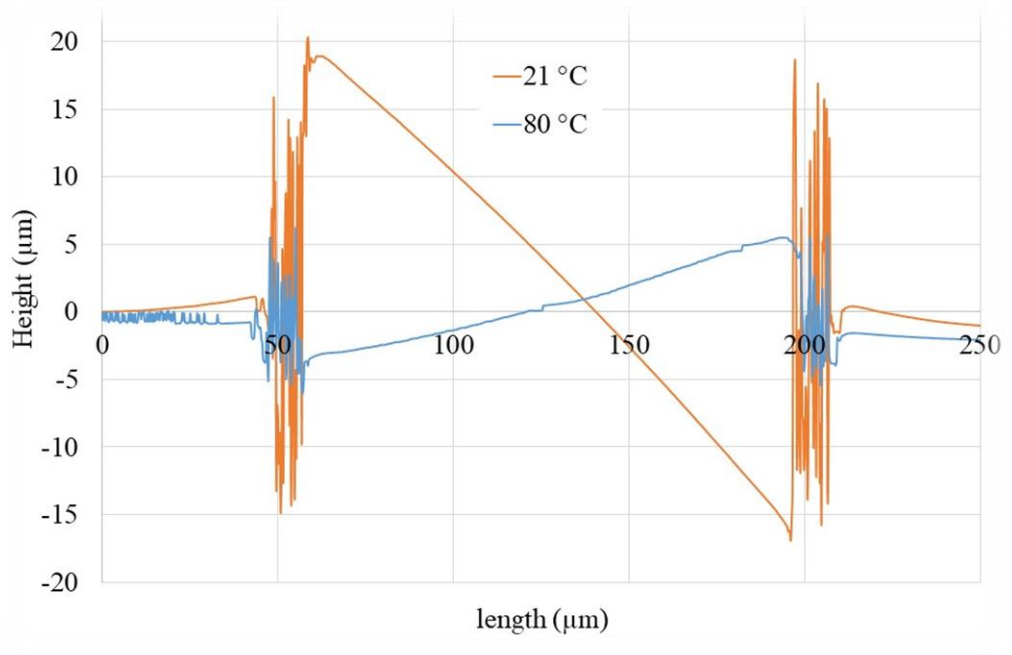

Figure 71. Measured deflection change of the shutter at room temperature and 80 °C corresponding to a thermally actuated pixel moving through 29.9 degrees of rotation.

5.4. Summary

Micromirrors offer a promising solution for future optical modulation, beam steering, and LiDAR applications. Existing MEMS mirrors are usually based on electrostatic actuation such as those commercially found in digital micromirror devices such as projectors. These devices are extremely reliable, but usually are limited to maximum tip/tilt delfection no more than 12-17 µm. This allows fast actuation, but limits the degree to which light can be modulated or steered. This chapter presented a novel design based on large deflection SMA mirrors, where prelimanry demonstration showed a deflection approaching 30 degrees. Combined with work in Chapters 4 and 5, the SMA micromirror presented here could be actuated with laser-irradiation and joule-heating, which was shown to be fast (up to 3 kHz), and consuming low power (5-15 mW).

Chapter 6: Summary and Conclusions

6.1. Conclusion

NiTi SMA has several appealing characteristics including the highest energy densities for actuation at MEMS scale. Existing limitations relating to NiTi abound in terms of processing and MEMS devices. From the processing side, it is difficult for nanoscale thickness SMA to exhibit reversible shape changes due to several constraints related to grain size, film thickness. Additionally, high temperature processing to crystallize or shape-set the NiTi prohibits integration with CMOS of soft polymeric materials. In this dissertation, reversible phase-change in nanoscale SMA films deposited onto Ru and Pt seed layers at lower processing temperatures compatible with CMOS and soft polymer materials is demonstrated. Additionally, the high frequency actuation of SMA MEMS is characterized using laser Doppler Vibrometry (LDV) and pulsed electrical currents to joule heat the NiTi. Actuation frequency is measured up to 3 kHz, and at low power levels, making SMA actuators suitable for power constrained environments (i.e. on chip). As a final preliminary demonstration, a first of its kind SMA MEMS micromirror is fabricated and actuated over 29.9 degrees of rotation, significantly more than other historical MEMS micromirror technologies based on electro-static actuation. During the completion of this dissertation, several scientific and technical contributions were made, and discussed in greater detail in the following section.

6.2. Scientific and Technical Contributions

In one publication, green laser actuation of shape memory MEMS bimorph actuators was characterized after a thorough characterization of intricate relationships between recovery stress and degree of unfolding of SMA MEMS bilayer actuators [168]. Here, it was demonstrated that

NiTi bimorph cantilever could be actuated in under 100 ms, with as little as 2 W/cm^2. In another paper the high cycle frequency of actuation and electrical characterization of SMA MEMS device to include (resistance, current, and power requirements) was investigated [183]. Here, is was demonstrated that NiTi bimorph resistor actuators could be actuated with as little as 0.5 V, requiring just 5-15 mW of power, and at rates up to 3,000 times per second due to the small volume and rapid heat transfer facilitated by large surface to volume ratios. In another paper, the shape memory effects of NiTi grown on a ruthenium (Ru) seed layer was characterized [164], pushing the limits in both SMA film thickness and lowered deposition temperatures.

By lowering the deposition temperatures and still maintaining shape memory effects, the feasibility of integrating NiTi SMA directly onto platforms that would otherwise be excluded due to normal SMA crystallization temperatures above >500 °C was demonstrated. Examples of additional materials would include polyimide, SU-8, certain solder materials, and standard CMOS. This means NiTi could be integrated into microelectronics even after a solder joints have been formed, without reflow. In this dissertation, shape memory effects in thin films deposited at temperatures as low as 325 °C on Ru seed layer, and as thin as 120 nm in thickness were confirmed. At 325°C, shape memory microactuators could be directly deposited onto or integrated onto soft materials like polyimide, SU-8, and some more standard electronic components. Another benefit of lowered crystallization and deposition temperatures is that the thermal failure in microelectronic components due to thermal-expansion mismatch (CTE) would be less severe.

Additionally, the fundamental developments in this work have facilitated the further hierarchical integrations of nanoscale NiTi SMA with nanoscale 3D printed polymers (additive manufacturing). [188, 189]. Below is list of the main scientific and technical contributions enabled in this dissertation.

1. Reduced radius of curvature for NiTi on Pt bimorph actuators. These actuators can thermally cycle between curled radius of 1.2 mm and flat states for ~ 1.2 µm thick NiTi on 200 nm thick Pt. We report a 5.4X reduction on curvature radius for 600 nm NiTi on 20 nm Pt, and achieve reversible shape memory effects between curled and flat positions. This has never before been demonstrated by any other research groups, which have typically been limited due to combinations of thicker NiTi and thick Si cantilevers. (Chapter 3)
2. Reversible shape memory properties in some of the thinnest and "coldest" deposition conditions reported in the literature have been shown to enable tighter curvature radius and process compatibility with soft materials like polymers. (Chapter 2)
3. Fundamental studies were performed to probe the crystallization of nanoscale NiTi SMA under various annealing conditions to arrive at best practices to produce thin films of NiTi SMA with large amounts of recovery stress, capable of phase-transformation (Chapter 2).
4. Demonstrated crystallization of 400 nm NiTi on polyimide at temperatures as low at 400°C, and crystallization of ultra-thin NiTi (120 nm) at temperatures as low as 325°C on a Ru seed layer. Reversible shape memory effects were characterized in these films. (Chapter 2)
5. NiTi actuators performance under laser irradiation was demonstrated at low fluence. A pulsed laser at fast frequencies showed unprecedented reversible range of motion in NiTi cantilevers and "micro mirrors" or micro joule-heaters. (Chapter 3 and 4)
6. Best-practices MEMS processing and NiTi patterning (etch, release) methods were developed (Chapter 3)
7. Increased the frequency with which NiTi SMA Actuators can be cycled, measuring device actuation response up to 3 kHz. (Chapter 4)

8. Significantly lowered the amount of power required to actuate SMA MEMS device (as low as 0.5 V, or 5-10 mW for joule heaters), and 2 W/cm^2 using a 440 mW green laser. (Chapter 3-4)
9. Developed MEMS fabrication process for SMA optical mirror device arrays. The large deflections inherent to SMA MEMS enabled the largest range of motion (ROM) micromirrors (29.9°), compared to traditional concepts based on piezoelectric and electrostatic actuations used in commercial digital micromirror devices (DMD). (Chapter 5)

6.3. Future Work

Several avenues of opportunity exist for further exploration of NiTi SMAs and MEMS micromirror actuators related to and building upon this dissertation.

High Cycle Fatigue NiTi-based alloys:

In order for NiTi to become reliable in high cycle applications like that required in the human body and solid state cooling (elastocalorics cooling), NiTi or other SMA will need to undergo reversible martensitic transformation many thousands or millions of times. Certain work has already been done in these areas [190], but certainly there is room for additional works and fabrication and testing of devices based on these high cycle operations. An extension of these efforts with value to the community would be to fabricate MEMS actuators from the identified NiTiCu alloy compositions.

NiTi on Ru actuator characterizations

In this dissertation, the ground work was laid to confirm crystallization and measured shape memory properties on nanoscale thickness NiTi films on substrate. Future work could consider

MEMS patterning and actuator testing of these films to enable even faster, or lower power actuators.

Thermal property measurements of NiTi films with various deposition conditions and grain size.

As reported in [56], solution anneals can drastically influence the grain size (GS) of bulk NiTi, which is positively correlated to significant enhancements in thermal conductivity as measured by FDTR and TDTR methods. Because at micro and nanoscale, thermal properties will significantly affect the heat transfer, and allow for more accurate thermo-mechanical modeling in MEMS actuators, a suitable study of these properties (incl. thermal conductivity, and heat capacity) should be of great interest.

MEMS micromirrors and adaptive optics.

MEMS micromirrors [148, 186, 187] have been successfully developed and actuated with electrostatic and VO_2 based actuation, but never with shape memory alloy. SME could impart some extremely large deflections not possible based on these other actuation methods at MEMS scale.

Integrating 3D printing with SMA MEMS:

The DARPA SHRIMP program (Short Range Independent Microrobotic Platforms), which spans from approx. 2018 - 2022 is focused in-part on the development of novel micro actuation technologies to propel futuristic micro-robots has spurred some early work in this field. Nanoscribe 3D printer was used in conjunction with sputtered NiTi SMA MEMS processing to create novel actuators with impressive figures of merit including low power draw (nominal pulsed actuation cycle is 3.7 V, 35 mA, and 0.97 mJ, and a 7.5 ms pulse width), large strokes (85 μm for 415 μm beam), high cycle actuation (> 5,000 cycles, and most importantly, large force-displacement

product ($1.2*10^{-7}$ N-m) [188, 189]. These NiTi SMA actuators are incredibly lightweight ($1.27*10^{-5}$ g), occupy extremely small volumes ($1.04*10^{-5}$ cm^3), and require only 3.7 V to actuate. A free cantilever displacement of 85 μm, and blocking force of 1.6 mN was achieved with a NiTi / IPS composite beam of 415 μm length for an impressive ratio of length to displacement.

Microelectronics transient cooling applications:

Bulk NiTi, including additive manufacturing has been shown as a promising candidate for pulsed power cooling due to large latent heat of transformation associated with the reversible martensitic phase change [55, 56]. A natural scaling down of the SMA into MEMS and microelectronics platforms would potentially revolutionize the microelectronics industry by allowing chips and microprocessors to run harder and faster without overheating. This would be expected to benefit edge computing.

Chapter 7: Publications

The contributions of this dissertation were primarily captured in the following peer-reviewed journals, conference proceedings, book chapters, and invention disclosure.

7.1. Journal Papers

I. *Controlling shape memory effects in NiTi thin films grown on Ru seed layer* Sensors and Actuators A: Physical Volume 294, 1 August 2019, Pages 133-139 Kenneth Ainslie, Cory R. Knick, Gabriel Smith, Jianheng Lia, Charles Troxel, Apurva Mehta, Roopali Kukreja

II. *High-frequency, low-power, electrically actuated SMA MEMS bimorph actuators* Cory R. Knick, Hugh A. Bruck, Christopher J. Morris, Gabe Smith, Journal of Micromechanics and Microengineering (JMM), Vol 29, 7 (2019)

III. *Low Power Laser Actuation of Sputter-Deposited NiTi Shape Memory Alloy (SMA) MEMS Thermal Bimorph Actuators* Cory. R. Knick, Gabriel L. Smith, Hugh A. Bruck, and Christopher. J. Morris Sensors & Actuators A: Physical, Vol 291, pp. 48-57 (2019)

IV. *Combining Micro Fabrication and Additive Manufacturing for Microrobotic Mechanisms Camilo Velez, Dinesh Patel, Sukjun Kim, Mahnoush Babaei, Cory R. Knick, Gabriel Smith, and Sarah Bergbreiter, special proceedings JMEMS (2020)*

7.2. Conference Proceedings Papers

I. *Rapid Prototyping of Microactuators by Integrating 3D Printed Polymeric Structures With NiTi Thin Film*, 33rd IEEE International Conference on Micro Electromechanical Systems (MEMS). pp 893-896, 2020 Camilo Velez, Sukjun Kim, Dinesh Patel, Mahnoush Babaei, Cory R. Knick, Gabriel Smith, and Sarah Bergbreiter (2020)

II. *Investigating Nanoscale Behavior of SMA films deposited onto soft substrates*, Cory R. Knick, Christopher J. Morris, Gabe Smith, Dan Cole, Proceedings of ASME Smart materials, adaptive structures, intelligent systems, SMASIS (2017)

III. *Material and Process Development of Thin Film Shape Memory Alloy for MEMS Actuators*, Cory R. Knick, Christopher J. Morris, Proceedings of Smart Materials, Adaptive Structures, and Intelligent Systems SMASIS (2016)

IV. *Characterization of Sputtered Nickel-Titanium Shape Memory Alloy and Microfabricated Thermal Actuators*, Cory R. Knick, Christopher J. Morris, Proc. of IEEE MEMS (2016)

V. *Co-sputter Development of Thin Film Shape Memory Alloy of MEMS Actuator*, Cory R. Knick, Christopher J. Morris, Proceedings of Smart Materials, Adaptive Structures, and Intelligent Systems SMASIS (2015)

VI. *Development of thin-film shape memory alloy for reversible, thermally actuated MEMS devices*, Cory R. Knick, Christopher J. Morris, MRS Fall (2014) Proceedings, Boston, MA

7.3. Invention Disclosures / Patents

I. Phase-change microshutter arrays and method of manufacture

7.4. Book Chapters

II. Fabrication and Characterization of Nanoscale Shape Memory Alloy MEMS "Advanced Functional Materials (2020)"

III. Optimization of MEMS actuator driven by shape memory alloy thin film phase-change "Advanced Functional Materials (2020)"

References

[1] K. Otsuka and X. Ren, "Physical metallurgy of Ti–Ni-based shape memory alloys," *Progress in Materials Science,* vol. 50, no. 5, pp. 511-678, 2005, doi: 10.1016/j.pmatsci.2004.10.001.

[2] J. Walker, K. Gabriel, and M. Mehregany, "Thin-film processing of TiNi shape memory alloy," *Sensors and Actuators A: Physical,* vol. 21, no. 1-3, 1990.

[3] P. Krulevitch, A. P. Lee, P. B. Ramsey, J. C. Trevino, J. Hamilton, and M. A. Northrup, "Thin film shape memory alloy microactuators," *Journal of Microelectromechanical Systems,* vol. 5, no. 4, 1996.

[4] B.-K. L. Chen-Luen Shih, Harold Kahn, Stephen M. Phillips, and Arthur H. Heuer, "A robust co-sputtering fabrication procedure for TiNi shape memory alloys for MEMS," *Journal of Microelectromechanical Systems,* vol. 10, no. 1, p. 69, 2001.

[5] K. R. C. Gisser, J. D. Busch, A. D. Johnson, and A. B. Ellis, "Oriented nickel-titanium shape memory alloy films prepared by annealing during deposition," *Applied Physics Letters,* vol. 61, no. 14, pp. 1632-1634, 1992, doi: 10.1063/1.108434.

[6] D. G. Li Hou, "Transformational superelasticity in sputtered titanium-nickel thin films," *Scripta Materialia,* vol. 33, no. 6, pp. 989-995, 1995.

[7] Y. C. Shu and K. Bhattacharya, "The influence of texture on shape-memory effect in polycrystals," *Acta Mater.,* vol. 46, no. 15, p. 5457, 1998.

[8] J. D. Busch, A. D. Johnson, C. H. Lee, and D. A. Stevenson, "Shape-memory properties in Ni-Ti sputter-deposited film," *Journal of Applied Physics,* vol. 68, no. 12, pp. 6224-6228, 1990, doi: 10.1063/1.346914.

[9] K. P. M. Ken K. Ho, Gregory P. Carman, "Examination of the sputtering profile of NiTi under target heating conditions," *Thin Solid Films,* vol. 413, pp. 1-7, 2002.

[10] Y. Fu, W. Huang, H. Du, X. Huang, J. Tan, and X. Gao, "Characterization of TiNi shape-memory alloy thin films for MEMS," *Surface and Coatings Technology,* vol. 145, pp. 107-112, 2001.

[11] Y. Q. Fu *et al.*, "On the lower thickness boundary of sputtered TiNi films for shape memory application," *Thin Solid Films,* vol. 515, no. 1, pp. 80-86, 2006, doi: 10.1016/j.tsf.2005.12.039.

[12] Y. Fu and H. Du, "Relaxation and recovery of stress during martensite transformation for sputtered SMA TiNi film," *Surface and Coatings Technology,* vol. 153, pp. 100–105, 2002.

[13] V. G. Kotnur, F. D. Tichelaar, W. T. Fu, J. T. M. De Hosson, and G. C. A. M. Janssen, "Shape memory NiTi thin films deposited on polyimide at low temperature," *Surface and Coatings Technology,* vol. 258, pp. 1145-1151, 2014, doi: 10.1016/j.surfcoat.2014.07.018.

[14] Y. Fu, H. Du, and S. Zhang, "Sputtering deposited TiNi films: relationship among processing, stress evolution and phase transformation behaviors," *Surface and Coatings Technology,* vol. 167, no. 2-3, pp. 120-128, 2003, doi: 10.1016/s0257-8972(02)00896-4.

[15] Y. Fu, H. Du, S. Zhang, and Y. Gu, "Stress and surface morphology of TiNiCu thin films: effect of annealing temperature," *Surface and Coatings Technology,* vol. 198, no. 1-3, pp. 389-394, 2005, doi: 10.1016/j.surfcoat.2004.10.107.

[16] D. S. G. a. J. Zhang, "Stress in Sputtered Films of Near-Equiatomic TiNiX on (100) Si: Intrinsic and Extrinsic Stresses and Their Modification by Thermally Activated Mechanisms," *phys. stat. sol.,* vol. 186, no. 1, pp. 17-39, 2001.

[17] E. H. Anderson, D. D. Shin, K. P. Mohanchandra, D. G. Lee, and G. P. Carman, "Miniature actuator using thin-film shape-memory alloy," vol. 5054, p. 118, 2003, doi: 10.1117/12.483732.
[18] D. C. John Gill, Leslie Momoda, Greg Carman, "Manufacturing issues of thin film NiTi microwrapper," *Sensors and Actuators A: Physical*, vol. 93, pp. 148-156, 2001.
[19] S. Sanjabi, Y. Z. Cao, S. K. Sadrnezhaad, and Z. H. Barber, "Binary and ternary NiTi-based shape memory films deposited by simultaneous sputter deposition from elemental targets," *Journal of Vacuum Science & Technology A: Vacuum, Surfaces, and Films*, vol. 23, no. 5, pp. 1425-1429, 2005, doi: 10.1116/1.2011404.
[20] S. Sanjabi and Z. H. Barber, "The effect of film composition on the structure and mechanical properties of NiTi shape memory thin films," *Surface and Coatings Technology*, vol. 204, no. 8, pp. 1299-1304, 2010, doi: 10.1016/j.surfcoat.2009.10.013.
[21] B. Naveen Kumar Reddy and N. K. Udayashankar, "Influence of annealing temperature on the structural, morphological, mechanical and surface properties of near equiatomic NiTi thin films," *Vacuum*, vol. 142, pp. 186-196, 2017, doi: 10.1016/j.vacuum.2017.05.021.
[22] A. Ishida, "Mechanical properties of Ti–Ni shape memory thin films formed by sputtering," *Materials Science and Engineering: A*, vol. 273–275, pp. 754–757, 1999.
[23] A. Ishida, "Effects of Composition and Annealing on Shape Memory Behavior of Ti-Rich Ti-Ni Thin Films Formed by Sputtering," *Materials Transactions*, vol. 42, no. 6, pp. 1060-1067, 2001.
[24] A. Ishida and M. Sato, "Thickness effect on shape memory behavior of Ti-50.0at.%Ni thin film," *Acta Materialia*, vol. 51, no. 18, pp. 5571-5578, 2003, doi: 10.1016/s1359-6454(03)00420-8.
[25] H. D. a. Y. Fu, "Characterization and MEMS application of sputtered TiNi shape memory alloy thin films," *Micromachining and Microfabrication Process Technology and Devices*, vol. 4602, 2001.
[26] Y. Fu, X. Huang, H. Du, and Y. Liii, "RF magnetron sputtered crystalline TiNiCu shape memory alloy thin film," *Smart Structures and Materials*, vol. 4333, 2001.
[27] Y. Q. Fu *et al.*, "Evolution of surface morphology in TiNiCu shape memory thin films," *Applied Physics Letters*, vol. 89, no. 17, p. 171922, 2006, doi: 10.1063/1.2361275.
[28] L. Zhang, C. Xie, and J. Wu, "Effect of annealing temperature on surface morphology and mechanical properties of sputter-deposited Ti–Ni thin films," *Journal of Alloys and Compounds*, vol. 427, no. 1-2, pp. 238-243, 2007, doi: 10.1016/j.jallcom.2006.02.067.
[29] H. Inoue, N. Miwa, and N. Inakazu, "Texture and shape memory strain in TiNi alloy sheets," *Acta Mater.*, vol. 44, no. 12, pp. 4825-4834, 1996.
[30] M. Sato, A. Ishida, and S. Miyazaki, "Two-way shape memory effect of sputter-deposited thin films of Ti 51.3 at% Ni," *Thin Solid Films*, vol. 315, pp. 305–309, 1998.
[31] X. Wang, "Crystallization and Martensitic Transformation Behavior of NiTi Shape Memory Alloy Thin Films," PhD, School of Engineering and Applied Sciences, Harvard, 2007.
[32] Y. S. Liu, D. Xu, B. H. Jiang, Z. Y. Yuan, and P. V. Houtte, "The effect of crystallizing procedure on microstructure and characteristics of sputter-deposited TiNi shape memory thin films," *Journal of Micromechanics and Microengineering*, vol. 15, no. 3, pp. 575-579, 2005, doi: 10.1088/0960-1317/15/3/019.

[33] Y. Liu and X. Huang, "Substrate-induced stress and transformation characteristics of a deposited Ti–Ni–Cu thin film," *Philosophical Magazine,* vol. 84, no. 19, pp. 1919-1936, 2004, doi: 10.1080/14786430410004500.
[34] G. Satoh, A. Birnbaum, and Y. L. Yao, "Annealing Effect on the Shape Memory Properties of Amorphous NiTi Thin Films," *Journal of Manufacturing Science and Engineering,* vol. 132, no. 5, p. 051004, 2010, doi: 10.1115/1.4002189.
[35] P. Surbled, C. Clerc, B. L. Pioufle, M. Atakaa, and H. Fujitaa, "Effect of the composition and thermal annealing on the transformation temperatures of sputtered TiNi shape memory alloy thin films," *Thin Solid Films,* vol. 401, pp. 52–59, 2001.
[36] "Martensitic transformations in Ni50Ti50 films."
[37] A. L. ROYTBURD, T. S. KIM, Q. SU, J. SLUTSKER, and M. WUTTIG, "Martensitic transformation in constrained films," *Acta Mater.,* vol. 46, no. 14, pp. 5095-5107, 1998.
[38] S. Z. H. a. M. W. Quanmin Su, "Martensitic transformations in Ni50Ti50 films," *SPIE,* vol. 2189.
[39] I.-J. KIM, H. NANJO, T. IIJIMA, and T. ABE, "Crystallization Process of TiNi Thin Films Sputtered at Elevated Temperatures on Pt/Si Oxide/Si and Si Oxide/Si Substrates," *Japan Journal of Applied Physics,* vol. 39, pp. 568–571, 2000.
[40] B.-K. Lai, H. Kahn, S. M. Phillips, Z. Akase, and A. H. Heuer, "Quantitative phase transformation behavior in TiNi shape memory alloy thin films," *Journal of Materials Research,* vol. 19, no. 10, pp. 2822-2833, 2004, doi: 10.1557/jmr.2004.0385.
[41] A. P. L. Peter Krulevitch, Philip B. Ramsey, James C. Trevino, Julie Hamilton, and M. Allen Northp, "Thin film shape memory alloy microactuators," *Journal of Microelectromechanical Systems,* vol. 5, no. 4, pp. 270-282, 1996.
[42] H. Hou, "NANOSCALE NICKEL-TITANIUM SHAPE MEMORY ALLOYS THIN FILMS FABRICATED BY USING BIASED TARGET ION BEAM DEPOSITION," PhD, Engineering Science and Mechanics, Pennsylvania State University, 2015.
[43] R. M. S. Martins *et al.*, "Texture development, microstructure and phase transformation characteristics of sputtered Ni–Ti Shape Memory Alloy films grown on TiN<111>," *Thin Solid Films,* vol. 519, no. 1, pp. 122-128, 2010, doi: 10.1016/j.tsf.2010.07.078.
[44] C. Bechtold, C. Chluba, R. Lima de Miranda, and E. Quandt, "High cyclic stability of the elastocaloric effect in sputtered TiNiCu shape memory films," *Applied Physics Letters,* vol. 101, no. 9, p. 091903, 2012, doi: 10.1063/1.4748307.
[45] A. Ishida, M. Sato, and Z. Y. Gao, "Properties and applications of TiNiCu shape-memory-alloy thin films," *Journal of Alloys and Compounds,* vol. 577, pp. S184-S189, 2013, doi: 10.1016/j.jallcom.2011.12.155.
[46] M.H. Ren, L. Wang, D. Xu, and B. C. Cai, "Sputter-deposited TiNiCu shaped memory alloy thin films," *Materials and Design,* vol. 21, pp. 583-586, 2000.
[47] H. J. Z. a. C. J. Qiu, "A TiNiCu Thin Film Micropump Made by Magnetron Co-Sputtered Method," *Materials Transactions,* vol. 47, no. 3, pp. 532-535, 2006.
[48] A. Isalgue, "Shape memory NiTi thin films deposited at low temperature," *Materials Science and Engineering: A,* vol. 273–275, pp. 717–721, 1999.
[49] V. G. Kotnur, F. D. Tichelaar, and G. C. A. M. Janssen, "Sputter deposited Ni–Ti thin films on polyimide substrate," *Surface and Coatings Technology,* vol. 222, pp. 44-47, 2013, doi: 10.1016/j.surfcoat.2013.01.058.
[50] Y. F. a. H. Du, "TiNi shape memory alloy thin films for microactuator application."

[51] S. K. S. A. Kumar, S. Bysakh, S.V. Kamat and S. Mohan, "Effect of Substrate and Annealing Temperatures on Mechanical Properties of Ti-rich NiTi Films," *J. Mater. Sci. Technol.*, vol. 26, no. 11, pp. 961-966, 2010.

[52] H.-J. Lee and A. G. Ramirez, "Crystallization and phase transformations in amorphous NiTi thin films for microelectromechanical systems," *Applied Physics Letters*, vol. 85, no. 7, pp. 1146-1148, 2004, doi: 10.1063/1.1783011.

[53] S. Momeni, J. Biskupek, and W. Tillmann, "Tailoring microstructure, mechanical and tribological properties of NiTi thin films by controlling in-situ annealing temperature," *Thin Solid Films*, vol. 628, pp. 13-21, 2017, doi: 10.1016/j.tsf.2017.02.052.

[54] W. Tillmann and S. Momeni, "In-situ annealing of NiTi thin films at different temperatures," *Sensors and Actuators A: Physical*, vol. 221, pp. 9-14, 2015, doi: 10.1016/j.sna.2014.10.034.

[55] B. F. D. Darin J. Sharar, Ronald J. Warzoha, Adam A. Wilson, Asher C. Leff, and Brendan M. Hanrahan, "Solid-state thermal energy storage using reversible martensitic transformations," *Applied Physics Letters*, vol. 114, 2019. [Online]. Available: https://doi.org/10.1063/1.5087135.

[56] N. T. V. Ronald J.Warzoha, Brian F. Donovan, Elena Cimpoiasu, Darin J. Sharar, Asher C. Leff, Adam A. Wilson, Andrew N.Smith, "Grain growth-induced thermal property enhancement of NiTi shape memory alloys for elastocaloric refrigeration and thermal energy storage systems," *International Journal of Heat and Mass Transfer*, vol. 154, p. 119760, 2020. [Online]. Available: https://www.sciencedirect.com/science/article/abs/pii/S0017931020304221.

[57] "A Comparative Study of PZT-Based & TiNi- Shape Memory Alloy Based MEMS Microactuators."

[58] S. D. Nijmeh, M. S. Ashhab, and R. F. Khasawneh, "A Comparative Study of PZT-Based & TiNi- Shape Memory Alloy Based MEMS Microactuators," *Jordan Journal of Mechanical and Industrial Engineering*, vol. 7, no. 1, pp. 27-34, 2007.

[59] B. S. Shariat *et al.*, "Functionally graded shape memory alloys: Design, fabrication and experimental evaluation," *Materials & Design*, vol. 124, pp. 225-237, 2017, doi: 10.1016/j.matdes.2017.03.069.

[60] A. AbuZaiter, M. Nafea, A. A. Mohd Faudzi, S. Kazi, and M. S. Mohamed Ali, "Thermomechanical behavior of bulk NiTi shape-memory-alloy microactuators based on bimorph actuation," *Microsystem Technologies*, vol. 22, no. 8, pp. 2125-2131, 2015, doi: 10.1007/s00542-015-2641-1.

[61] F. Lambrecht, C. Lay, I. R. Aseguinolaza, V. Chernenko, and M. Kohl, "NiMnGa/Si Shape Memory Bimorph Nanoactuation," *Shape Memory and Superelasticity*, vol. 2, no. 4, pp. 347-359, 2016, doi: 10.1007/s40830-016-0080-1.

[62] Y. Chen and C. A. Schuh, "Size effects in shape memory alloy microwires," *Acta Materialia*, vol. 59, no. 2, pp. 537-553, 2011, doi: 10.1016/j.actamat.2010.09.057.

[63] T. LEHNERT, S. CREVOISERAT, and R. GOTTHARDT, "Transformation properties and microstructure of sputter-deposited Ni-Ti shape memory alloy thin films," *Journal of Materials Science*, vol. 37, 2002.

[64] H. T. Lee, M. S. Kim, G. Y. Lee, C. S. Kim, and S. H. Ahn, "Shape Memory Alloy (SMA)-Based Microscale Actuators with 60% Deformation Rate and 1.6 kHz Actuation Speed," *Small*, vol. 14, no. 23, p. e1801023, Jun 2018, doi: 10.1002/smll.201801023.

[65] E. Wibowo and C. Y. Kwok, "Fabrication and characterization of sputtered NiTi shape memory thin films," *Journal of Micromechanics and Microengineering*, vol. 16, no. 1, pp. 101-108, 2006, doi: 10.1088/0960-1317/16/1/014.
[66] C. M. Craciunescu, "Actuation in shape memory layer engineered film based architectures," *Surface Engineering*, vol. 26, no. 7, pp. 536-539, 2013, doi: 10.1179/174329409x439014.
[67] C. M. Craciunescu, I. Mihalca, and V. BudAu, "TRIMORPH ACTUATION BASED ON SHAPE MEMORY ALLOYS," *Journal of Optoelectronics and Advanced Materials*, vol. 7, no. 2, pp. 1113-1120, 2005.
[68] C. Craciunescu and A. Ercuta, "Prediction of thermally-controlled actuation for shape memory alloy film-based bimorph cantilevers," *Smart Materials and Structures*, vol. 23, no. 7, p. 075025, 2014, doi: 10.1088/0964-1726/23/7/075025.
[69] A. Ishida, M. Sato, W. Yoshikawa, and O. Tabata, "Bimorph-Type Microactuator using TiNi Shape-Memory Thin Film," *Materials Science Forum*, vol. 394-395, pp. 487-490, 2002, doi: 10.4028/www.scientific.net/MSF.394-395.487.
[70] L. Wang, D. Xu, B. Cai, and X. Cheng, "Control of internal stress in SMA-Si bimorph microactuators," *Micromachining and Microfabrication Process Technology*, vol. 4174, 2000.
[71] E. Wongweerayoot, W. Srituravanich, and A. Pimpin, "Fabrication and Characterization of Nitinol-Copper Shape Memory Alloy Bimorph Actuators," *Journal of Materials Engineering and Performance*, vol. 24, no. 2, pp. 635-643, 2014, doi: 10.1007/s11665-014-1334-8.
[72] S. R. S. S. Pal, X. Zhang, and H. Xie, "Large in-plane displacement microactuators based on electro-thermal bimorphs with folded multiple segments," *Transducers*, 2013.
[73] M. J. Sinclair, "A High Force Low Area MEMS Thermal Actuator," in *Inter Society Conference on Thermal Phenomena*, 2000.
[74] S. Rastjoo, R. Fechner, L. Bumke, M. Kötz, E. Quandt, and M. Kohl, "Development and co-integration of a SMA/Si bimorph nanoactuator for Si photonic circuits," *Microelectronic Engineering*, vol. 225, 2020, doi: 10.1016/j.mee.2020.111257.
[75] I. A. F. Lambrecht, V. Chernenko and M. Kohl, "Integrated SMA-based NEMS actuator for optical switching," in *IEEE 29th International Conference on Micro Electro Mechanical Systems (MEMS)*, Shanghai, China, 2016, pp. 79-82, doi: 10.1109/MEMSYS.2016.7421562.
[76] C. J. M. Kate E. Laflin, Tanziyah Muqeem, and David H. Gracias, "Laser triggered sequential folding of microstructures," *Applied Physics Letters*, vol. 101, 2012, doi: 10.1063/1.4754607

10.1063/1.4754607].
[77] K. Malachowski, M. Jamal, Q. Jin, B. Polat, C. J. Morris, and D. H. Gracias, "Self-folding single cell grippers," *Nano Lett*, vol. 14, no. 7, pp. 4164-70, Jul 9 2014, doi: 10.1021/nl500136a.
[78] D. V. D. Resnik, U. Aljančič, M. Možek, S. Penič, S. Amon,, "Influence of mechanical stress on adhesion properties of DC magnetron sputtered Ti/NiV/Ag layers on n+Si substrate," *Microelectronic Engineering*, vol. 85, no. 7, 2008.
[79] T. G. Leong, C. L. Randall, B. R. Benson, N. Bassik, G. M. Stern, and D. H. Gracias, "Tetherless thermobiochemically actuated microgrippers," *Proc Natl Acad Sci U S A*, vol. 106, no. 3, pp. 703-8, Jan 20 2009, doi: 10.1073/pnas.0807698106.

[80] T. G. Leong, B. R. Benson, E. K. Call, and D. H. Gracias, "Thin film stress driven self-folding of microstructured containers," *Small*, vol. 4, no. 10, pp. 1605-9, Oct 2008, doi: 10.1002/smll.200800280.

[81] D. Konig, M. Ehmann, S. Thienhaus, and A. Ludwig, "Micro- to Nanostructured Devices for the Characterization of Scaling Effects in Shape-Memory Thin Films," *Journal of Microelectromechanical Systems*, vol. 19, no. 5, pp. 1264-1269, 2010, doi: 10.1109/jmems.2010.2067441.

[82] M. Kabla, H. Seiner, M. Musilova, M. Landa, and D. Shilo, "The relationships between sputter deposition conditions, grain size, and phase transformation temperatures in NiTi thin films," *Acta Materialia*, vol. 70, pp. 79-91, 2014, doi: 10.1016/j.actamat.2014.02.009.

[83] A. Kumar, D. Singh, and D. Kaur, "Grain size effect on structural, electrical and mechanical properties of NiTi thin films deposited by magnetron co-sputtering," *Surface and Coatings Technology*, vol. 203, no. 12, pp. 1596-1603, 2009, doi: 10.1016/j.surfcoat.2008.12.005.

[84] X. Huang and A. G. Ramirez, "Effects of film dimension on the phase transformation behavior of NiTi thin films," *Applied Physics Letters*, vol. 95, no. 10, p. 101903, 2009, doi: 10.1063/1.3226104.

[85] X. Huang, H.-J. Lee, and A. G. Ramirez, "Incomplete martensitic transformations in NiTi thin films," *Scripta Materialia*, vol. 59, no. 10, pp. 1067-1070, 2008, doi: 10.1016/j.scriptamat.2008.07.017.

[86] B. Winzek *et al.*, "Recent developments in shape memory thin film technology," *Materials Science and Engineering: A*, vol. 378, no. 1-2, pp. 40-46, 2004, doi: 10.1016/j.msea.2003.09.105.

[87] X. Wang and J. J. Vlassak, "Thickness and film stress effects on the martensitic transformation temperature in equi-atomic NiTi thin films," *Mechanics of Materials*, vol. 88, pp. 50-60, 2015, doi: 10.1016/j.mechmat.2015.05.001.

[88] E. Q. M. Kohl, "Development of Microactuators Based on the Shape Memory Effect," *Journal De Physique IV* vol. 5, 1995.

[89] D. S. Grummon, R. Gotthardt, and T. LaGrange, "Planar Extrinsic Biasing of Thin Film Shape-Memory MEMS Actuators," *Mat. Res. Soc. Symp.*, vol. 741, 2003.

[90] David S. Grummon, Jinping Zhang, and T. J. Pence, "Relaxation and recovery of extrinsic stress in sputtered titanium–nickel thin films on (100)-Si," *Materials Science and Engineering: A*, vol. 273–275, pp. 722–726, 1999.

[91] A. P. L. Peter Krulevitch, Philip B. Ramsey, James C. Trevino, Julie Hamilton, and M. Allen Northp, "Thin Film Shape memory alloy microactuators," *Journal of Microelectromechanical Systems*, vol. 5, no. 4, p. 270, 1996.

[92] T. Waitz, T. Antretter, F. D. Fischer, and H. P. Karnthaler, "Size effects on martensitic phase transformations in nanocrystalline NiTi shape memory alloys," *Materials Science and Technology*, vol. 24, no. 8, pp. 934-940, 2008/08/01 2008, doi: 10.1179/174328408X302620.

[93] B. G. Priyadarshini, S. Aich, and M. Chakraborty, "Nano-crystalline Ni Ti alloy thin films fabricated using magnetron co-sputtering from elemental targets: Effect of substrate conditions," *Thin Solid Films*, vol. 616, pp. 733-745, 2016, doi: 10.1016/j.tsf.2016.09.034.

[94] T. Waitz, V. Kazykhanov, and H. P. Karnthaler, "Martensitic phase transformations in nanocrystalline NiTi studied by TEM," *Acta Materialia*, vol. 52, no. 1, pp. 137-147, 2004, doi: 10.1016/j.actamat.2003.08.036.

[95] G. Pan, Z. Cao, M. Wei, J. Shi, L. Xu, and X. Meng, "Thickness and grain size dependence of B2–R martensitic transformation behaviors in nanoscale TiNi films," *Materials Letters*, vol. 130, pp. 285-288, 2014, doi: 10.1016/j.matlet.2014.05.129.
[96] W.-S. Ko, S. B. Maisel, B. Grabowski, J. B. Jeon, and J. Neugebauer, "Atomic scale processes of phase transformations in nanocrystalline NiTi shape-memory alloys," *Acta Materialia*, vol. 123, pp. 90-101, 2017, doi: 10.1016/j.actamat.2016.10.019.
[97] J. Ye, R. K. Mishra, A. R. Pelton, and A. M. Minor, "Direct observation of the NiTi martensitic phase transformation in nanoscale volumes," *Acta Materialia*, vol. 58, no. 2, pp. 490-498, 2010, doi: 10.1016/j.actamat.2009.09.027.
[98] X. B. Shi, F. M. Guo, J. S. Zhang, H. L. Ding, and L. S. Cui, "Grain size effect on stress hysteresis of nanocrystalline NiTi alloys," *Journal of Alloys and Compounds*, vol. 688, pp. 62-68, 2016, doi: 10.1016/j.jallcom.2016.07.168.
[99] D. M. Norfleet *et al.*, "Transformation-induced plasticity during pseudoelastic deformation in Ni–Ti microcrystals," *Acta Materialia*, vol. 57, no. 12, pp. 3549-3561, 2009, doi: 10.1016/j.actamat.2009.04.009.
[100] D. Konig, "Fabrication and Characterization of nanoscale shape memory alloy objects," 2013.
[101] X. Wang, Y. Bellouard, Z. Xue, and J. J. Vlassak, "Thermal modeling of laser-annealing-induced crystallization of amorphous NiTi thin films," *Applied Physics A*, vol. 90, no. 4, pp. 689-694, 2007, doi: 10.1007/s00339-007-4331-z.
[102] Y. Bellouard, "Shape memory alloys for microsystems: A review from a material research perspective," *Materials Science and Engineering: A*, vol. 481-482, pp. 582-589, 2008, doi: 10.1016/j.msea.2007.02.166.
[103] N. Choudhary and D. Kaur, "Shape memory alloy thin films and heterostructures for MEMS applications: A review," *Sensors and Actuators A: Physical*, vol. 242, pp. 162-181, 2016, doi: 10.1016/j.sna.2016.02.026.
[104] H. Y. K. A. S. M. MASANARI TOMOZAWA, "Microactuators Using R-phase Transformation of Sputter-deposited Ti-47.3Ni Shape Memory Alloy Thin Films," *JOURNAL OF INTELLIGENT MATERIAL SYSTEMS AND STRUCTURES*, vol. 17, 2006, doi: 10.1177/1045389X06064883.
[105] M. Kohl, E. Just, W. Pfleging, and S. Miyazaki, "SMA microgripper with integrated antagonism.," *Sensors and Actuators A: Physical*, vol. 83, 2000.
[106] R. H. W. a. A. H. Heuer, "TiNi (Shape Memory) Films on Si for MEMS Applications," *Journal of Microelectromechanical Systems*, vol. 4, no. 4, p. 206, 1995.
[107] M. Dahmardeh *et al.*, "High-power MEMS switch enabled by carbon-nanotube contact and shape-memory-alloy actuator," *physica status solidi (a)*, vol. 210, no. 4, pp. 631-638, 2013, doi: 10.1002/pssa.201228678.
[108] M. S. Mohamed Ali, B. Bycraft, A. Bsoul, and K. Takahata, "Radio-Controlled Microactuator Based on Shape-Memory-Alloy Spiral-Coil Inductor," *Journal of Microelectromechanical Systems*, vol. 22, no. 2, pp. 331-338, 2013, doi: 10.1109/jmems.2012.2221161.
[109] S. Mukesh Kumar and M. V. Lakshmi, "Applications of Shape Memry Alloys in MEMS Devices," *International Journal of Advanced Research in Computer and Communication Engineering*, vol. 2, no. 2, 2013.
[110] "Micromachining process for thin-film SMA actuators."

[111] E. Quandt *et al.*, "Sputter deposition of TiNi, TiNiPd and TiPd films displaying the 2-way SME," *Sensors and Actuators A: Physical*, vol. 53, pp. 434-439, 1996.
[112] M. Salehi, M. Hamedi, H. S. Nohouji, and J. Arghavani, "Mechanical properties identification and design optimization of nitinol shape memory alloy microactuators," *Smart Materials and Structures*, vol. 23, no. 2, p. 025001, 2014, doi: 10.1088/0964-1726/23/2/025001.
[113] C. R. Knick, G. L. Smith, D. P. Cole, N. W. Piekiel, and C. J. Morris, "Investigating nanoscale behavior of NiTi SMA films deposited on soft substrates " in *Proceedings of the ASME 2017 Conference on Smart Materials, Adaptive Structures and Intelligent Systems*, Snowbird, Utah, 2017: ASME.
[114] A. Ishida and M. Sato, "Development of Polyimide/SMA Thin-Film Actuator," *Materials Science Forum*, vol. 654-656, pp. 2075-2078, 2010, doi: 10.4028/www.scientific.net/MSF.654-656.2075.
[115] S. Zaidi, F. Lamarque, C. Prelle, O. Carton, and A. Zeinert, "Contactless and selective energy transfer to a bistable micro-actuator using laser heated shape memory alloy," *Smart Materials and Structures*, vol. 21, no. 11, p. 115027, 2012, doi: 10.1088/0964-1726/21/11/115027.
[116] F. Sassa, Y. Al-Zain, T. Ginoza, S. Miyazaki, and H. Suzuki, "Miniaturized shape memory alloy pumps for stepping microfluidic transport," *Sensors and Actuators B: Chemical*, vol. 165, no. 1, pp. 157-163, 2012, doi: 10.1016/j.snb.2011.12.085.
[117] D. S. Grummon, "Thin-Film Shape-Memory Materials for high temperature applications," *Smart Structural Materials*, 2003.
[118] D. D. Shin, D.-G. Lee, K. P. Mohanchandra, and G. P. Carman, "Thin film NiTi microthermostat array," *Sensors and Actuators A: Physical*, vol. 130-131, pp. 37-41, 2006, doi: 10.1016/j.sna.2005.10.010.
[119] C. A. Biffi and A. Tuissi, "Nitinol laser cutting: microstructure and functional properties of femtosecond and continuous wave laser processing," *Smart Materials and Structures*, vol. 26, no. 3, p. 035006, 2017, doi: 10.1088/1361-665X/aa5596.
[120] M. Taheri Andani *et al.*, "Mechanical and shape memory properties of porous Ni50.1Ti49.9 alloys manufactured by selective laser melting," *J Mech Behav Biomed Mater*, vol. 68, pp. 224-231, Apr 2017, doi: 10.1016/j.jmbbm.2017.01.047.
[121] R. F. Hamilton, B. A. Bimber, M. Taheri Andani, and M. Elahinia, "Multi-scale shape memory effect recovery in NiTi alloys additive manufactured by selective laser melting and laser directed energy deposition," *Journal of Materials Processing Technology*, vol. 250, pp. 55-64, 2017, doi: 10.1016/j.jmatprotec.2017.06.027.
[122] M. Elahinia, N. Shayesteh Moghaddam, M. Taheri Andani, A. Amerinatanzi, B. A. Bimber, and R. F. Hamilton, "Fabrication of NiTi through additive manufacturing: A review," *Progress in Materials Science*, vol. 83, pp. 630-663, 2016, doi: 10.1016/j.pmatsci.2016.08.001.
[123] S. Dadbakhsh, M. Speirs, J. Van Humbeeck, and J.-P. Kruth, "Laser additive manufacturing of bulk and porous shape-memory NiTi alloys: From processes to potential biomedical applications," *MRS Bulletin*, vol. 41, no. 10, pp. 765-774, 2016, doi: 10.1557/mrs.2016.209.
[124] J. Ma *et al.*, "Spatial Control of Functional Response in 4D-Printed Active Metallic Structures," *Sci Rep*, vol. 7, p. 46707, Apr 21 2017, doi: 10.1038/srep46707.

[125] H. K. William L. Benard, Arthur H. Heuer, And Michael A. Huff, "Thin-Film Shape-Memory Alloy Actuated Micropumps," *Journal of Microelectromechanical Systems,* vol. 7, no. 2, pp. 245-251, 1998.
[126] T. M. Eiji Makino, Takayuki Shibata, "Micromachining of TiNi shape memory thin film for fabrication of micropump," *Sensors and Actuators A: Physical,* vol. 79, pp. 251–259, 2001.
[127] C. Y. Chung and P. M. Chan, "NiTi shape memory alloy thin film micro-cantilevers array," *Thin Solid Films,* vol. 519, no. 15, pp. 5307-5309, 2011, doi: 10.1016/j.tsf.2011.01.116.
[128] J. P. Tan, W.M. Huang, X. Y. Gao, J. H. Yeo, and J. M. Miao, "NiTi shape memory alloy thin film based microgripper," *Smart Materials,* vol. 4234, 2001.
[129] Q. He *et al.,* "Characterization of sputtering deposited NiTi shape memory thin films using a temperature controllable atomic force microscope," *Smart Materials and Structures,* vol. 13, no. 5, pp. 977-982, 2004, doi: 10.1088/0964-1726/13/5/001.
[130] S. Dadbakhsh, B. Vrancken, J. P. Kruth, J. Luyten, and J. Van Humbeeck, "Texture and anisotropy in selective laser melting of NiTi alloy," *Materials Science and Engineering: A,* vol. 650, pp. 225-232, 2016, doi: 10.1016/j.msea.2015.10.032.
[131] C. Craciunescu and A. Ercuta, "Modulated interaction in double-layer shape memory-based micro-designed actuators," *Sci Technol Adv Mater,* vol. 16, no. 6, p. 065003, Dec 2015, doi: 10.1088/1468-6996/16/6/065003.
[132] S. Timoshenko, "Analysis of bimetal thermostats," *J. Opt. Soc. Am.,* vol. 11, pp. 233-256, 1925.
[133] C. Craciunescu and A. Ercuta, "Prediction of thermally-controlled actuation for shape memory alloy film-based bimorph cantilevers," *Smart Materials and Structures,* vol. 23, no. 7, 2014, doi: 10.1088/0964-1726/23/7/075025.
[134] X. Wang, S. Kustov, B. Verlinden, and J. Van Humbeeck, "Fundamental Development on Utilizing the R-phase Transformation in NiTi Shape Memory Alloys," *Shape Memory and Superelasticity,* vol. 1, no. 2, pp. 231-239, 2015, doi: 10.1007/s40830-015-0007-2.
[135] Z. Lekston and E. Lagiewka, "X-ray diffraction studies of NiTi shape memory alloys," *Achives of Materials Science and Engineering,* vol. 28, no. 11, pp. 665-672, 2007.
[136] X. Wang, C. Li, B. Verlinden, and J. Van Humbeeck, "Effect of grain size on aging microstructure as reflected in the transformation behavior of a low-temperature aged Ti–50.8at.% Ni alloy," *Scripta Materialia,* vol. 69, no. 7, pp. 545-548, 2013, doi: 10.1016/j.scriptamat.2013.06.023.
[137] A. R. Pelton, "Nitinol Fatigue: A Review of Microstructures and Mechanisms," *Journal of Materials Engineering and Performance,* vol. 20, no. 4-5, pp. 613-617, 2011, doi: 10.1007/s11665-011-9864-9.
[138] Y. T. Huilong Hou, Reginald F. Hamilton, and Mark W. Horn, "Functional fatigue of submicrometer NiTi shape memory alloy films," *Journal of Vacuum Science & Technology A: Vacuum, Surfaces, and Films,* vol. 35, no. 4, 2017, doi: 10.1116/1.4983011.
[139] C. Chluba *et al.,* "Ultralow-fatigue shape memory alloy films," *Science,* vol. 348, no. 6238, 2015.
[140] J. Cui *et al.*, "Demonstration of high efficiency elastocaloric cooling with large ΔT using NiTi wires," *Applied Physics Letters,* vol. 101, no. 7, p. 073904, 2012, doi: 10.1063/1.4746257.

[141] C. Chluba, H. Ossmer, C. Zamponi, M. Kohl, and E. Quandt, "Ultra-Low Fatigue Quaternary TiNi-Based Films for Elastocaloric Cooling," *Shape Memory and Superelasticity,* vol. 2, no. 1, pp. 95-103, 2016, doi: 10.1007/s40830-016-0054-3.
[142] C. Elbuken, L. Gui, C. L. Ren, M. Yavuz, and M. B. Khamesee, "Design and analysis of a polymeric photo-thermal microactuator," *Sensors and Actuators A: Physical,* vol. 147, no. 1, pp. 292-299, 2008, doi: 10.1016/j.sna.2008.04.019.
[143] H. Adam, S. Rode, M. Schreiber, K. Kobayashi, H. Yamada, and A. Kuhnle, "Photothermal excitation setup for a modified commercial atomic force microscope," *Rev Sci Instrum,* vol. 85, no. 2, p. 023703, Feb 2014, doi: 10.1063/1.4864084.
[144] D. R. Evans, P. Tayati, H. An, P. K. Lam, V. S. Craig, and T. J. Senden, "Laser actuation of cantilevers for picometre amplitude dynamic force microscopy," *Sci Rep,* vol. 4, p. 5567, Jul 4 2014, doi: 10.1038/srep05567.
[145] B. T. O'Callahan and M. B. Raschke, "Laser heating of scanning probe tips for thermal near-field spectroscopy and imaging," *APL Photonics,* vol. 2, no. 2, p. 021301, 2017, doi: 10.1063/1.4972048.
[146] J. H. Cho, T. James, and D. H. Gracias, "Curving nanostructures using extrinsic stress," *Adv Mater,* vol. 22, no. 21, pp. 2320-4, Jun 4 2010, doi: 10.1002/adma.200904410.
[147] L.-H. Han and S. Chen, "Wireless bimorph micro-actuators by pulsed laser heating," *Sensors and Actuators A: Physical,* vol. 121, no. 1, pp. 35-43, 2005, doi: 10.1016/j.sna.2004.12.012.
[148] T. Ohnishi and A. Sugimura, "Optical actuation of micromirrors fabricated by the micro-origami technique," *Appl Phys Lett,* vol. 83, no. 18, Aug 31 2009.
[149] D. L. Dickensheets *et al.*, "Thermally actuated microshutter for MOEMS applications," vol. 7208, p. 720809, 2009, doi: 10.1117/12.809776.
[150] "HIGH SPEED, LARGE MOTION ELECTROSTATIC ARTIFICIAL EYELID."
[151] T. George *et al.*, "Complex MEMS device: microshutter array system for space applications," vol. 6556, p. 655602, 2007, doi: 10.1117/12.721502.
[152] S. Baglio, S. Castorina, L. Fortuna, and N. Savalli, "Modeling and design of novel photo-thermo-mechanical microactuators," *Sensors and Actuators A: Physical,* vol. 101, pp. 185-193, 2002.
[153] M. P. S S *et al.*, "Thermo-mechanical behavior of shape memory alloy spring actuated using novel scanning technique powered by ytterbium doped continuous fiber laser," *Smart Materials and Structures,* 2019, doi: 10.1088/1361-665X/ab06d8.
[154] J. R. L. Murrer, S. H. Goodwin, D. E. Dausch, S. L. Solomon, and M. K. Lamvik, "Electrostatic artificial eyelid actuator as an analog micromirror device," vol. 5785, p. 59, 2005, doi: 10.1117/12.603699.
[155] G. Ritt and B. Eberle, "Automatic laser glare suppression in electro-optical sensors," *Sensors (Basel),* vol. 15, no. 1, pp. 792-802, Jan 5 2015, doi: 10.3390/s150100792.
[156] C. Lewis, S. Svensson, G. P. Owen, S. Björkert, H. Kariis, and C. Lopes, "Countering laser pointer threats to road safety," 2006, vol. 6402, p. 640207, doi: 10.1117/12.689057.
[157] E. A. Wachter, T. Thundat, P. I. Oden, R. J. Warmack, P. G. Datskos, and S. L. Sharp, "Remote optical detection using microcantilevers," *Review of Scientific Instruments,* vol. 67, no. 10, pp. 3434-3439, 1996, doi: 10.1063/1.1147149.
[158] Z. Qian, S. Kang, V. Rajaram, C. Cassella, N. E. McGruer, and M. Rinaldi, "Zero-power infrared digitizers based on plasmonically enhanced micromechanical photoswitches," *Nat Nanotechnol,* vol. 12, no. 10, pp. 969-973, Oct 2017, doi: 10.1038/nnano.2017.147.

[159] B.-K. L. Chen-Luen Shih, Harold Kahn, Stephen M. Phillips, and Arthur H. Heuer, "A robust co-sputtering fabrication procedure for TiNi shape memory alloys for MEMS," *JMEMS*, vol. 10, pp. 69-79, 2001.
[160] R. H. W. a. A. H. Heuer, "TiNi (Shape Memory) Films on Si for MEMS Applications," *Journal of Microelectromechanical Systems*, vol. 4, no. 4, 1995.
[161] D. König, P. J. S. Buenconsejo, D. Grochla, S. Hamann, J. Pfetzing-Micklich, and A. Ludwig, "Thickness-dependence of the B2–B19 martensitic transformation in nanoscale shape memory alloy thin films: Zero-hysteresis in 75nm thick Ti51Ni38Cu11 thin films," *Acta Materialia*, vol. 60, no. 1, pp. 306-313, 2012, doi: 10.1016/j.actamat.2011.09.037.
[162] P. H. I. Jarrige, P. Jonnard, "Diffusion processes in NiTi/Si, NiTi/SiO_2 and NiTi/Si_3N_4 systems under annealing," *Thin Solid Films*, vol. 458, pp. 314-321, 2004, doi: https://doi.org/10.1016/j.tsf.2003.12.039.
[163] L. L. C. Yu, J. Wood, C. Pelter, A. Hirohata, K. O'Grady, J. Sagar, "Effect of Seed Layers on Polycrystalline Co2FeSi Thin Films," *IEEE Transactions on Magnetics*, vol. 48, pp. 4006–4009, 2012, doi: https://doi.org/10.1109/tmag.2012.2202890.
[164] C. K. Kenneth Ainslie, Gabriel Smith, Jianheng Li, Charles Troxel, Apurva Mehta, Roopali Kukreja, "Controlling shape memory effects in NiTi thin films grown on Ru seed layer," *Sensors and Actuators A: Physical*, vol. 294, p. 7, 2019. [Online]. Available: https://doi.org/10.1016/j.sna.2019.04.047.
[165] M. S. J. X. Zhang, A. Ishida, "On the Ti2Ni precipitates and Guinier–Preston zones in Ti-rich Ti–Ni thin films," *Acta Materialia*, vol. 51, 2003.
[166] V. K. T. Waitz, H. P. Karnthaler, "Martensitic phase transformations in nanocrystalline NiTi studied by TEM," *Acta Materialia*, vol. 52, no. 1, pp. 137-147, 2004.
[167] H. P. K. T.Waitz, "Martensitic transformation of NiTi nanocrystals embedded in an amorphous matrix," *Acta Materialia*, vol. 52, no. 19, pp. 5461-5469, 2004.
[168] C. R. Knick, G. L. Smith, C. J. Morris, and H. A. Bruck, "Rapid and low power laser actuation of sputter-deposited NiTi shape memory alloy (SMA) MEMS thermal bimorph actuators," *Sensors and Actuators A: Physical*, vol. 291, pp. 48-57, 2019, doi: 10.1016/j.sna.2019.03.016.
[169] K. O. A. Ishida, M. Sato & S. Miyazaki "Microstructure of Ti-48.2 at. Pct Ni shape memory thin films," *Metallurgical and Materials Transactions A*, vol. 28, pp. 1985-1991, 1997.
[170] M. Tomozawa, H. Y. Kim, and S. Miyazaki, "Microactuators Using R-phase Transformation of Sputter-deposited Ti-47.3Ni Shape Memory Alloy Thin Films," *Journal of Intelligent Material Systems and Structures*, vol. 17, no. 12, pp. 1049-1058, 2006, doi: 10.1177/1045389x06064883.
[171] Y. I. S.Miyazaki, K.Otsuka, "Effect of thermal cycling on the transformation temperatures of TiNi alloys," *Acta Materialia*, vol. 34, no. 10, 1986.
[172] E. P. Ryklina, K. A. Polyakova, N. Y. Tabachkova, N. N. Resnina, and S. D. Prokoshkin, "Effect of B2 austenite grain size and aging time on microstructure and transformation behavior of thermomechanically treated titanium nickelide," *Journal of Alloys and Compounds*, vol. 764, pp. 626-638, 2018, doi: 10.1016/j.jallcom.2018.06.102.
[173] E. P. J. Burow, C. Somsen, J. Frenzel, R.Z. Valiev, G.F. Eggeler, "Martensitic Transformations and Functional Stability in Ultra-Fine Grained NiTi Shape Memory Alloys," *Materials Science Forum*, pp. 852-857, 2008.

[174] T. K. K. Ogawa, S. Kajiwara, T. Matsunaga, S. Miyazaki, "Coherent subnanometric plate precipitates formed during crystallization of As-sputtered Ti-Ni films," *J. Phys.* , pp. 221-226, 1997.
[175] G. M. P. W. C. Oliver, "An improved technique for determining hardness and elastic modulus using load and displacement sensing indentation experiment," *Journal of Materials Research,* vol. 7, no. 6, 1992.
[176] D. P. Cole, "Fabrication and Characterization of Compositionally-Graded Shape Memory Alloy Films," PhD, Mechanical Engineering, University of Maryland College Park, 2009.
[177] D. P. Cole, H. A. Bruck, and A. L. Roytburd, "Nanoindentation studies of graded shape memory alloy thin films processed using diffusion modification," *Journal of Applied Physics,* vol. 103, no. 6, p. 064315, 2008, doi: 10.1063/1.2888510.
[178] D. P. Cole, H. Jin, W.-Y. Lu, A. L. Roytburd, and H. A. Bruck, "Reversible nanoscale deformation in compositionally graded shape memory alloy films," *Applied Physics Letters,* vol. 94, no. 19, p. 193114, 2009, doi: 10.1063/1.3129167.
[179] M. D. S. Cory R. Knick, Christopher J. Morris, "Characterization of Sputtered Nickel-Titanium Shape Memory Alloy and Microfabricated Thermal Actuators," in *IEEE MEMS*, Shanghai, China, 2016.
[180] M. H. Ervin, S. S. Bedair, C. R. Knick, H. Tsang, B. Isaacson, and N. W. Piekiel, "Evaporation Driven Assembly of On-Chip Thermite Devices," *Journal of Microelectromechanical Systems,* vol. 26, no. 6, pp. 1408-1416, 2017, doi: 10.1109/jmems.2017.2757149.
[181] L. H. Petr Sittner, Jan Pilch, Caroline Curfs, Thiery Alonso, and Denis Favier, "Young's Modulus of Austenite and Martensite Phases in Superelastic NiTi Wires," *Journal of Materials Engineering and Performance,* vol. 23, no. 7, 2014, doi: 10.1007/s11665-014-0976-x.
[182] G. A. Shaw, D. S. Stone, A. D. Johnson, A. B. Ellis, and W. C. Crone, "Shape memory effect in nanoindentation of nickel–titanium thin films," *Applied Physics Letters,* vol. 83, no. 2, pp. 257-259, 2003, doi: 10.1063/1.1591235.
[183] C. R. Knick, D. J. Sharar, A. A. Wilson, G. L. Smith, C. J. Morris, and H. A. Bruck, "High frequency, low power, electrically actuated shape memory alloy MEMS bimorph thermal actuators," *Journal of Micromechanics and Microengineering,* vol. 29, no. 7, p. 075005, 2019, doi: 10.1088/1361-6439/ab1633.
[184] C. A. Klein and R. P. Miller, "Strains and stresses in multilayered elastic structures: The case of chemically vapor-deposited ZnS/ZnSe laminates," *Journal of Applied Physics,* vol. 87, no. 5, pp. 2265-2272, 2000, doi: 10.1063/1.372171.
[185] Y. W. Xiaobo Zhang, Xiaodan Miao, Congchun Zhang, and Guifu Ding, "An Electro-thermal SU-8 Cantilever Micro Actuator based on Bimorph Effect," in *Proceedings of the 2010 5th IEEE International Conference on Nano/Micro Engineered and Molecular Systems*, Xiamen, China, 2010: IEEE, pp. 362-365.
[186] J. R. L. Murrer, S. H. Goodwin, D. E. Dausch, S. L. Solomon, and M. K. Lamvik, "Electrostatic artificial eyelid actuator as an analog micromirror device," presented at the Technologies for Synthetic Environments: Hardware-in-the-Loop Testing X, 2005.
[187] J. M. Zanardi Ocampo *et al.*, "Optical actuation of micromirrors fabricated by the micro-origami technique," *Applied Physics Letters,* vol. 83, no. 18, pp. 3647-3649, 2003, doi: 10.1063/1.1622800.

[188] D. P. Camilo Velez, Sukjun Kim, Mahnoush Babaei, Cory Knick, Gabriel Smith, and Sarah Bergbreiter, "Combining Micro Fabrication and Additive Manufacturing for Microrobotic Mechanisms," *Special Proceedings of JMEMS* Combining Micro Fabrication and Additive Manufacturing for Microrobotic Mechanisms Camilo Velez1, Dinesh Patel, Sukjun Kim, Mahnoush Babaei, Cory Knick, Gabriel Smith, and Sarah Bergbreiter, special proceedings JMEMS (2020), 2020.

[189] S. K. Camilo Velez, Dinesh Patel, Mahnoush Babaei, Cory R. Knick, Gabriel Smith, and Sarah Bergbreiter, "Rapid Prototyping of Microactuators by Integrating 3D Printed Polymeric Structures With NiTi Thin Film," presented at the 33rd IEEE International Conference on Micro Electromechanical Systems (MEMS), 2020.

[190] W. G. Christoph Chluba, Rodrigo Lima de Miranda, Julian Strobel, Lorenz Kienle, Eckhard Quandt, Manfred Wuttig, "Ultralow-fatigue shape memory alloy films," *Science*, vol. 348 no. 6238, 2015.